An Experimental and Numerical Investigation of Nonlinear Normal Modes in Geometrically Nonlinear Structures

by

David Adam Ehrhardt

A dissertation submitted in partial fulfillment of the requirements for the degree of

DOCTOR OF PHILOSOPHY

(Engineering Mechanics)

at the

UNIVERSITY OF WISCONSIN-MADISON

2015

Date of final oral examination: 05/12/2015

The dissertation is approved by the following members of the Final Oral Committee:

Matthew S. Allen, Associate Professor, Engineering Physics

Daniel C. Kammer, Professor, Engineering Physics

Roderic S. Lakes, Professor, Engineering Physics

Melih Eriten, Assistant Professor, Mechanical Engineering

Timothy J. Beberniss, Aerospace Engineer, Air Force Research Laboratory

Abstract

The design of modern structures operating in dynamic environments has placed emphasis on light weight, flexible, and reusable structures, that lead to nonlinear force-displacement relationships. In contrast, the test and analysis techniques that are available to guide designers are fundamentally based on linear force-displacement relationships. The discrepancy between the techniques needed and those that are available has motivated the pursuit of a better understanding of how nonlinearity manifests in the field of structural dynamics. Although nonlinear behavior can manifest in infinitely many ways, there are several features that can be commonly observed in nonlinear structures. For example, the dynamic response amplitude can be seen to depend on input energy or amplitude, the underlying (e.g. about some equilibrium) linear modes of vibration become coupled at high dynamic response amplitudes, and higher harmonics are generated in the response when the structure is subjected to a sinusoidal input. In this context, new nonlinear test and analysis techniques should be developed to address the generally observed behavior. This dissertation seeks to contribute to the nonlinear dynamic testing of structures in two ways: first by presenting a means of collecting large number of DOF measurements from the linear and nonlinear structure, and second by improving the means the nonlinear structure is experimentally characterized with the improved implementation of the nonlinear normal mode (NNM) concept in a testing environment.

The first contribution of this work to the state of the art extends the use of the spatially dense measurement techniques of Three Dimensional-Digital Image Correlation (3D-DIC) and Continuous-scan Laser Doppler Vibrometry (CSLDV) to nonlinear vibration measurements, and presents the first experimental comparison of both techniques. 3D-DIC and CSLDV exhibit limitations under certain loading conditions, deformation amplitudes, and complexity of spatial

deformation as will be discussed in this dissertation. The full-field deformation information available with 3D-DIC and CSLDV is especially beneficial when studying the thin walled structures that are examined here. In linear response regimes, these structures are sensitive to initial geometric imperfections which will effect the global dynamics of the structure. When only a few measurement points are available, as with traditional test methods, there typically is not enough information to tell what imperfections my be present and what effect they have on the dynamics of a structure. In contrast, imperfections are clearly visible in full-field deformation measurements. Furthermore, in nonlinear response regimes, these structures exhibit a nonlinear coupling between linear normal modes, which is evident in the strength of the higher harmonics and the deformation shape at each harmonic. This nonlinear coupling can be characterized using the full-field deformation available at each harmonic.

This work's second contribution is the development of a new stepped-sine testing strategy that allows the experimentalist to more easily isolate the nonlinear normal modes (NNMs) of the structure of interest. NNMs are *not necessarily synchronous periodic solutions* of the conservative nonlinear equations of motion (EOM) and can be arranged to compactly present nonlinear behavior in frequency-energy plots (FEPs). A substantial amount of previous work involving NNMs has focused on low dimension, or low degree of freedom (DOF), nonlinear systems. This work seeks to exploit recent advancements that allow the computation of NNMs for continuous structures with geometric nonlinearities. This is of particular interest since well separated linear normal modes (LNMs) of such structures can become coupled, as evident by the harmonic content observed in a nonlinear response regimes. This coupling causes an unexpected, and possibly detrimental, change in the deformation of the structure. The harmonic content and deformation shapes along FEP branches are key to the characterization of the nonlinear coupling

of a structure's LNMs as a structure operates in nonlinear response regimes. This necessitates the need for full-field measurements in the experimental identification of an NNM since the once well separated LNMs are now commensurate at several harmonics in the response. Therefore, a multi-harmonic input force is needed to isolate each LNM motion at each harmonic The required input force is identified by tuning the fundamental frequency and amplitudes of the force at each harmonic until the force/velocity plots of the positive and negative portions of the periodic cycle overlay.

The use of full-field measurement techniques to isolate a structure's NNMs gives ample spatial information when comparing test and analysis as a structure transitions from a linear response regime to a nonlinear response regime. As will be shown, a structure's full-field deformation provides valuable insight to the nonlinear deformation experienced by a structure. Now that these methods can be used to identify the way in which the LNMs combine to produce each NNM, a nonlinear experimental model can be identified from the measurements by projecting the nonlinear deformation onto the structures LNMs. This experimental model allows one to compare the actual performance of the structure with numerically calculated modal models in much more detail and is shown to help guide model updating efforts.

Acknowledgements

My path to a Ph.D. has included 22 years focusing on my education. Teachers and professors have been central to my success and require my deepest gratitude. First and foremost, I would like to thank my advisor, Dr. Matt Allen, for his assistance and patience during my time at UW-Madison. He support and guidance have further deepened my understanding and desire to pursue my research path. I would also like to thank my previous advisor, Dr. Jorge Abanto-Bueno, for setting me on my current path to a Ph.D. I would not have achieved my current level of academic success without continuous encouragement from my former teacher, Mr. Roger Leach, who has always pushed me to continue to learn.

I would also like to extend my gratitude to my Ph.D. committee for taking the time to review the material in this dissertation and provide feedback. I'd like to extend a special thanks to Tim Beberniss for his help in the lab and support when using high speed 3D-DIC for all of my summers spent in Ohio.

I have had the pleasure of meeting many talented colleagues throughout my time spent at UW-Madison and Bradley University. These researchers are too numerous to list, but have been key to the development of this work.

I am grateful for receiving financial support from the Wisconsin Alumni Research Foundation and the Morgridge Distinguished Graduate Fellowship as well as the J. Gordon Baker Fellowship.

Finally, I would like to thank my family and friends for all of their support and encouragement during my time as a student. Without their reinforcement I probably would not be where I am today. My wife and parents have always been the a positive force throughout my academic career and I am eternally grateful.

Abbreviations

3D-DIC	Three-Dimensional Digital Image Correlation
CSLDV	Continuous-scan Laser Doppler Vibrometry
DOF	Degree-of-freedom
EOM	Equations of Motion
FEA	Finite Element Analysis
FEM	Finite Element Model
FRF	Frequency Response Function
LNM	Linear Normal Mode
MAC	Modal Assurance Criterion
MIF	Mode Indicator Function
MO	Mode Orthogonality
NNM	Nonlinear Normal Mode
V&V	Verification and Validation

Contents

1 Introduction

1.1 *Motivation*

The testing and analysis of a machine or structure are key steps to support decision making during the design process. For instance, complementary results from a test and an analysis are used to identify areas of uncertainty between the physical machine or structure and the mathematical model used to describe it. Alternatively, individual results from an analysis are used when the machine or structure of interest operates outside the ranges of available testing facilities. Similarly, individual results from a test are used when the machine or structure operates within knowledge gaps of analysis methods. In current practice, an analytical model will not typically be used without first comparing its response to tests on the structure of interest; otherwise unexpected errors can distort results and lead to incorrect design decisions. In this context, formal guidelines have been created to aid in the establishment of a suitable comparison between test and analysis under the title of model validation, which is a branch of Verification and Validation (V&V) [1]. Model validation seeks to answer the question, *"Are we solving the correct equations?"* by comparing the physical and modeled structure under expected loading conditions [2]. Prior to model validation, a model calibration is performed, where fundamental properties of the physical and modeled structure are compared with the goal of determining the correct model order, selected structural parameters, and quantifying uncertainty within the physical and modeled structure. Due to the overlapping relationship between test and analysis throughout the model validation process, advancements in testing techniques are motivated by advances in analysis methods, and visa-versa.

When considering the field of structural vibrations, a substantial amount of work has built model calibration metrics around dynamic linear force-displacement relationships [3-6]. These metrics hinge on the quantification of invariant dynamic properties inherent to the linear normal modes (LNMs) of a structure (e.g. resonant frequencies and mode shapes), and include resonant frequency error, frequency response functions, modal assurance criterion (MAC), etc. [7]. Physically, LNMs represent uncoupled synchronous motions of a structure defined by its undamped free vibration characteristics. Mathematically, LNMs represent non-trivial solutions to the conservative unforced equations of motion (EOM):

$$\mathbf{M}\ddot{\mathbf{x}}(t) + \mathbf{K}\mathbf{x}(t) = 0 \tag{1.1}$$

For an n degree of freedom (DOF) system, $\mathbf{M}$ is an n x n mass matrix, $\mathbf{K}$ is an n x n stiffness matrix, $\mathbf{x}(t)$ is an n x 1 vector of the displacement of the system, and $\ddot{\mathbf{x}}(t)$ is an n x 1 vector of the acceleration of the system. Assuming harmonic motion, $\mathbf{x}(t) = \mathbf{X}\cos(\omega t)$, the EOM can be recast as an eigenvalue/vector problem:

$$\left(\mathbf{K} - \boldsymbol{\omega}_n{}^2\mathbf{M}\right)\boldsymbol{\Phi} = 0 \tag{1.2}$$

Where the n x 1 eigenvalues ($\boldsymbol{\omega}_n$) and the n x n eigenvectors ($\boldsymbol{\Phi}$) define the LNMs of a structure. For a linear structure such as this, the LNMs are amplitude invariant, decouple the EOM due to their orthogonality, and can be used to find an analytical solution for the free and forced vibrations of the structure through the superposition principle. Exploiting the properties of LNMs in structural vibrations has been the cornerstone to developing test and analysis techniques in the areas of finite element model updating [4], experimental modal analysis [5], and model reduction [8].

A central idea behind these techniques is the use of a truncated set of dynamically important LNMs to define the structure's global free or forced deformations and guide the model calibration. It is left to the engineer to decide which set of LNMs to measure in a test or use in an analysis, and there are several techniques to aid in this decision [8]. The number of LNMs included in the truncated set further defines the minimum number and location of measured or modeled degrees of freedom (DOF). In current practice, the number of DOF within a test is typically tens to hundreds, while analysis methods can produce millions. In standard practice, the data available from an analysis is reduced or interpolated to compare with test data. The assumption is made that the reduced DOF used in an experiment can capture the LNMs of a structure well. However, structures whose dynamics are sensitive to the definition of the initial static equilibrium (e.g. thin beams and plates) can experience variations in LNMs that are not captured by the truncated set of DOF, underlining the need for more experimental measurement DOF. A second assumption this process makes is that the physical structure behaves linearly, justifying the use of LNMs as a basis for the model calibration process. However, the linearity assumption is well known as the exception rather than the rule for real world structures, and the increasing desire to design nonlinear structures has accentuated the short comings of using LNMs as a basis for nonlinear model calibration. This dissertation seeks to address these model calibration shortcomings in two ways: first by presenting a means of collecting spatially dense measurements from the linear and nonlinear structure, and second by developing a new stepped-sine testing strategy that allows the experimentalist to more easily isolate the nonlinear normal modes. These objectives are explained in detail below.

The total available number of DOF in a test is presently limited by the use of traditional discrete sensors (e.g. accelerometers, linearly varying displacement transducers, and strain

gauges). The number of such sensors that can be used in a test is restricted by cost and their effect on the structural response. For example, when a large number of such sensors are attached to the structure, the mass loading effects will decrease the natural frequencies and distort the mode shapes of a structure. Advanced measurement techniques, such as Continuous-scan Laser Doppler Vibrometry (CSLDV) [9] and high speed Three Dimensional-Digital Image Correlation (3D-DIC) [10], have been developed to obtain more spatial information of a structure's deformation while reducing the effect on the response of a structure. Both techniques are relatively new and have not been effectively compared as a structure deforms from linear to nonlinear response regimes in a vibratory environment. Additionally, the combination of CSLDV and 3D-DIC within the framework of a nonlinear normal mode, which is expounded upon in the next paragraph, provides the information needed to diagnose how the LNMs are coupled as a response transitions from a linear to a nonlinear response regime.

The generalization of a mode of vibration to accommodate nonlinear responses has lead to the definition of nonlinear normal modes (NNMs). Rosenberg [11] first defined a NNM as a *synchronous motion* of the nonlinear system which provided a direct extension of the LNM concept. This definition has been broadened to include *not necessarily synchronous periodic motions* of the conservative nonlinear equations of motion (EOM) [12, 13]. The extended definition allows NNMs to contain phenomena including bifurcations [12], internal resonances [14], and strong dependence on the amplitude of the response [15]. The primary body of work on NNMs has been on their analytical and numerical calculation for low DOF systems [13]. Few works have been published in which an NNM of a physical structure has been isolated experimentally [16, 17], perhaps because of the complex dynamics associated with a NNM response. Over the past several decades, phase separation [18-20], and phase resonance

techniques [21, 22], have been explored to experimentally characterize a nonlinear structure. The development of these methods has relied on the assumption that the damping observed in a structure is well defined; however, this is not generally the case for real structures. By approaching the measurement of a NNM as a stepped-sine test, an appropriation vector can be realized at each subsequent step removing the need for this damping assumption. However, the multi-harmonic nature of the response makes determining the correct appropriation vector difficult in practice. This thesis proposes a means of isolating an NNM, and shows that by simply monitoring a force-velocity plot (which is easy to implement in real time) one can tune the frequency and harmonic amplitudes in the force to isolate an NNM.

For the purposes of this thesis, the final goal of the comparison of test and analysis is to create a calibrated model that captures the dynamics of a structure in the response regions of interest which can then be applied to other loading conditions not considered in a physical test scenario. If a structure behaves linearly, the accurate modeling of LNMs over a frequency range of interest can give the designer confidence in the predicted structural deformation in a dynamic environment. The use of LNMs to update the underlying analytical model is well established in the field of structural dynamics [4]. As previously discussed, the dynamic test and analysis procedures built on LNMs cannot be directly applied to the determination of NNMs; however, it is useful to first determine the LNMs (e.g. about some equilibrium) of the nonlinear structure to be used as a starting point when updating the nonlinear model. This now becomes the first step in the model calibration process used for this dissertation shown in Fig. 1.1. LNMs define an unambiguous model of the structure in its initial state providing an anchor for the model calibration. With the fully updated linear models, the NNMs can be calculated using an assumed initial form of the nonlinearity. Alternatively, the form of the nonlinearity can be determined

after obtaining the experimentally measured NNMs. Since the combination of full-field measurements and the identification of the NNMs provides the information needed to characterize the nonlinearity, the nonlinear coupling between the LNMs can also be identified using the full-field measurements and projecting the deformation observed at each harmonic onto the LNMs of a structure. The previously established work leads to the final step in the calibrated nonlinear model where the identified nonlinear coefficients can be used to update the nonlinear model.

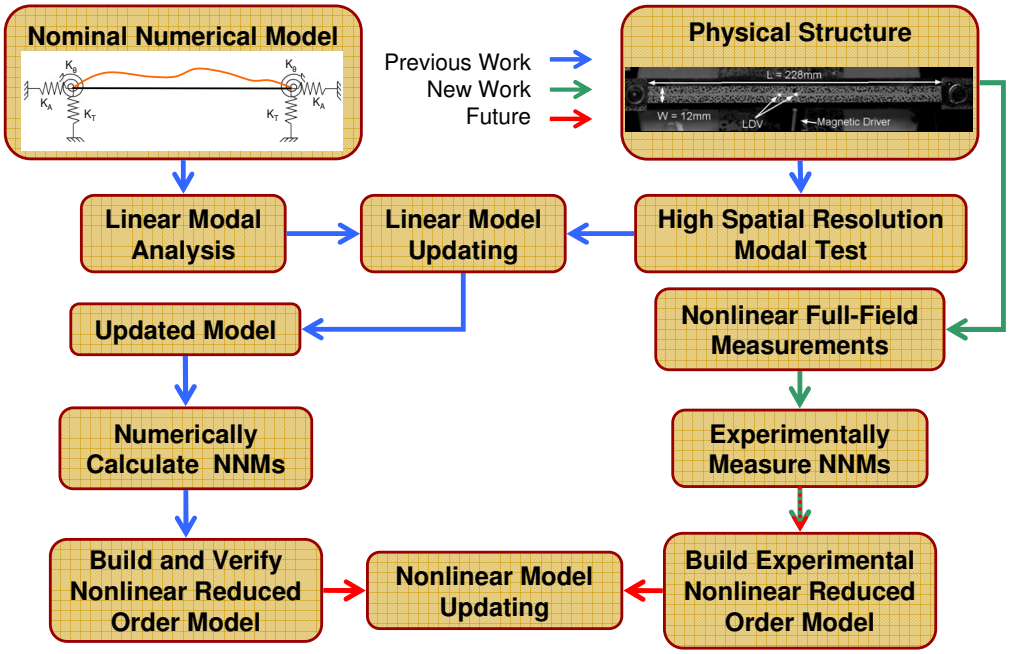

Figure 1.1: Flow chart for nonlinear model updating

1.2 *Full-Field Measurement Techniques*

The development of full-field measurement techniques has received much attention as the design of high-performance light weight structures has advanced. There is an increasing need for experimental techniques capable of measuring a structure's response at a large number of measurement degrees of freedom without modifying the response significantly. Techniques such

as Continuous-scan Laser Doppler Vibrometry (CSLDV) and high-speed Three Dimensional-Digital Image Correlation (3D-DIC) have been developed to meet this need. Both CSLDV and high-speed 3D-DIC are capable of measuring the response at thousands of points across the surface of a structure. However, these techniques involve additional processing to extract velocities or displacements when compared with traditional measurement techniques.

A Laser Doppler Vibrometer (LDV) is a device capable of measuring the velocity of a single stationary point on the surface of a deforming structure by calculating the Doppler shift of the reflected laser light. CSLDV extends the LDV concept by continuously moving the laser by a known pattern across the surface of a deforming structure instead of dwelling at a single location. The motion of the laser requires additional consideration in the experimental setup since, the quality of the reflected laser signal is key to the accurate measurement of velocity and the measurement grid is dependent on the selected scan pattern. Measurements with CSLDV also require an additional processing step when compared with LDV measurements because the continuously moving measurement point requires the measurement to be described by a linear time-varying or, more specifically, linear time-periodic dynamic model [23]. The benefit provided by the continuously moving measurement point is an increased measurement resolution with drastically decreased measurement time when compared with the conventional approach of individually dwelling at a measurement location for a prescribed length of time. Various algorithms have been devised to determine the mode shapes of a structure along a continuously moving laser scan path. For example, Ewins et al. treated the operational deflection shape as a polynomial function of the moving laser position [9, 24-27]. They showed that sideband harmonics appear in the measured spectrum separated by the scan frequency, and that the amplitudes of the sidebands can be used to determine polynomial coefficients describing the

deformation shape. Allen et al. later presented a lifting approach for impulse response measurements [28, 29]. The lifting approach groups the responses at the same location along the laser path. Hence, the lifted responses appear to be from a set of pseudo sensors attached to the structure, allowing conventional modal analysis routines to extract modal parameters from the CSLDV measurements. Recently, Linear Time Periodic (LTP) system theory has been used to derive modal identification algorithms that parallel traditional linear time invariant (LTI) system theory [30-33]. Therefore, a structure's dynamic response due to virtually any type of loading (measured or unmeasured) can be measured over the laser scan path through the use of the input-output transfer functions and power spectrums similar to classical LTI modal analysis.

2D-DIC uses a single camera to match planar deformations throughout a series of captured images and has been widely used in fracture mechanics. 3D-DIC extends this idea to all three spatial dimensions by adding a second camera and a second set of captured images of the deforming surface. Through a series of coordinate transformations, the full-field 3D deformation of a structure is measured [10]. When considering the application of 3D-DIC to the dynamic measurements of structures undergoing large deformation, issues such as lighting, camera placement, field and depth of view for the physical setup are critical to obtain accurate measurements. For sample rates greater than 100 fps, these considerations require measurements to be obtained through an additional step of post processing. Schmidt et al. [34] presented early work on the use of high-speed digital cameras to measure deformation and strain experienced by test articles under impact loadings. Similarly, Tiwari et al. [35] used two high-speed CMOS cameras in a stereo-vision setup to measure the out of plane displacement of a plate subjected to a pulse input. The transient deformations measured compared favorably with work previously published and showed the capability of the 3D-DIC system in a high-speed application, although

over a short time history. Niezrecki et al. [36], Helfrick et al. [37], and Warren et al. [38] measured mode shapes of several structures using discrete 3D-DIC in a frequency range below 200Hz. Niezrecki et al. and Helfrick et al. also combined accelerometers, vibrometers, and dynamic photogrammetry to compare the measured mode shapes and natural frequencies obtained with 3D-DIC. Each technique provided complementary results showing the capability of 3D-DIC, although 3D-DIC was not processed along the entire surface of the structure. Abanto Bueno et al. [39], Beberniss and Ehrhardt [40, 41], and Ehrhardt et al. [42, 43] explored measurement error in full-full field 3D-DIC vibration measurements in frequency ranges up to 1000Hz made on structures subjected to random and sinusoidal loading. In such environments 3D-DIC provided accurate 3D deformation fields of the structures investigated. Due to the extended duration of at test to obtain higher frequency deformations, handling the large amount of data in conjunction with the image files limits the use of 3D-DIC in vibration measurements.

These techniques provide an unprecedented number of measured DOF, allowing one to make a much more informative comparison between test and analysis and provides insight to variations of the underlying physical structure (e.g. variations in initial conditions). This is illustrated in Fig. 1.2, where the first mode of a finite element model of a flat plate considered in this work is overlaid on measurements of the first mode of the flat plate using CSLDV (shown with triangles) and 3D-DIC (shown with squares). For reference between the two plots, the amplitude of deformation is color coded from low (blue) to high (red) amplitude. These results will be discussed in more detail later, but for now it is interesting to note that CSLDV and 3D-DIC provide a comparable number of DOF between the measured and calculated mode shape. It is also of note that the measurement grid differences between CSLDV and 3D-DIC are inherent to their implementation, as will be discussed in Chapter 2. Because these methods provide such

high resolution, we can observe a skew in the measured deformation shape which is not present in the model. This finding suggests that the true structure doe not have the perfect symmetry assumed in the model, and so the model should be updated to account for this; these test results could then be used to determine how much asymmetry should be added. Applying these techniques to measurement of nonlinear deformations also improves the ability to decouple modal interactions at individual harmonics of the response typical at large amplitudes of deformation, as will be discussed in the next section. The first objective of this dissertation is to assess the suitability of CSLDV and 3D-DIC to provide a dense measurement grid in linear and nonlinear modal testing. In Chapter 2, the measurement accuracy and limitations of each system is explored in for small and large amplitudes of deformation. It will be shown that these methods can provide a practical means of measuring the response over a dense array of points on the surface of a structure.

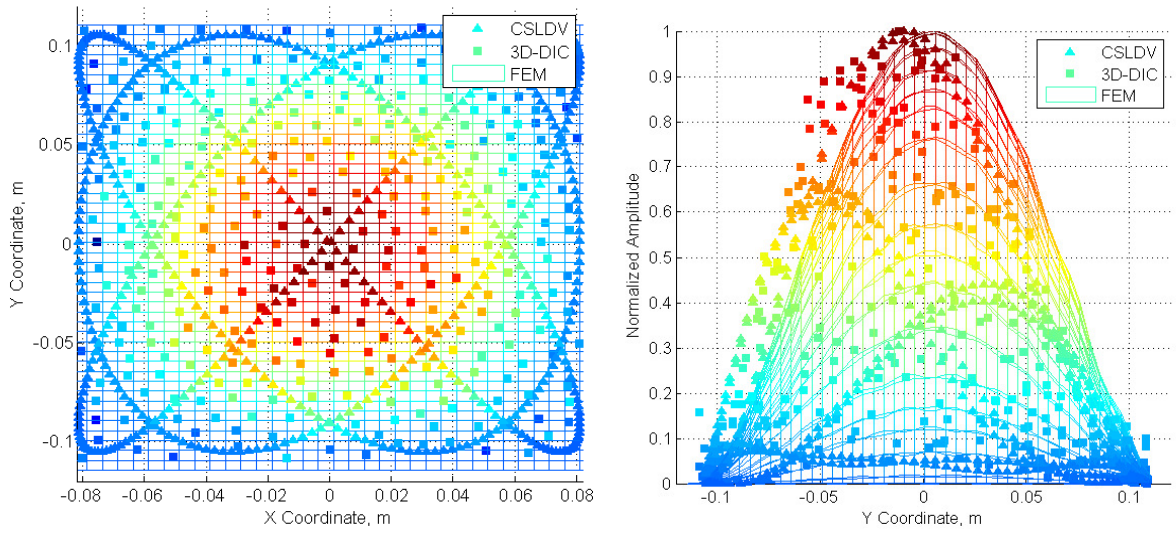

Figure 1.2: Mode 1 of a nominally Flat Plate

1.3 *Nonlinear Normal Modes*

Nonlinearity can present itself in a variety of forms within a structure. For instance, nonlinearities can be distributed throughout a structure and manifest in several ways: geometric

nonlinearity (e.g. large deformations of flexible elastic continua such as beams and plates), inertia nonlinearity (e.g. Coriolis accelerations of translating and rotating bodies), material nonlinearity (e.g. nonlinear stress/strain relationships), or damping nonlinearity (e.g. distributed fluid layer on structure surface). Other nonlinearities occur at discrete locations such as a joint nonlinearity (e.g. dry friction and stick/slip from relative motion of joint) and vibro-impacts (e.g. clearance constraints). Presently, there has been no general test and analysis methodology that can be applied to all nonlinearities since each type of nonlinearity has a distinct mathematical form and give rise to vastly different physics. However, there are several phenomena that are common to many types of nonlinear structures including response amplitude dependence, coupling between linear modes of vibration, and the generation of integer related higher-harmonic responses. The nonlinear normal mode (NNM) concept extends many of the conceptual benefits of linear normal modes (LNMs) to nonlinear systems. Similar to the LNMs previously introduced in Eqns. (1.1) and (1.2), the definition of NNMs is rooted in the conservative homogeneous EOM, which can be written as follows:

$$\mathbf{M}\ddot{\mathbf{x}}(t)+\mathbf{K}\mathbf{x}(t)+\mathbf{f}_{\mathbf{nl}}(x,t) \tag{1.3}$$

Where $\mathbf{f}_{\mathbf{nl}}$ represents the nonlinear stiffness coupling between the displacements which is of particular interest for this dissertation. A NNM is defined as *not necessarily synchronous solutions* of the conservative nonlinear EOM. The extended definition allows NNMs to contain phenomena including bifurcations [12], internal resonances [14], and strong dependence on the amplitude of the response [15]. Due to the complex nature of the dynamics included in a NNM, a graphical depiction of the NNMs is key to their use in test and analysis of nonlinear structures. The use of a frequency-energy plot (FEP) has become relatively standard in the examination of

NNMs [44] and groups 'families' of NNMs with similar dynamic properties together which aids the comparison of experimentally measured and numerically calculated NNMs.

For example, the dynamics of the first 'family' of NNMs of the clamped-clamped flat beam investigated in this dissertation are shown in Fig. 1.3. The FEP in Fig. 1.3b contains two 'families' of NNMs. The first family, shown in blue, is the nonlinear continuation of LNM-1 and is typically termed the backbone branch or NNM-1. Along this backbone, it is observed that the fundamental frequency exhibits a spring hardening dependence on the total energy of the response of the beam or in other words, NNM-1 exhibits an increase of the fundamental frequency vibration with increasing energy. The second 'family' of NNMs, shown in red, is a bifurcation from the NNM-1 backbone and pertains to a 5:1 nonlinear harmonic coupling in the response of the beam. This coupling is known to arise because of interactions between the underlying linear modes of the structure; specifically this branch pertains to a coupling between LNM-1 and LNM-3. On this branch, the deformation shape is a combination of the deformations of the underlying LNMs and higher harmonics in the temporal response are key to understanding this nonlinear coupling.

The dynamic characteristics of these NNMs can be further understood though the examination of the deformation of the beam throughout a quarter period of response (Figs. 1.3c-e) and the Fourier coefficients of center point beam deflection over a period of the response (Figs. 1.3f-h) at selected points along the frequency-energy plot (FEP). Beginning in the linear region of the response, Point 1 shows a LNM-1 deformation of the beam, which is confirmed in the deformation shape and Fourier coefficients of the point. Point 2 refers to the response of the 5:1 harmonic interaction, which contains a primarily LNM-3 deformation of the beam. This can again be confirmed through the examination of the deformation shape and Fourier coefficients

associated with that point. It is important to note that at Point 2, LNM-3 only contributes a small amount to the dynamic response of the beam when compared with the dominant response from mode 1. As energy is increased along this internal resonance branch, LNM-3 contributes more to the dynamic response, and conversely, as energy is decreased along this branch, mode 1 begins to dominate the dynamic response. Finally, Point 3 shows the deformation of the beam at high levels of energy. Here, mode 1 dominates the response, but due to the large transverse deformations at this energy level, axial stretching is observed changing the deformation shape of the NNM. As shown, the presentation of an NNM in an FEP is relatively intuitive, but a large amount of complex structural dynamics is described in this simple plot. Additionally, the evolution of the FEP depends strongly upon which modes interact with the mode of interest along the FEP, which further motivates the use of full-field measurement techniques in nonlinear response regimes to decouple the modal interactions in the response of the structure.

As this new NNM definition has developed, new experimental and analytical techniques have been developed to begin to establish a foundation for nonlinear modal analysis. Traditionally, linear experimental modal analysis techniques can be divided into phase resonance, where one LNM is isolated at a time, or phase separation, where multiple LNMs are excited at once and are decomposed into different frequency components using modal parameter estimation techniques (e.g. the complex mode indicator function, eigensystem realization algorithm, least squares complex exponential, etc.). Similarly, techniques to measure NNMs have focused on extending phase resonance testing techniques to isolate single NNMs [21, 22, 45] and recently, phase separation techniques have been proposed to identify multiple NNMs simultaneously [18, 20, 46]. Current phase separation techniques that characterize a structure's nonlinear response have seen limited implementation on experimental structures as they are

generally formulated around relatively low DOF nonlinear systems, include a challenging system identification step, and require some knowledge of the nonlinearity in a structure. Other researchers have proposed a more general system identification process that removes the need of knowledge of the nonlinearity [19]. However, these phase separation techniques rely on the damped response of structures, so it can be difficult to identify purely nonlinear stiffness effects. Therefore, the focus of this dissertation is on the implementation of phase resonance methods to measure NNMs through the implementation of different methods of force appropriation.

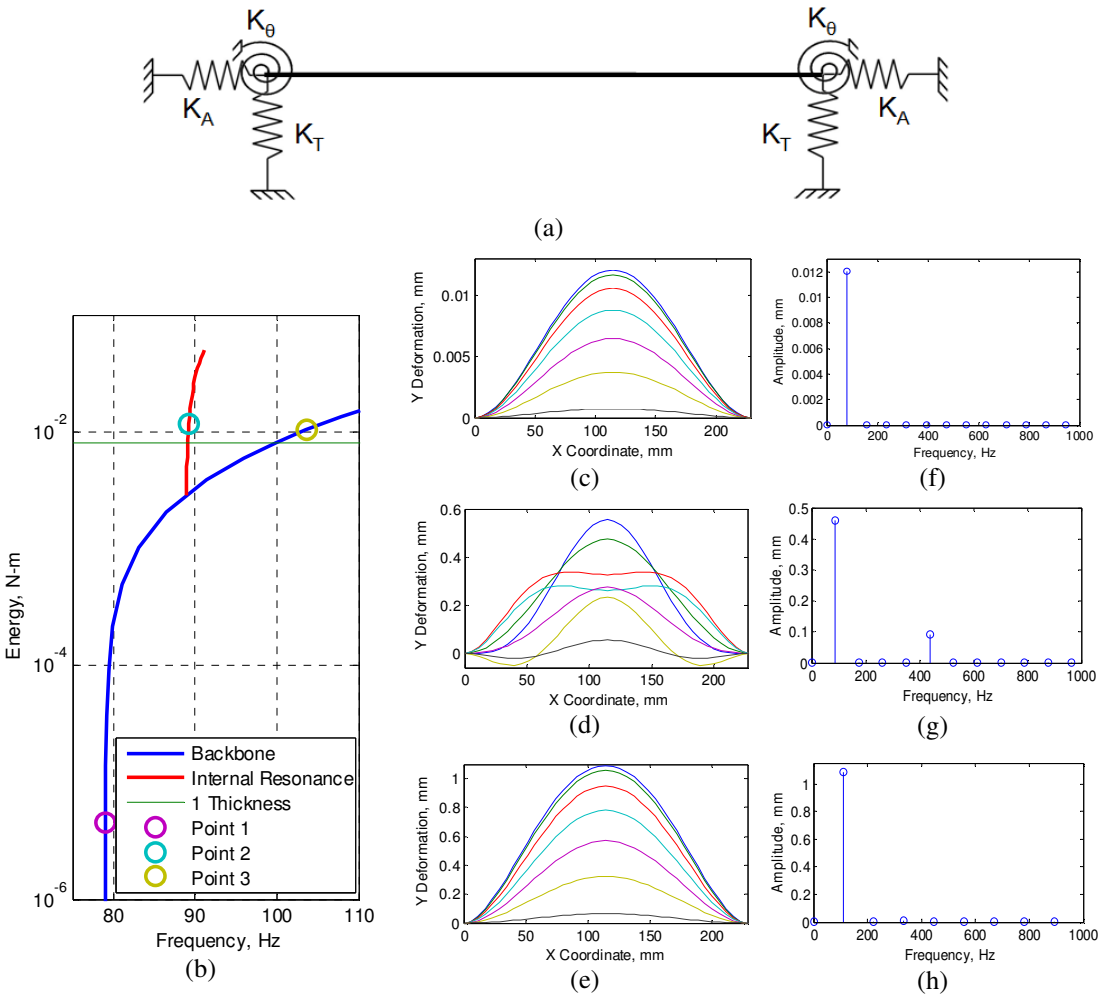

Figure 1.3: Dynamic properties of the first NNM of a flat beam (Kuether et al.). a) Schematic of flat beam. b) Frequency-energy plot, c-e) Deformation shapes for a quarter period (— 0%, — 4%, — 8%, — 12%, — 16% , — 20%, — 25% of the period) at selected points along the FEP f-h) FFTs of selected points along the FEP

Atkins et al. [22] presented a force appropriation of nonlinear systems (FANS) method using a multi-point multi-harmonic force vector to isolate a linear normal mode (LNM) of interest. This permits the direct nonlinear characteristics of the isolated mode to be calculated without modal coupling terms. Peeters et al. [16, 21] showed that a multi-point multi-harmonic sine wave could isolate a single NNM. For application to real world structures, it was then demonstrated that a single-point single harmonic force could be used to isolate a response in the neighborhood of a single NNM with good accuracy [16, 47]. In these investigations, once phase lag quadrature was met, the input force was turned off and the response allowed to decay tracing the backbone of the NNM. Building off of this work, Ehrhardt et al. [48] used step sine testing to measure the response around a specific NNM and at several input forcing levels leading to nonlinear frequency response functions (FRFs). From these FRFs, responses in the neighborhood of the NNM can be isolated from measured responses. Similarly, using manually tuned stepped sine excitation, Ehrhardt et al. [45] showed the ability to isolate a NNM through incrementally increasing force levels and adjusting the frequency of the input force to experimentally measure a NNM. This method drastically reduces the amount of data measured while isolating a NNM, making the implementation of full-field measurements feasible.

For the calculation of nonlinear normal modes (NNMs), several analytical and numerical techniques are available. Analytical techniques, such as the method of multiple scales [12, 13, 49, 50] and the harmonic balance approach [15], are typically restricted to structures where the equations of motion are known in closed form, so analysis is limited to simple geometries. This dissertation is focused on realistic (e.g. FEM) models for a structure where the analytical methods are not usually practical. To expand the calculation of NNMs to more complex geometries, asymptotic [51] and continuation based [12, 13, 52] numerical methods have been

developed to calculate NNMs of discrete systems. Recently, numerical methods based on continuation have also been extended to calculate NNMs of larger scale structures [52-54] using MATLAB® coupled with a commercial FEA code such as Abaqus®. Of interest for this dissertation, Kuether et al. [52] proposed a direct method to compute the NNMs of full-ordered models termed the applied modal force (AMF) algorithm. Similarly, Allen et al. [55] used nonlinear reduced order models (NLROMs) to calculate the NNMs of a structure, allowing NNMs to be calculated of more complex structures at a modest computational cost.

Typically, the fundamental frequency of vibration of the NNM is presented as a function of the total energy (kinetic + potential) of the structural response in the form of FEPs as previously shown in Fig. 1.3. In an experimental environment, the measurement of energy is not convenient, so the FEP of a structure is represented as a plot of the maximum amplitude of the structural response versus the fundamental frequency of vibration. A comparison of the experimentally measured and numerically calculated NNM1 backbone is show in Fig. 1.4, where the experimentally measured (left) and numerically calculated (right) NNM provide complementary results for this structure as will be further discussed in Chapter 3. In Fig. 1.4, NNM-1 shows that when the deformation of the flat beam investigated approaches 1 mm, the fundamental frequency of vibration increases from 64Hz to 95 Hz, or the structure becomes more stiff at higher deformation amplitudes changing the dynamic characteristics of the response. FEPs present the complex dynamics of NNMs compactly for experimental or numerical data, motivating their use as a model calibration metric. The second objective of this dissertation is to use NNMs as qualitative and quantitative metrics for model calibration.

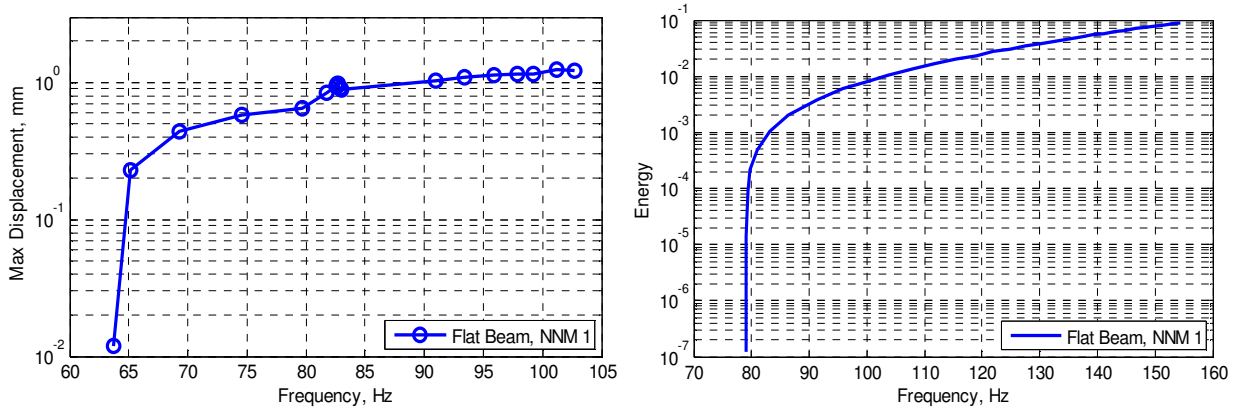

Figure 1.4: Experimental frequency-maximum deformation plot of beam (Left). Numerical frequency-energy plot of beam (Right).

1.4 *Proposed Test and Analysis Methodology*

This work proposes the use of continuous-scan laser Doppler vibrometry (CSLDV) and 3-dimensional digital image correlation (3D-DIC) to measure nonlinear normal modes (NNMs) of geometrically nonlinear structures using manually tuned single point multi-harmonic excitation where frequency and amplitude of the input force are adjusted to track a NNM. A flow chart describing the model calibration procedure used and the work completed for this dissertation is shown in Fig. 1.5. LNMs and NNMs were measured and calculated on structures provided in collaboration with the Air Force Research Lab (AFRL) at Wright Patterson Air Force Base and Cummins Emissions Solutions (CES) in steps (**1-6**). Using the resulting LNMs and NNMs, the models were updated to accurately capture the structural dynamics in linear and nonlinear response regimes in steps (**7-8**). Finally, the models are being validated through the use of linear and nonlinear response measurement and simulation in step (**9**). The following provides an in depth discussion of the structures investigated, the tasks completed and avenues of future work.

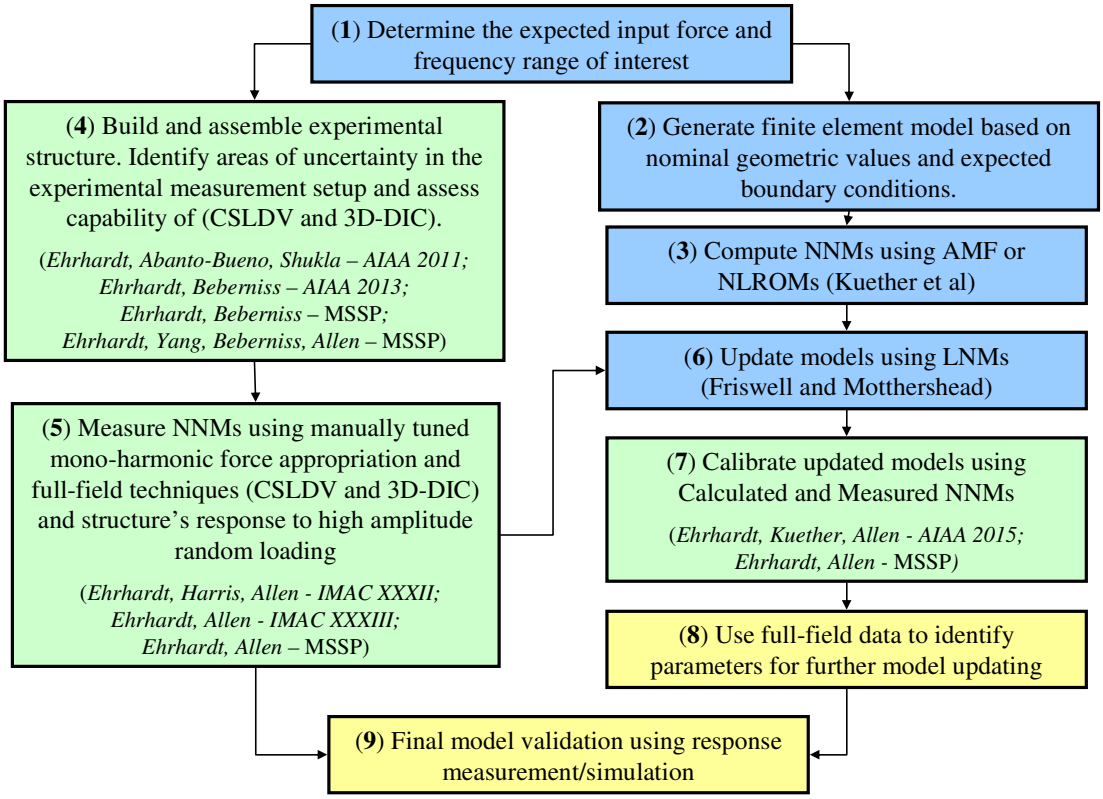

Figure 1.5. Flow chart for proposed thesis on calibration with NNMs. (Blue) represents tasks that are considered previously completed, and will not be further developed in this thesis, (Green) represents tasks completed to date, and (Yellow) are potential areas of future work.

The numerical models and physical structures of interest for this thesis have been provided in collaboration with the AFRL and CES. The physical structures include a flat beam, curved beam, rectangular flat plate, and an axi-symmetric perforated plate as shown in Fig. 1.6. Each beam is made from high carbon steel and undergoes surface preparation for use with 3D-DIC (black and white speckles) and CSLDV (grey retro reflective tape). The flat beam has a length, width, and thickness of 228.6mm, 12.7mm, and 0.762mm and for the curved beam, length, width, and thickness are 304.8mm, 12.7mm, and 0.51mm, respectively. The curved beam has an additional curvature of 3000mm, which is not obvious in the image provided, but will be shown with more detail in Chapter 4 of this dissertation. The flat plate is made of aluminum and

has a length, width, and thickness of 228.6mm, 177.8mm, and 0.51mm. The surface of the flat plate was also prepared for use with 3D-DIC (black and white speckles) and CSLDV (grey retro-reflective tape). This plate is of particular interest to the AFRL and has been used in combined environment loading conditions to aid in the design of aircraft panels. The curved axi-symmetric plate has a diameter and thickness of 304.8mm and 1.52mm. Due to the perforations, the surface of the axi-symmetric plate was only prepared for 3D-DIC since CSLDV requires a continuous surface. This plate is of particular interest to CES and is used as an acoustic damper in heavy industrial exhaust components.

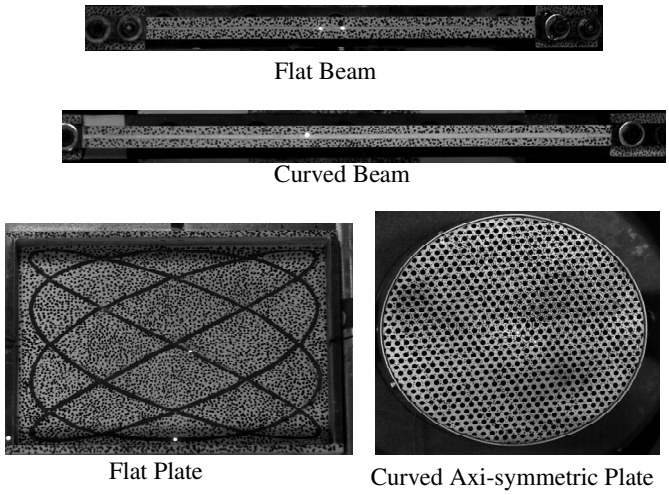

Figure 1.6: Four Structures that will be used to evaluate the proposed model updating strategy

Through the use of the Vibration Testing Facility at the AFRL, tests have been performed to identify and quantify areas of potential error in the experimental setup fulfilling step (**4**) in Fig. 1.5. This work extends the use of CSLDV and 3D-DIC to measure full-field structural responses in linear and nonlinear response regimes. Additionally, the NNMs of each structure have been measured in the same facility using a novel, manually tuned multi-harmonic force appropriation procedure in step (**5**). Through the subsequent adjustment of input forcing amplitude and frequency, CSLDV and 3D-DIC were used to measure the full-field deformations

along the NNM backbone curve. In collaboration with the AFRL and CES, FEMs based on nominal geometry and boundary conditions have also been provided in step (**2**), and through the use of recently developed methods [52, 56], NNMs have been calculated for each baseline model in step (**3**). Using the full-field static measurements taken with 3D-DIC and measured full-field LNMs of the structures, the initial geometry, boundary conditions, and material properties of each model have been updated (**6**). The compact presentation of NNMs in an FEP have been used to validate the linearly updated models, fulfilling step (**7**).

For future work, the final steps of the model calibration procedure, step (**8**), can be completed by using the measured full-field dynamic data at all harmonics in the response to identify the nonlinear modal interactions in the structures. A final model validation step can then be performed using additional measured and simulated response data, completing step (**9**) and the model calibration process.

1.5 *Scope of the Dissertation*

The dissertation is organized as follows. Chapter 2 introduces the CSLDV and 3D-DIC measurement systems and compares the relative merits of each technique in the measurement of linear and nonlinear dynamic responses. It is shown that each technique is capable of providing a dense measurement grid when used to measure the dynamic response of a flat beam and flat rectangular plate The suitability of CSLDV and 3D-DIC in the nonlinear model updating frame is also explored here. In Chapter 3, the concept of NNMs is presented in more detail with a specific focus on their measurement as applied to a flat beam and a curved axi-symmetric plate. Previous work has detailed the numerical calculation of NNMs, so only a brief summary is

presented. Using the experimentally and numerically determined NNMs, a qualitative validation is performed on a flat beam and a curved beam through updating their boundary conditions and material properties and is presented in Chapter 4. Chapter 5 provides a summary of the dissertation and Chapter 6 identifies future work that has been uncovered in the development of this dissertation.

2 The use of Continuous-scan Laser Doppler Vibrometry and 3D Digital Image Correlation for Full-Field Linear and Nonlinear Measurements

2.1 *Introduction*

The development of non contact full-field measurement techniques has received increased attention as the design of high-performance structures has advanced. Due to complex geometries and the lightweight nature of these structures, there is an increasing need for experimental techniques capable of measuring the response at a large number of degrees of freedom without modifying the structural response significantly. Techniques such as Continuous-Scan Laser Doppler Vibrometry (CSLDV) and high-speed Three-dimensional Digital Image Correlation (high-speed 3D-DIC) have been developed to meet this need. Both CSLDV and high-speed 3D-DIC are non-contact, non-destructive, and capable of accurately measuring the dynamic response at thousands of points across the surface of a structure. Both techniques are also capable of providing "real-time" measurements, but this has seen limited to no implementation for several reasons. In the case of 3D-DIC, significant computational power is needed to move and manipulate the thousands of image files sampled for each test. For CSLDV, real time measurement is theoretically feasible with the implementation of the harmonic power spectrum algorithm, but to the best of the authors knowledge this has never been done. For this work, these limitations are avoided by post-processing the data acquired with both methods.

2.2 *Continuous-scan Laser Doppler Vibrometry*

CSLDV is an extension of traditional Laser Doppler Vibrometry (LDV), where the laser point, instead of dwelling at a fixed location, is continuously moving across a measurement

surface. Therefore, obtaining vibration frequencies and deformation shapes from CSLDV signals is more challenging than from LDV signals since the moving measurement location requires the system to be treated as time-varying. Though this motion complicates the post-processing, the benefit provided by the continuously moving point is an increased measurement resolution with a drastically decreased measurement time when compared with traditional LDV. Several algorithms have been devised to determine a structure's deformation along the laser scan path. For example, Ewins et al. treated the operational deflection shape as a polynomial function of the moving laser position [9, 25-27, 57, 58]. They showed that sideband harmonics appear in the measured spectrum, each separated by the scan frequency, and that the amplitudes of the sidebands can be used to determine the polynomial coefficients. Allen et al. later presented a lifting approach for impulse response measurements [29, 59]. The lifting approach breaks the CSLDV signal into sets of measurements from each location along the laser path. Hence, the lifted responses appear to be from a set of pseudo sensors attached to the structure, allowing conventional modal analysis routines to extract modal parameters from the CSLDV measurements. However, this method works best when the laser scan frequency is high relative to the natural frequencies of interest, and for some structures this increase the measurement noise too much to be practical. Recently, algorithms based on Linear Time Periodic (LTP) system theory [23, 60-64] were developed and used to derive input-output transfer function and power spectrum relationships from CSLDV measurements allowing the extraction of a structure's deformation from impulse, random, and sinusoidal excitations. When a structure is vibrating sinusoidally, many of the methods simplify significantly and in this paper the simplest method will be used based on Fourier analysis as was presented by Stanbridge, Martarelli, Ewins and Di Maio [9, 25-27, 57, 58], and which is called the Fourier series expansion method in [59].

The first step in the use of CSLDV is the selection of a scan pattern. Scan patterns can range from simple lines and circles to complex Lissajous curves and trajectories. The selection of a pattern is not limited to periodic patterns only, as methods have been developed that are capable of measuring velocities if the pattern is aperiodic [26]. Methods developed for aperiodic scan patterns are limited to sinusoidal or impulse excitation, which is applicable in this work; however, an aperiodic scan pattern would interfere with the use of 3D-DIC. Instead the use of periodic 1-D line and 2-D Lissajous curve patterns are used so that the mode shape will be a periodic function of time [59, 63] and hence the surface doesn't need to be fit to a polynomial in the spatial coordinates as is typically done in [9, 25-27, 57]. The selected periodic patterns are scanned across a surface using a single point fiber optic LDV and external mirrors, as shown in Fig. 2.1. Grey retro-reflective tape cut in the shape of the scanning pattern, a line for the beam (Fig. 2.6) and a Lissajous curve for the plate (Fig. 2.12), is added to the structures investigated to reduce signal contamination from a structure's surface and improve measurement feedback. With the completion of the scan, the LDV measurement is now a collection of time-periodic velocities of the surface deformation in the defined z-direction.

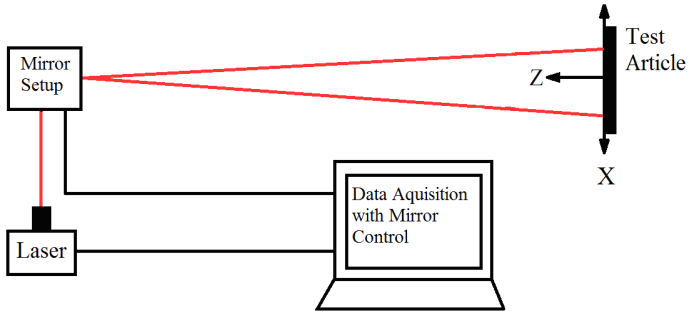

Figure 2.1: CSLDV System Diagram: The laser beam was redirect by a pair of mirrors to continuously scan on the test article

The implementation of a time-periodic CSLDV scan pattern couples the motion of the measurement point with the deformation of the structure. Therefore, additional processing is

required to separate the motion from the structural deformation in order to reconstruct the vibration shapes. Consider the measurement of vibration along a single axis (the z-axis in this instance) with a single point sensor. The measured response $\mathbf{z}(x,y,t)$ of a linear time invariant (LTI) structure subjected to a single frequency force input is harmonic at the same frequency, f, but with a different phase and amplitude at each point, so it can be written as follows.

$$\mathbf{z}(x,y,t) = \mathrm{Re}(\mathbf{Z}(x,y)e^{i2\pi * f * t} \tag{2.1}$$

Here x and y represent the sensor position on the surface. If CSLDV is used with a periodic scan pattern, the measured response becomes time periodic, $\mathbf{z} = \mathbf{z}(x(t),y(t),t)$, as follows

$$\mathbf{z}(x(t),y(t),t) = \mathrm{Re}(\mathbf{Z}(x(t),y(t))e^{i2\pi * f * t} \tag{2.2}$$

where the x- and y-coordinates change in time based on the predefined periodic motion

$$\begin{aligned} x(t) &= A_x \cos(2\pi f_x t) \\ y(t) &= A_y \sin(2\pi f_y t) \end{aligned} \tag{2.3}$$

For the Lissajous patterns used here, the period T_A of the scan pattern is determined by both x- and y- scan frequency, as defined in Eqn. (2.4), and modifying the values for f_x and f_y changes the density of the pattern across the scan.

$$T_A = \frac{1}{f_A} = N_x * T_x = N_y * T_y = N_x * \left(\frac{1}{f_x}\right) = N_y * \left(\frac{1}{f_y}\right) \tag{2.4}$$

As the amplitude $\mathbf{Z}(x(t),y(t))$ is periodic, it can be represented with a Fourier Series as shown below.

$$\mathbf{Z}\big(x(t),y(t)\big) = \mathbf{Z}(t) = \mathbf{Z}\big(t+T_A\big) = \frac{1}{2}\sum_{n=-\infty}^{\infty}\mathbf{Z}_n e^{in2\pi * f_A t} \tag{2.5}$$

The periodic motion of the laser couples with the structural deformation inducing a periodicity in the measurement. Inserting the Fourier series description of the deformation shape into Eqn. (2.2), one obtains the Fourier description of the CSLDV signal shown in Eqn. (2.6); the measured response using CSLDV includes motion at the input frequency and an infinite number of harmonics separated by the scan frequency f_A. Since the laser scan path is known, the deformation of the structure can be recovered by measuring the amplitudes of all of these harmonics, following a procedure similar to that which was presented in [63].

$$\mathbf{z}(x(t), y(t), t) = \mathbf{Z}(x(t), y(t))e^{i2\pi ft} = \frac{1}{2}\sum_{n=-\infty}^{\infty}\mathbf{Z}_n e^{i2\pi(f+nf_A)t} \tag{2.6}$$

2.3 *Three-Dimensional Digital Image Correlation*

To accurately measure 3D displacements with DIC, a setup using two cameras is used to image the test article as it deforms. As shown in Fig. 2.2, the two cameras are placed at a specific distance along the Z-axis from the test article to allow the surface to be captured simultaneously in each camera and establish a field of view. A pan angle, Θ_p, is specified based on a desired depth of view or range of out-of-plane displacements expected [65].

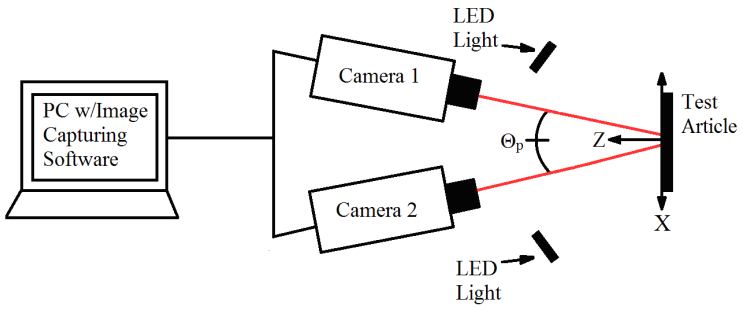

Figure 2.2: 3D-DIC System Diagram**.** The 3D-DIC system diagram shows Camera 1 (left camera) and Camera 2 (right camera) set to a specified pan angle, Θ_p.

Once the stereo camera setup is assembled and fixed, principles of triangulation are used to establish each camera's position in reference to the global experimental coordinate system as defined by:

$$\begin{bmatrix} x_{Camera} \\ y_{Camera} \\ z_{Camera} \end{bmatrix} = \mathbf{R} \begin{bmatrix} x_{Global} \\ y_{Global} \\ z_{Global} \end{bmatrix} + \mathbf{T} \tag{2.7}$$

Where **R** is the rotation matrix and **T** is the translation matrix for the coordinate system transformation. Additionally, lens distortion and variations between the sensor of the camera and the final images can be corrected through a bundle adjustment [10]. The coordinate system transformation matrix is established through the use of images of a rigid known pattern or calibration panel. With this calibration, the accuracy of the coordinate transformation matrix is not limited to the pixel size of the imaged surface of the test specimen, but instead can be interpolated on the sub pixel level (e.g. resolutions of about 0.03 pixels have been obtained [34]). Once the calibration of the 3D-DIC system is established, images of the fully deformable structure can be analyzed to obtain displacements. To achieve a sub pixel accuracy in the determination of displacements, the surface of the structure is divided into areas of pixels or subsets. Each subset in turn is fit with a surface following the form of:

$$\begin{bmatrix} A \\ B \end{bmatrix} = \begin{bmatrix} x \\ y \end{bmatrix} + \begin{bmatrix} a \\ b \end{bmatrix} + \begin{bmatrix} \partial a/\partial x & \partial a/\partial y \\ \partial b/\partial x & \partial b/\partial y \end{bmatrix} \begin{bmatrix} \Delta x \\ \Delta y \end{bmatrix} + \begin{bmatrix} \partial^2 a/\partial x \partial y \\ \partial^2 b/\partial x \partial y \end{bmatrix} \Delta x \Delta y + \begin{bmatrix} \partial^2 a/\partial x^2 & \partial^2 a/\partial y^2 \\ \partial^2 b/\partial x^2 & \partial^2 b/\partial y^2 \end{bmatrix} \begin{bmatrix} (\Delta x)^2 \\ (\Delta y)^2 \end{bmatrix} \tag{2.8}$$

Where A and B are the final deformed coordinates of the center of the subset, x and y are the original coordinates, a and b are the rigid translation of the subset and the three remaining matrices correspond to an affine, irregular, and quadratic deformation of the subset, respectively. Using a correlation algorithm, each subset is matched through each imaged deformation providing out of plane displacement accuracies on the order of 0.03 pixels (or 10 μm for the field-of-view used in this work) depending on the correlation algorithm used. In-plane deformations are measured with a greater accuracy when compared with purely out-of-plane deformations since these deformation are less reliant on the higher order fit. Prior to testing, a high-contrast random gray-scale pattern is applied to the measurement surface so the defined subsets can be uniquely and accurately fit. As detailed in [10], triangulation of the subset matching is used to determine the coordinate value of each measurement point.

An example of the measurement of a out of plane rotation is shown in Fig. 2.3. During characterization of the 3D-DIC system a measuring coordinate system as shown in Figs. 2.3a and 2.3b is established. Images are captured throughout deformation as shown in Figs. 2.3c and 2.3d. Using the image captured in the un-deformed condition for Camera 1 (Fig. 2.3a), subsets of the image are established. Subset matching is performed between the un-deformed condition for Camera 1 and the un-deformed condition for Camera 2 (Fig. 2.3b). As the test article experiences deformation, images are captured with each camera simultaneously. Subset matching is then performed between the un-deformed image of Camera 1 (Fig. 2.3a) and the deformed image of Camera 1 (Fig. 2.3c). Once the subsets have been established in the deformed image of Camera 1 (Fig. 2.3c), a second stage of subset matching is performed between the deformed image of Camera 1 (Fig. 2.3c) and the deformed image of Camera 2 (Fig. 2.3d). An out-of-plane rigid body rotation about the Y-axis of the un-deformed test article (Figs 2.3a and 2.3b) is shown in

Figs. 2.3c and 2.3d. Again, using the surface fitting previously described, this procedure allows subsets to be matched between the simultaneous images captured with sub-pixel accuracy. In-plane displacements, or motion in the X-Y plane, can be measured with the same order of accuracy as with a 2D-DIC system as mentioned before. The addition of the second camera allows the out-of-plane displacements to be measured with accuracy on the order of 0.03 pixels [34].

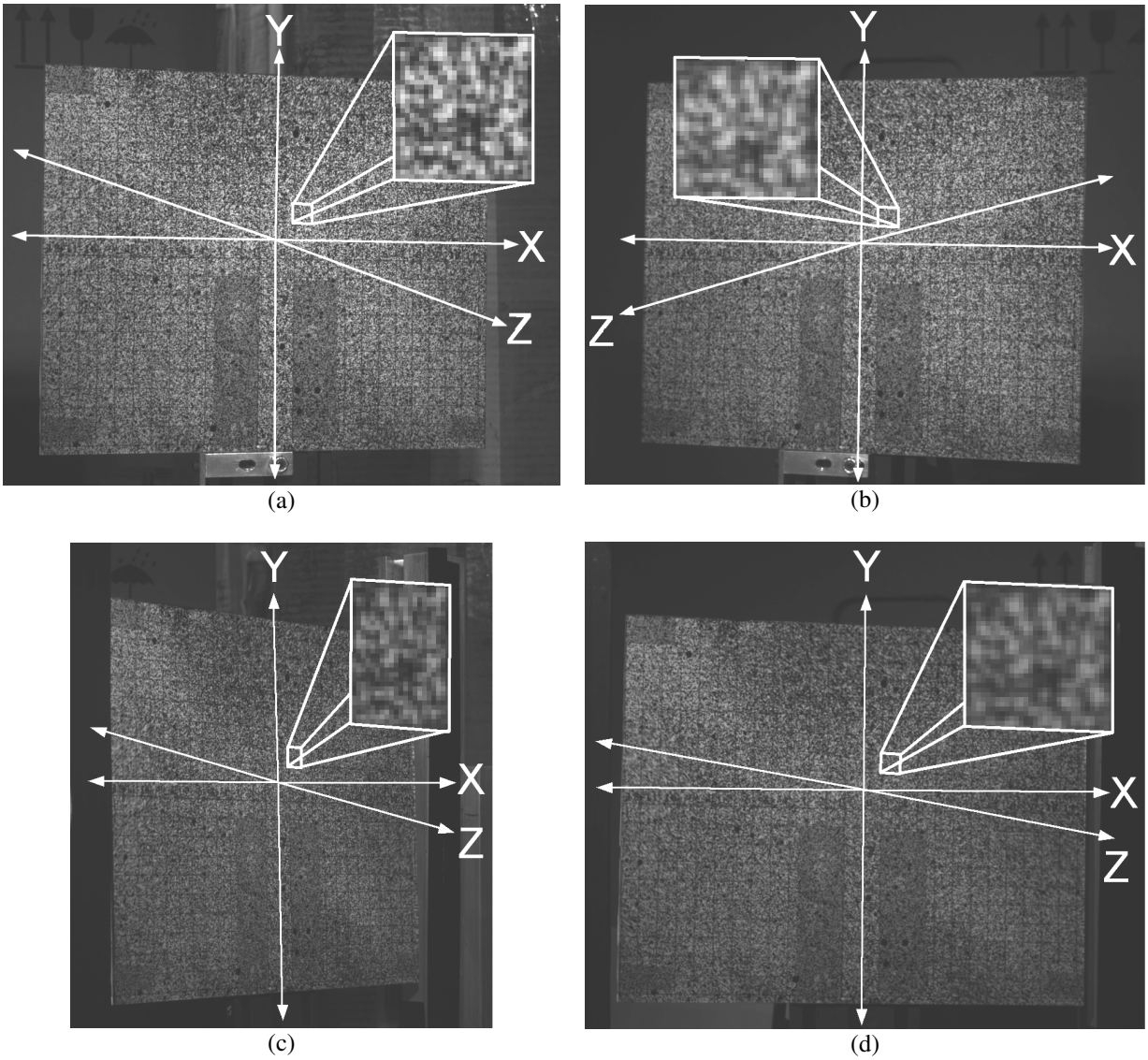

Figure 2.3: 3D-DIC Out-of-Plane Deformation Measurements. a) Left camera un-deformed image. b) Left camera deformed image, c) Right camera un-deformed image, d) Right camera deformed image

One difficulty in a 3D-DIC setup is establishing uniform lighting over large out-of-plane deformations experienced by the test article. Since uniform lighting is hard to establish, accuracy in out-of-plane measurements vary with Z distance from the test article. Also, to establish the 3D measuring coordinate system, a system characterization that is more involved than the 2D case is needed. Typically 10-20 images of a plate with a known pattern is subjected to a rigid-body displacement in the desired measuring volume to create the 3D measuring coordinate system.

2.4 *Experimental Setup*

The physical experimental setup is shown in Fig. 2.4. In this setup, there are four main systems: 1) exciter/ controller, 2) static 3D-DIC system, 3) dynamic 3D-DIC system, and 4) the CSLDV system.

1) Excitation was provided by two separate exciters, both controlled in an open-loop using a Wavetek Variable Phase Synthesizer. The low amplitude excitation was provided by an Electro Corporation 2030 PHT magnetic pickup which was given a high voltage input from a Piezo Amplifier. This induces a localized magnetic field providing a near single point input force to ferrous materials. If non-ferrous materials are used or more force is required, a thin magnetic metal dot can be added to a structure. The force exerted by the magnetic pickup was measured using a force transducer mounted to a solid base between a solid base and the magnetic pickup providing measurement of the reaction force with the base. Large amplitude excitation was provided by shaking the base of the structure's clamping fixture which was mounted on a 5000N MB dynamics shaker. However, this type of excitation provides symmetric inertial loading at a constant acceleration and limits the ability to examine asymmetric motion of the structure. The voltage input to the exciter was measured as well as the input force for the magnetic driver and the base acceleration for the shaker. The velocity response and input voltage signals were

analyzed in real time using a Onosoki FFT Analyzer to track the phase between the signals. Here, the input voltage was used instead of the measured force/acceleration to limit noise contamination from the measurement sensors. However, the measured force/acceleration signals were compared after measurement to ensure the correct phase relationship between input and response was maintained. The structure's fundamental frequencies in linear and nonlinear response regimes could then be determined by adjusting the frequency until the input voltage and response velocity are 180 degrees out of phase.

2) The static 3D-DIC system consists of two Prosilica GT2750 CCD cameras with a full resolution of 2750 x 2200 pixels with a maximum frame rate of 20 fps. For this experimental setup, full resolution images were used since the amount of available memory in the cameras was not limited and to include the greatest amount of pixels in the measurement . The static system uses 18mm lenses and is positioned at a standoff distance of 580mm with a camera angle of 26 degrees. All static displacements were determined using a commercial 3D-DIC software Aramis using subsets of 31x31 pixels with a 13 pixel overlap across the entire surface of the plate. A 250mm x 200mm calibration panel was used to establish the measurement volume and lead to a calibration deviation of 0.032 pixels for this camera resolution or 0.004 mm for this field of view.

3) The dynamic 3D-DIC system includes two Photron, high speed 12-bit CMOS cameras (model Fastcam SA5 775K-M3K). Each camera has 32GB of memory onboard with a maximum resolution of 1024×1024 pixels. For each experimental setup, image size was adjusted to fit as much of the structure in the frame of both cameras. The dynamic system uses 85mm lenses at a stand off distance of 1370mm with a camera angle of 24.4 degrees. All dynamic displacements were determined using a software extension of Aramis called IVIEW Real Time Sensor [66]

using subsets of 15x15 pixels. In order to minimize the heat generated and remove the electrical noise produced by the lighting systems that are typically used in high-speed DIC systems, two 305×305 LED light panels were used. The cameras and the data acquisition system were simultaneously started using an external TTL trigger. Measurement points were selected to avoid the retro-reflective tape, so there is no overlap of measurements between CSLDV and 3D-DIC. This was done to reduce the measurement noise previously seen in the static measurements and provide better tracking for the DIC algorithm. A 250mm x 200mm calibration panel was used to establish the measurement volume and lead to a calibration deviation of 0.02 pixels for this camera resolution or 0.007 mm for this field of view.

4) The continuous-scan mechanism was built using a Polytec OFV-552 fiber optic laser vibrometer with a sensitivity of 125 mm/s/V and the same external mirror system that was used in [29]. The mirrors were positioned at a stand off distance of 2.4m, which was selected to minimize the scan angle, which was a maximum of 7.3 degrees in x-direction and 5.4 degrees in y-direction for both setups, and yet keep the laser close enough to maintain a high quality signal. The external mirror system consisted of two galvanometer scanners in open-loop control; each scanner had a position detector that measured the instantaneous rotation angle, allowing precise and accurate control and measurement of the laser position. The control and data acquisition system was built using a National Instruments PXI system. A LabVIEW program was developed to integrate several features including the function generator, data acquisition, and signal processing. The line and Lissajous patterns used for this investigation have a x-direction scan frequency of 3 Hz and the y-direction scan frequency is 4 Hz. Data was collected at each steady state response level with a sampling frequency of 10,240Hz for 2 minutes.

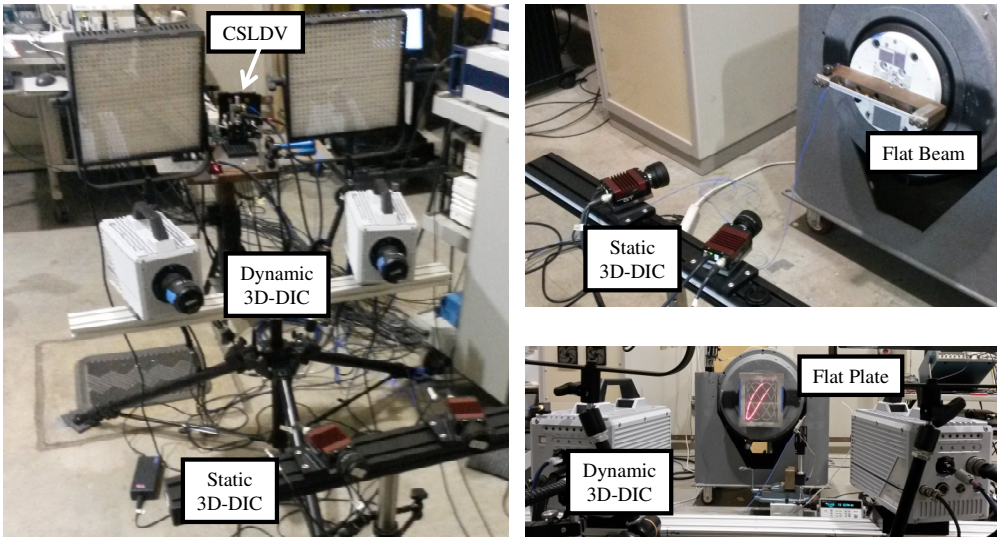

Figure 2.4: Experimental Setup.

2.5 *Measurement of Linear and Nonlinear Response of a Clamped-Clamped Flat Beam*

2.5.1 Beam Description

The first structure under test is a precision-machined feeler gauge made from high-carbon, spring-steel in a clamped-clamped configuration, as was previously studied in [67]. The beam is assumed to be flat and has an effective length of 228.6mm, a nominal width of 12.7mm, and a thickness of 0.762mm. Using nominal dimensions and material properties, the first three linear mode shapes were calculated and are presented in Fig. 2.5. All dimensions are nominal and subject to variation from clamping and from the machining process to obtain the desired thickness.

Prior to clamping, the beam was prepared for three dimensional digital image correlation (3D-DIC) and continuous-scan laser Doppler vibrometry (CSLDV) as discussed in [42] and shown in Fig. 2.6a. Locations of the initial laser Doppler vibrometry (LDV) positions are also shown at the center of the beam and 12mm to the left of the center measurement. The clamping

force was provided by the two 6.35-28 UNF-2B bolts tightened to 90 in-lbs. Before and after clamping the beam in the fixture, static 3D-DIC was used to measure the initial curvature of the clamped beam and the result is shown in Fig. 2.6b. It is interesting to note that although the beam is assumed to be nominally flat, before and after clamping the beam has an initial deflection of 4% and 0.01% of the beam thickness, which is not obvious during clamping. This change of initial curvature has little effect on the linear results, but could change the characteristic nonlinearity of the beam (e.g. softening to hardening effect). Additionally, single-input single-output modal hammer tests were performed throughout testing on the beam to identify natural frequencies and damping ratios. Results from these hammer tests showed a 0.7% variation in the first natural frequency of the final clamped beam, which can be expected due to a small amount of slipping or temperature variation in the room.

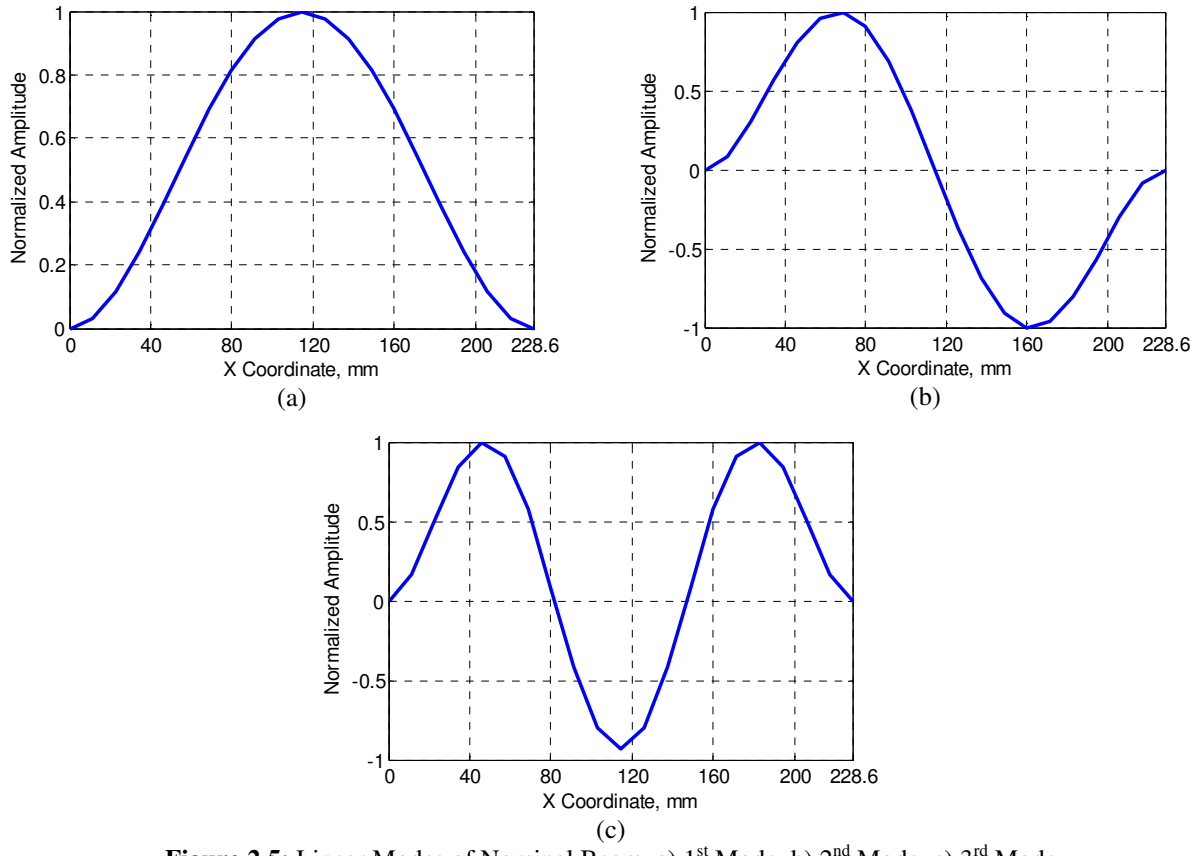

Figure 2.5: Linear Modes of Nominal Beam. a) 1st Mode, b) 2nd Mode, c) 3rd Mode

In order to measure the deformation of the beam in one setup, an understanding of the limitations of each setup is needed. For instance, 3D-DIC loses measurement capabilities at small deformations, so although the minimum measurement resolution is 0.007 mm, displacements at this level will be contaminated with noise. CSLDV is sensitive to large deformations since the measurement is one dimensional, and will be contaminated with cross-axis deformation in the beam. So, for the best signal to noise ratio for 3D-DIC and minimal cross-axis deformation in the structure, the beam was driven at the largest force that allowed a linear response in the beam. This force was determined by incrementally increasing the input force level while monitoring damping. When damping increased a measurable amount, the force was decreased to the previous forcing level. The maximum resulting response was 62% of the beam thickness.

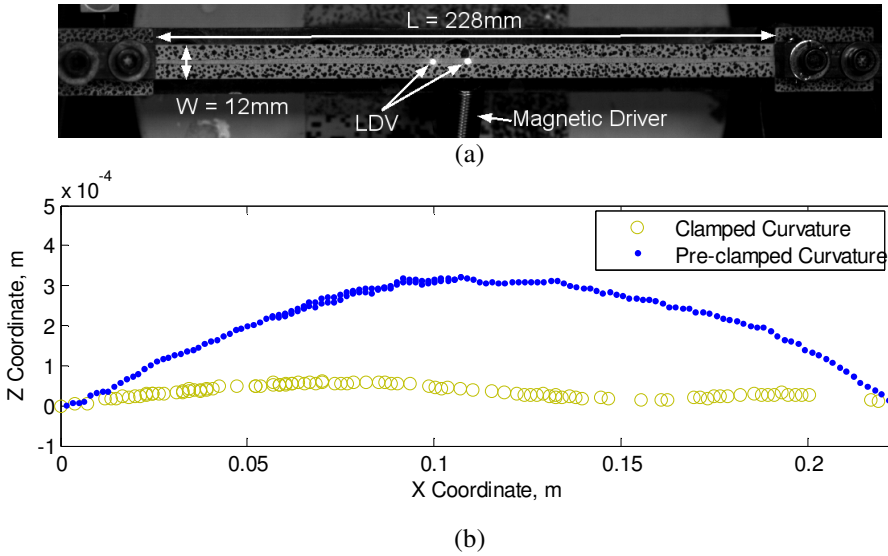

Figure 2.6**:** Beam Specimen. a) Final clamped-clamped configuration, b) Initial clamping deformation

In order to measure the deformation of the beam with one measurement system setup, an understanding of the limitations of each measurement system is needed. For instance, measurements with 3D-DIC become contaminated with noise at small deformations as a result of

sensor limitations of the imaged surface area. Also, measurements with CSLDV can become contaminated with noise at small deformations due to the added speckle noise from the moving laser point. Additionally, the cameras used for 3D-DIC need to be able to 'see' the deforming surface to make a measurement possible which limits the amount of deformation the structure can undergo. Also, the laser used for CSLDV will disperse more when the structure undergoes large deformation also limiting the amount of deformation the structure can undergo. Therefore, special consideration is needed when setting the field- and depth-of-view for 3D-DIC and when selecting the scanning frequency and stand off distance for CSLDV so both systems can simultaneously measure the deformation of the structure when undergoing small or large deformations. Alternatively, 3D-DIC and CSLDV measurement setups can be chosen so one can measure smaller deformations and one can measure larger deformation with an overlap where both systems can measure the deformation of the structure. For this experimental setup, the latter case is true and deformations on the order of 0.02 mm are the low end for 3D-DIC, where CSLDV can measure down to 0.0002 mm. No upper limit is identified for the structures investigated since the structures investigated would have been damaged at this high level of deformation. To find the area of measurement overlap the beam was driven at the largest force that allowed a near linear response in the beam. This force was determined by incrementally increasing the input force level while monitoring damping. When damping increased a measurable amount, the force was decreased to the previous forcing level. The maximum resulting response was 62% of the beam thickness which is a weakly nonlinear level.

2.5.2 Linear Response Comparison

The clamped beam was driven using mono-harmonic sinusoidal forcing at each of the first three natural frequencies identified with the single-input single-output modal hammer tests.

The beam's steady state response under these forcing conditions was measured using high-speed 3D-DIC and CSLDV. Fig. 2.7(a) shows an example of the response spectrum from 3D-DIC measured at the center of the beam when it is forced at the first natural frequency. Only the out-of-plane displacements are shown for 3D-DIC since the axial and transverse displacements are in the noise of the measurement. As expected, a single harmonic is seen in the response at 71.3Hz, which is the forcing frequency. Fig. 2.7 (b) shows an example of the response spectrum from CSLDV measured as the laser scans the beam's surface. In addition to the primary harmonic of the response at 71.3Hz, several side-bands are observed in the response spectrum each separated by the scanning frequency of 3Hz. As previously discussed, an infinite number of sidebands are expected for CSLDV, but Fig. 2.7(b) shows sideband harmonics higher than the 6th order are buried in the noise floor. So, no harmonics above the 6th order were used when construction the mode shape. The Fourier coefficients for harmonics of n = -6:6 were then used to construct the mode shape along the laser path. The second and third bending mode shapes were reconstructed using the Fourier coefficients that stood out about the noise floor, which ended up being harmonics n=-10...10 and n=-15...15.

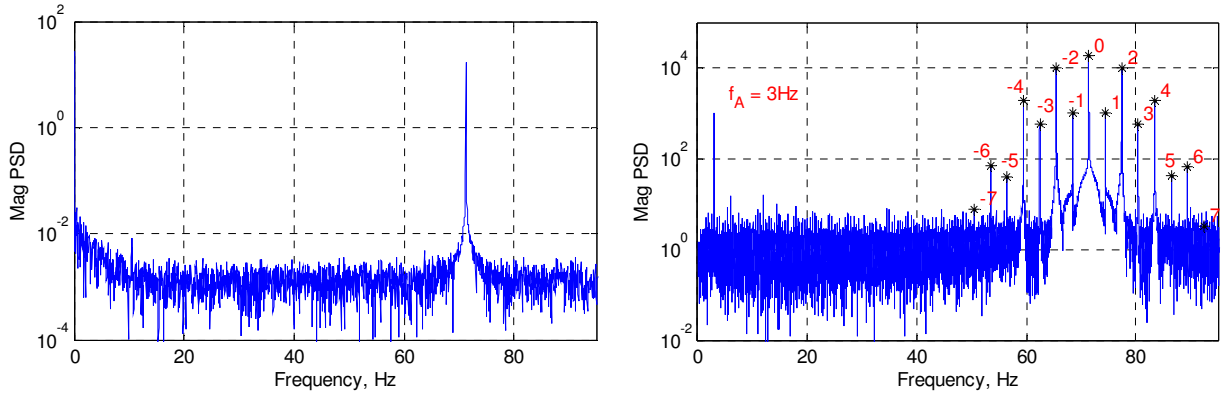

Figure 2.7**:** Linear Response Spectrum Comparison. 3D-DIC (Left) and CSLDV (Right)

Figure 2.8 compares the mode shapes obtained by CSLDV and 3D-DIC when exciting near each of the three resonance frequencies. Figure 2.8a contains the mode shape at 71.3Hz and shows the difference between the mode shapes measured with CSLDV and the measurement points obtained with high-speed 3D-DIC. Similarly, Fig. 2.8b and 2.8c show the mode shapes at 205.5Hz and 411.4Hz. The MAC values between DIC and the CSLDV shapes are shown in Tab. 2.1 along with the frequency errors previously discussed. It is noted that MAC values for modes 1 and 2 are above 0.99 showing excellent correlation between CSLDV and high-speed 3D-DIC; for the third mode at 411 Hz the maximum displacement was only 0.21mm measured at 411.4Hz, high-speed 3D-DIC begins to exhibit larger errors in the mode shape, which is shown in Fig. 2.8c, leading to a MAC value of 0.6572.

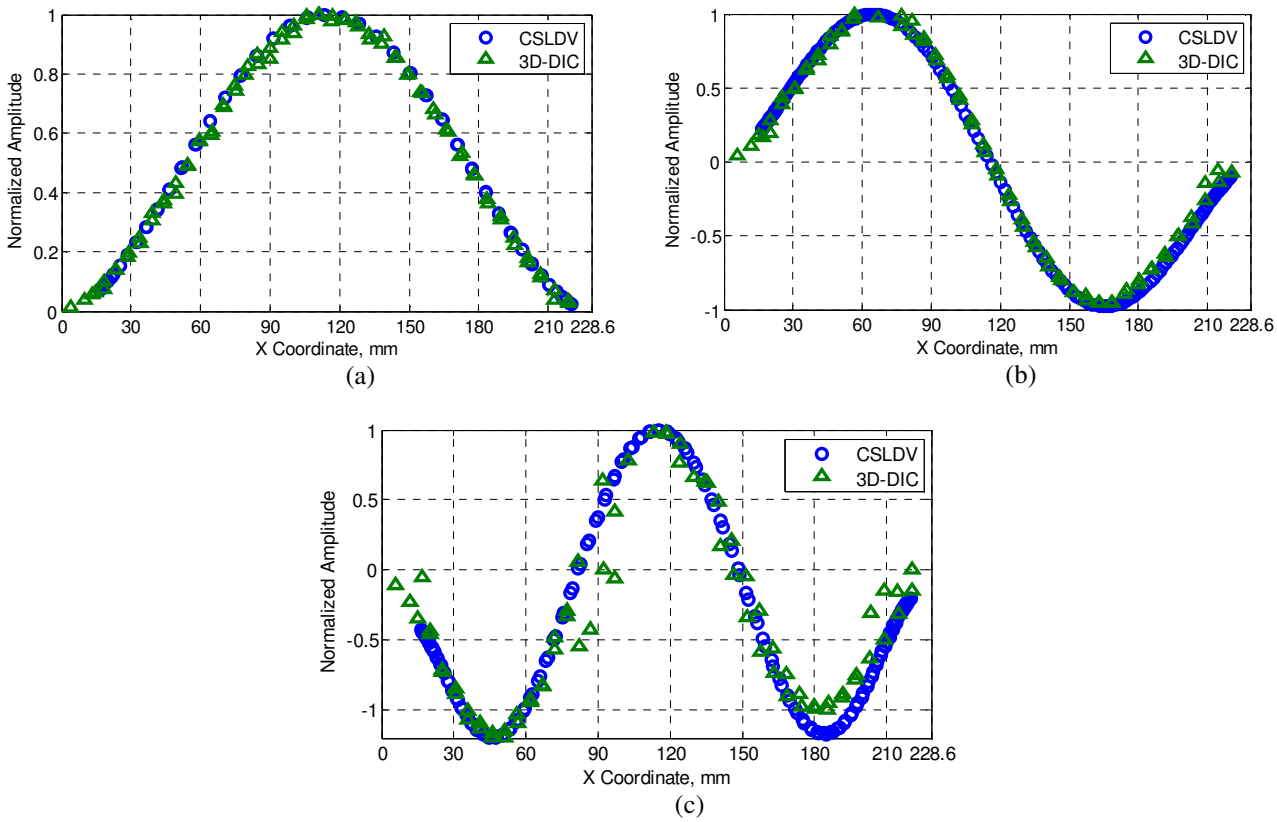

Figure 2.8**:** Modes shapes from Steady State Excitation. a) Mode 1 at 71.3Hz, b) Mode 2 at 204.5Hz, and c) Mode 3 at 411.4Hz.

Table 2.1**:** Modal Comparison

	Mode	f_n AVG Modal Hammer Test, Hz	% Change between Pre- and Post- Experiment Modal Hammer Tests	f_n CSLDV, Hz	% Error CSLDV	f_n DIC, Hz	% Error DIC	MAC
Sinusoidal	1	71.75	-0.70	71.24	-0.7112	71.30	-0.6269	0.9995
	2	204.35	-0.49	204.33	-0.0117	204.50	0.0747	0.9981
	3	411.45	-0.12	411.05	-0.0972	411.39	-0.0134	0.6572

Additionally an asymmetry is seen in the mode shapes of modes 2 and 3 which is believed a result of asymmetry of the boundary conditions or the initial curvature in the beam. Both measurement methods capture the asymmetry in mode 2, but the asymmetry for mode 3 is apparently not detected as accurately in CSLDV as with 3D-DIC. The accuracy of each method is difficult to ascertain for the measurement of mode 3 since 3D-DIC begins to lose measurement resolution and higher harmonics from CSLDV measurements are buried in the noise of the laser signal. In either case, the asymmetry would be undetectable unless the dynamic response is observed with the large number of measurement points.

It is also important to note that while the smooth nature of the CSLDV mode shapes seems to suggest that they are infallible, they are in fact an approximation of the true mode shapes obtained by expanding them in a Fourier series of the time-varying scan pattern. The accuracy of the reconstructed mode shape depends on the number of harmonics included in the Fourier series approximation. As mentioned previously, thirteen clearly dominant harmonics (i.e. n=-6...6) were observed for the first mode. The neglected harmonics were at least a few orders of magnitude smaller than the dominant ones, so one would be inclined to have high confidence in that shape. The harmonics n = -8...8 were also used to reconstruct the first bending mode shape,

the results was only 0.068% different from the shape that was shown which used harmonics n = -6...6. Furthermore, because the laser is scanning along a line with CSLDV, when the measurements are noisy, the mode shapes measured on the forward and backward parts of the sweep tend to differ giving an indication of the error. Here, the forward and backward sweeps overlay completely suggesting that the shapes shown are quite accurate.

2.5.3 Nonlinear Response Comparison

As a structure is pushed towards the nonlinear regime, a single harmonic input force results in a multi-harmonic response. Figure 2.9 shows the resulting nonlinear response spectrum for 3D-DIC and CSLDV. For 3D-DIC, 10 harmonics of the forcing frequency can be easily identified in the measured response. The additional harmonics seen in the 3D-DIC response near 140 Hz can be attributed to previously identified fan noise from the camera cooling fans. As discussed later, the deformation shape at all 10 harmonics cannot be fully visualized for 3D-DIC due to variations in the measurement across the surface, especially when the response has small displacement. For CSLDV, the scanning laser permits the identification of 7 harmonics of the forcing frequency in the measured response. Due to increased laser dispersion from the 3Hz motion of the laser the noise floor is increased reducing the ability to identify all 10 of the fundamental harmonic components. Also, at higher harmonics, the deformation shape of the beam becomes more complex, so more side band harmonics are needed to reconstruct the deformation shape of the beam. However, the added noise of the scanning laser reduces the ability to identify side band harmonics in the measured response.

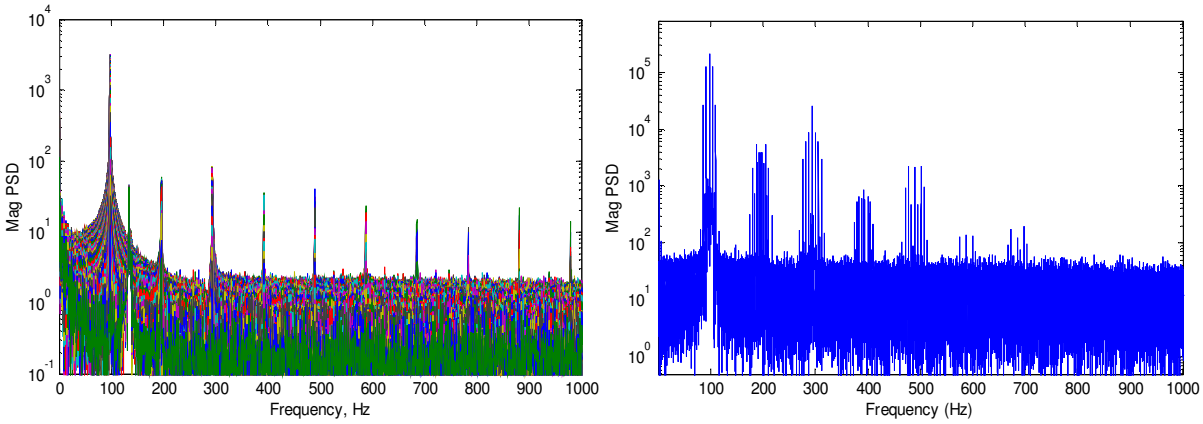

Figure 2.9**:** Nonlinear Beam Response Spectrum Comparison. (Left) 3D-DIC and (Right) CSLDV

Full-field measurements of a deforming structure, such as this beam, are especially beneficial for nonlinear deformations since the spatial deformation of the beam can be identified at each harmonic. These measurements can then in turn be used in model updating to identify nonlinear coupling in the beam's modes. Fig. 2.10a-e shows the deformation patterns along the beam for selected harmonics. Fig. 2.10a shows the first harmonic of the response, or the fundamental harmonic, which resembles the first linear mode of a flat beam as expected. There is a small shift in the deformation of the first harmonic made with CSLDV and 3D-DIC, but both systems correctly show a zero deformation at the clamps of the beam. Each measurement system establishes an independent reference coordinate system, and this shift corresponds to a 6 degree rotation about the y-axis of one of the measurement systems relative to the other. This is certainly within the uncertainty in the alignment of the two measurement systems. Fig. 2.10b shows the second harmonic of the response, which resembles the second linear mode of a flat beam, with a factor of two difference between the peak deformation of each lobe. The maximum

deformation of this harmonic is 0.013mm, which apparently causes 3D-DIC to begin to lose measurement resolution in this and subsequent harmonics. Fig. 2.10c shows the third harmonic of the response, where the deformation resembles a superposition of mode 1 and mode 3 of the beam. Again, 3D-DIC appears to lose measurement resolution at these small displacements, but the basic deformation shape is still captured. Fig. 2.10d shows the fourth harmonic of the response which does not resemble a linear mode of vibration. At this harmonic 3D-DIC completely loses ability to measure the beam deformation and CSLDV begins to loose accuracy, as is manifest in the difference between the shapes measured in the forward and backward sweeps. Fig. 2.10e shows the fifth harmonic of the response which occurs at a higher level of deformation than the fourth. Therefore, 3D-DIC is able to capture the response but the measurement resolution is still reduced. The amplitude of this harmonic is higher than the fourth, but the deformation pattern is more complex, so CSLDV also shows variation in the forward and backward sweeps for this mode. For the low levels of deformation presented here, CSLDV outperforms 3D-DIC in capturing these spatial deformation shapes.

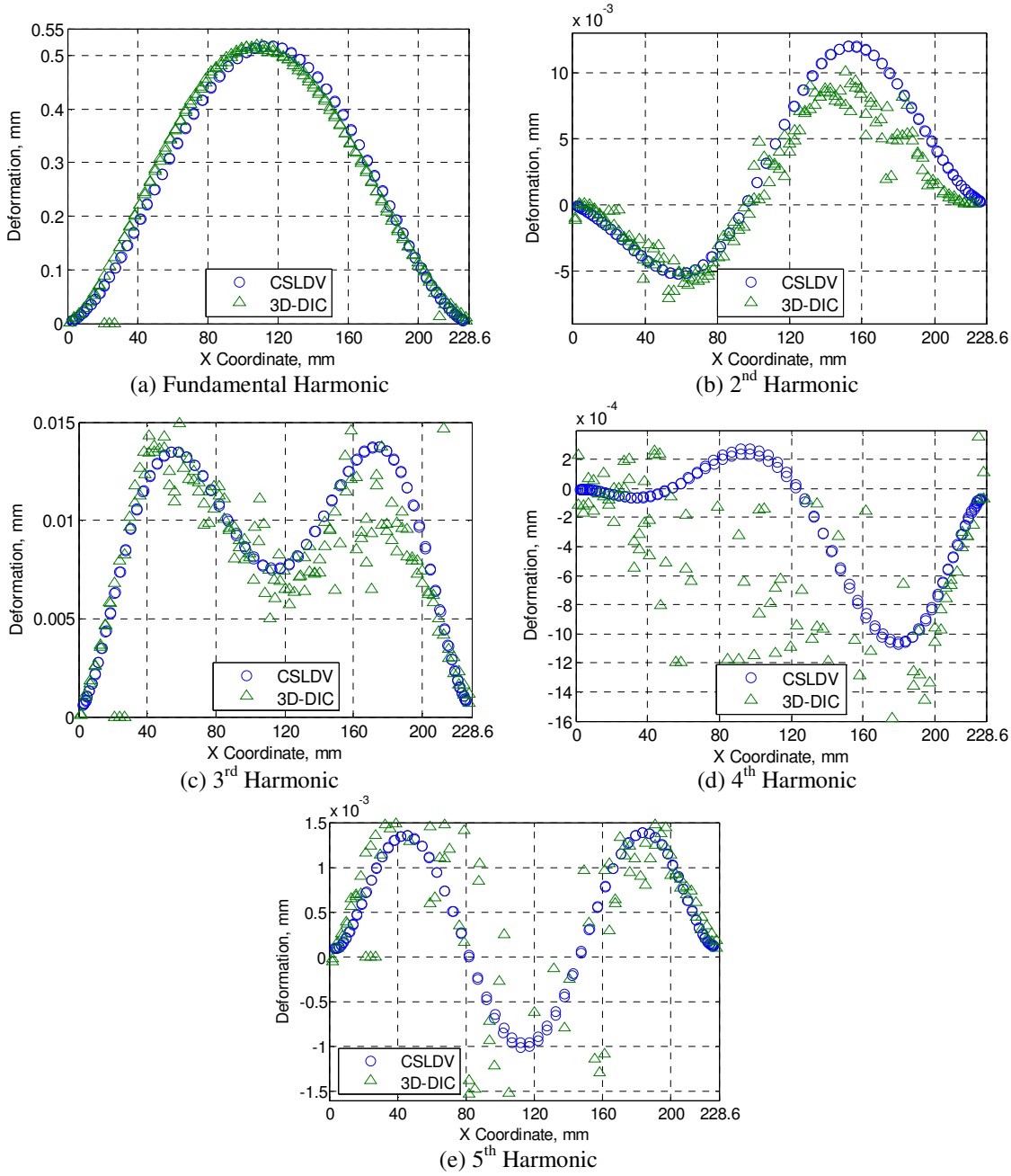

Figure 2.10: Deformation pattern for each harmonic in the response of the beam.

2.6 *Measurement of Linear and Nonlinear Response of a Clamped Flat Plate*

2.6.1 Flat Plate Structure

The second structure under test is a nominally flat clamped aluminum plate. The tested plate had an effective length of 177mm, an effective width of 228mm, and a thickness of 0.5mm.

Using the nominal dimensions and material properties, linear mode shapes were calculated for the plate and is shown in Fig. 2.11, where the deformation of each mode is color coded from smallest (blue) to largest (red); however, dimensions are nominal and subject to change, so mode shapes are subject to variation in an experiment.

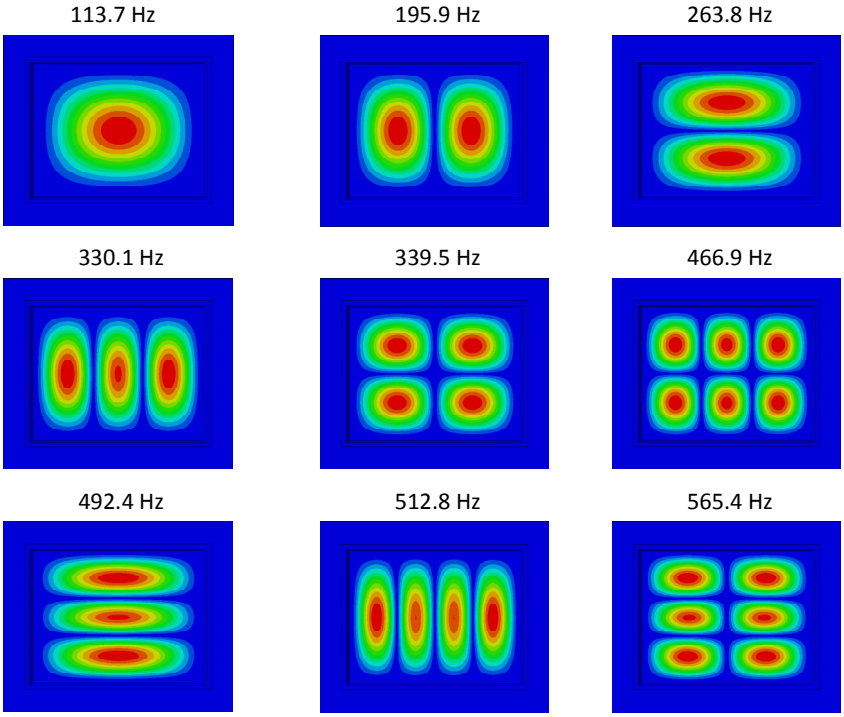

Figure 2.11: Flat Plate Linear Mode Shapes

The plate was then clamped between two mounting frames with adhesive as further described in [68]. After being fixed between the mounting frames, the plate was painted with a white base coat, and a speckle pattern, with an average diameter of 5 pixels, was applied using a marker and spray paint to increase the imaged surface texture and improve tracking for both 3D-DIC systems. Once the plate had dried, a pattern of retro-reflective tape (dark grey loop in Fig. 2.12a) cut from a printed Lissajous stencil was added to increase feedback to the CSLDV laser while not covering the rest of the plate so that 3D-DIC could be used in those areas. The final

prepared plate is shown in the clamping fixture in Figure 2.12a. For an accurate description of the initial conditions of the plate, static 3D-DIC images were captured after the plate was fully clamped. An initial deflection of 0.613 mm near the center of the plate was measured, as shown in Figure 2.12b, where the color bar corresponds to the defined z-coordinate from smallest (blue) to largest (red). One can see that the retro-reflective tape and the edge of the mounting frame have a negative effect on the ability of 3D-DIC to compute the static coordinates at certain positions, but the measurement density is high in other regions so it is not difficult to interpolate over the anomalies that these introduce. The final step of preparation was the addition of a 6mm steel disk to the back of the aluminum plate to allow input force from a magnetic driver, discussed in the next section. The location of this disk is shown in Fig. 2.12a.

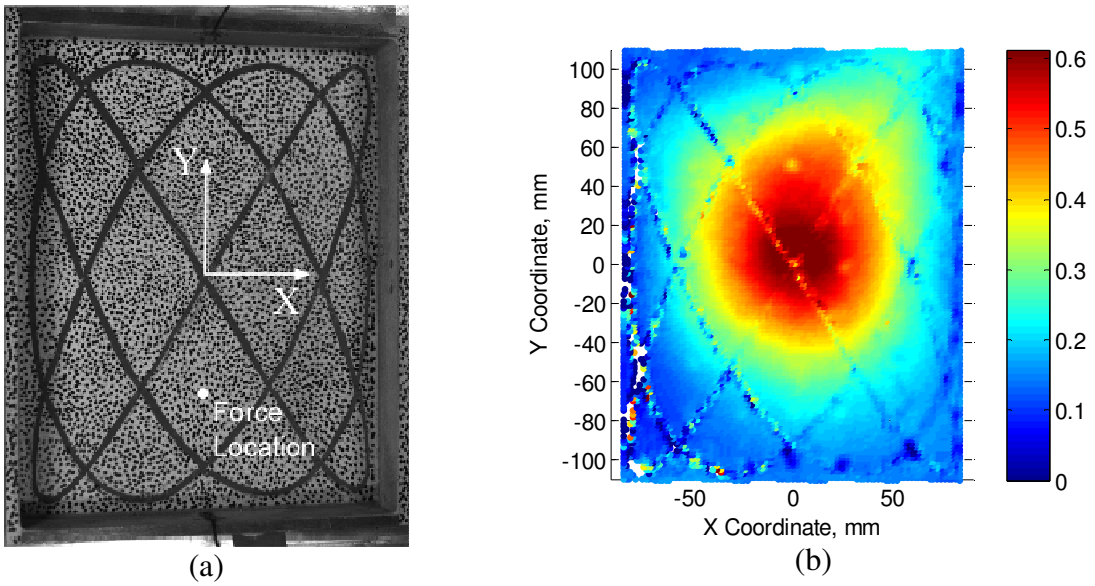

(a) (b)

Figure 2.12 : Images of Rectangular Plate: a) Final prepared surface, b) Measured initial curvature. The color bar gives the Z coordinate in mm

Table 2.2: Plate linear frequencies

Mode	f_n AVG Modal Hammer Test, Hz	% Change in Modal Hammer Tests	f_n CSLDV, Hz	% Error CSLDV	f_n DIC, Hz	% Error DIC
1	106.5	0.65	106.9	0.3756	106.7	0.1878
4	276.5	0.43	275	-0.5425	275.1	-0.5063

2.6.2 Linear Plate Response Comparison

Force appropriation was used to drive the plate at the first and fourth natural frequencies and the steady state response was measured using both CSLDV and high-speed 3D-DIC. Fig. 2.13 shows an example of the spectrum from the CSLDV signal with a scan frequency of 1Hz when the plate was driven at 106.9Hz and 277.7Hz. For mode 1 and mode 4, the sideband harmonics higher than the 14th and 32nd order, respectively, are in the noise of the signal, as seen in the power spectral density (PSD) plots in Fig. 2.12a and 2.12b, and hence no harmonics above these orders were used when constructing the mode shapes. It is important to note that more than twice as many harmonics are needed to reconstruct a 2D shape when compared with the 1D line. For a 2D Lissajous curve like this, it becomes harder to take the time to check all of the harmonics in the signal or tell when they are or are not reasonable to include in the reconstructed shape.

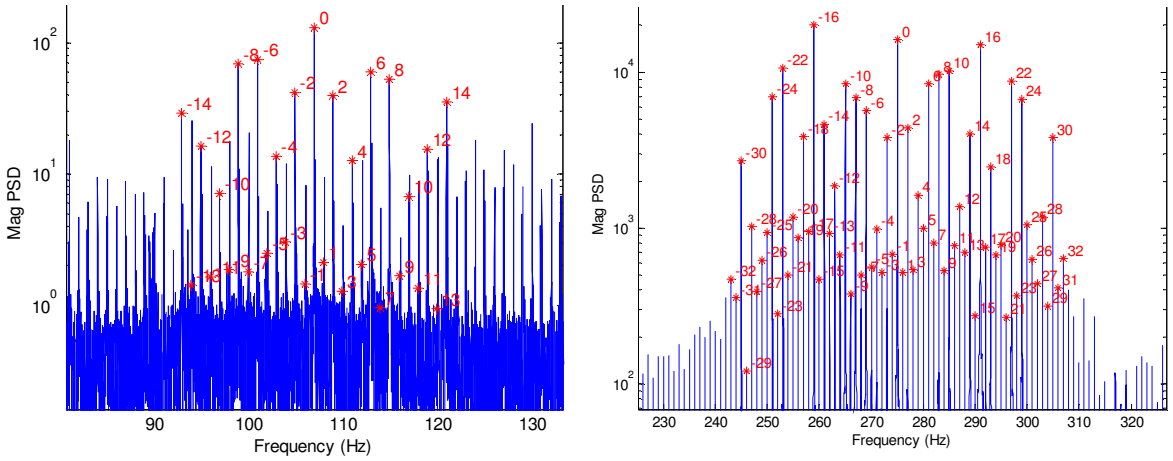

Figure 2.13: Power Spectra of CSLDV signals for (Left) mode 1 and (Right) mode 4

Fig. 2.14 compares the mode shapes obtained by CSLDV (triangles) and 3D-DIC (squares) for the two linear steady state experiments where the plate was excited with the magnetic driver. Figures 2.14a & 2.14b contain the mode shape at 106.9Hz, with the amplitude

color coded from low (blue) to high (red) amplitude. Although the defined measurement grids for CSLDV and 3D-DIC don't overlap, both measurements show good agreement between both techniques. Since there are no directly overlapping measurement points, MAC values cannot be calculated to compare the measured shapes, so only a qualitative comparison is made. The focus of this work was on modes of a rectangular plate that would be excited with the use of symmetric loading (i.e. in the application of interest the aircraft panels are excited by uniform pressure loads), so the next linear mode examined was mode 4. Since mode 4, is symmetric it can be excited with base excitation from the larger shaker. Figures 2.14c & 2.14d contain the mode shape at 277.70 Hz and again show good agreement between measurements.

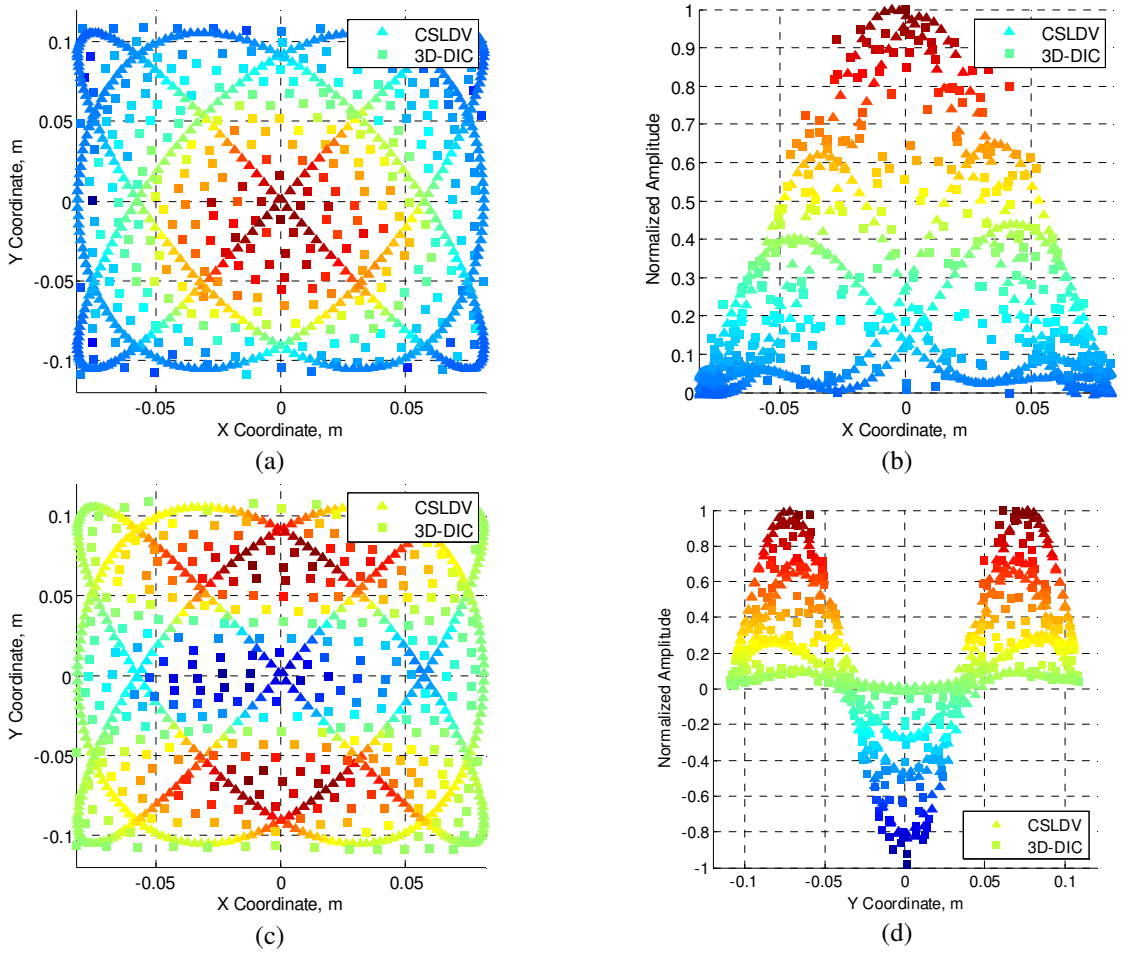

Figure 2.14: Mode Shape Comparison between CSLDV and 3D-DIC. a) & b) Mode 1, c) & d) Mode 4

2.6.3 Nonlinear Plate Response Comparison

Similar to the nonlinear excitation provided to the flat beam, the flat plate is excited at a large amplitude near the first resonant frequency. Since the plate is larger than the beam, a 5300 N shaker is used to provide base excitation to the flat plate. The deformation shapes at each harmonic are reconstructed with CSLDV using 32 sideband harmonics, the same number that was used previously with the 4^{th} linear mode shape. As is generally the case for a structure such as this [69], the primary harmonic of the measured nonlinear response, at 160.8Hz, resembles the first linear mode of a flat rectangular plate, as shown in Fig. 2.15a and 2.15b. Both measurement systems capture this deformation well and are in good agreement with each other. The second harmonic of the nonlinear response, at 321.6Hz is shown in Fig. 2.15c and 2.15d and was found to resemble the third linear mode of a flat rectangular plate. This deformation shape is unexpected since the base excitation that was used should theoretically not be able to directly excite an asymmetric mode such as this. Furthermore, the nonlinear normal modes [70] of a symmetric structure are typically all either purely symmetric or anti-symmetric [69, 71], so this measurement suggests that asymmetry is important to the nonlinear response and this information will be critical when modeling the structure. One should also note that asymmetric motions such as this are frequently observed in initially curved structures so the initial curvature of the plate should be modeled. Again, both measurement systems are able to capture this slightly more complicated mode shape.

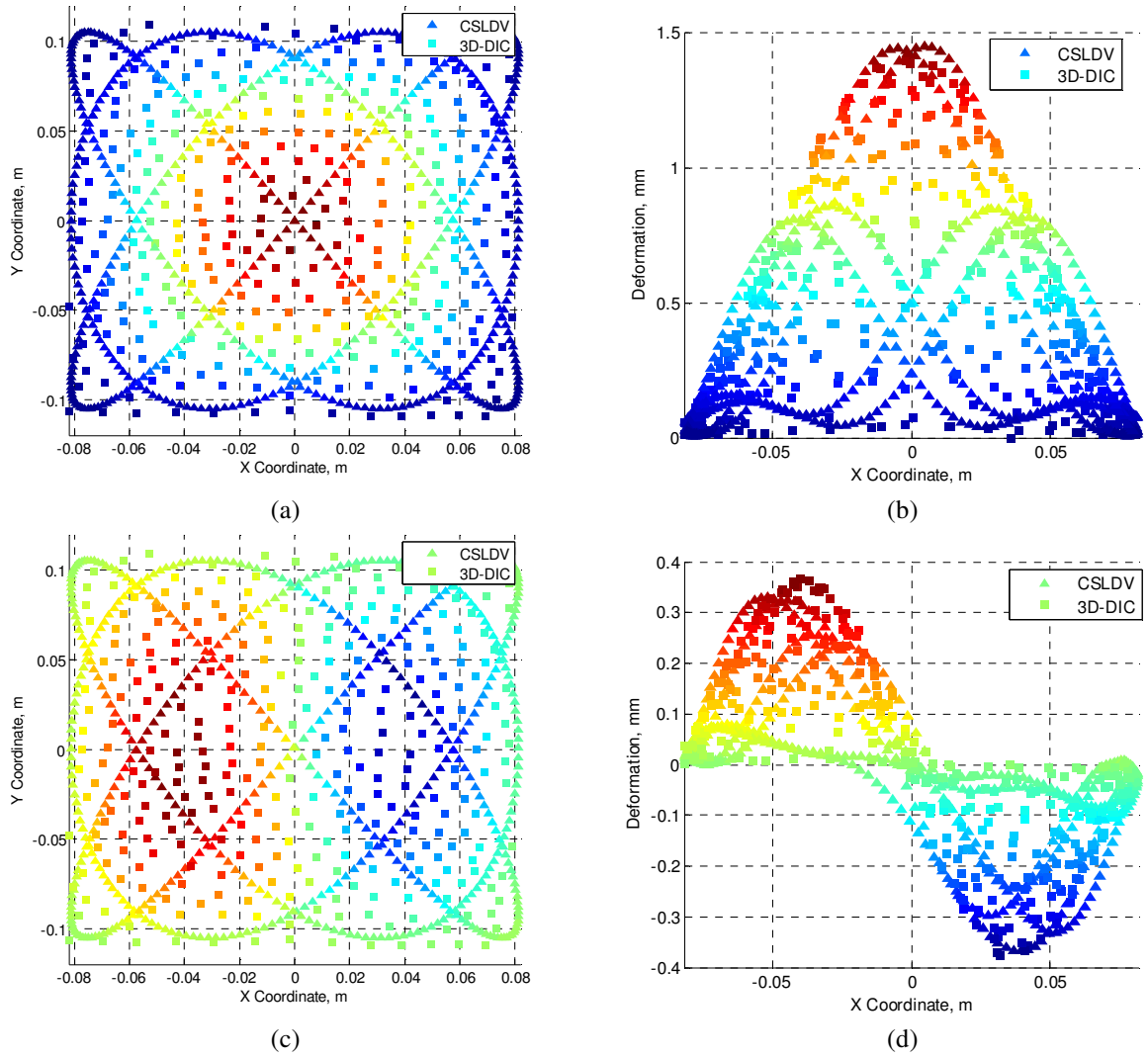

Figure 2.15: Deformation shape of CSLDV and 3D-DIC: a) & b) 1st harmonic, c) & d) 2nd harmonic

The third harmonic, at 482.4Hz, was found to resemble a rotated version of the 5th linear mode of a flat rectangular plate as seen in Fig. 2.16. This type of response is again unexpected as the characteristic shape is asymmetric in the y-coordinate. Again, both measurement systems capture the deformation shape well confirming the validity of this unexpected deformation shape. The fourth and the fifth harmonics showed similar results. The next harmonic examined is the sixth harmonic. Interestingly, the sixth harmonic's deformation shape, at 964.8Hz, resembles the 21st mode of the FE model. Here, the deformation shape is far more complicated, calling into

question the accuracy of a CSLDV shape based on only 39 Fourier terms. The shape does not agree with itself at several of the points where the lines of the Lissajous figure cross. Additional terms could easily be added when post processing the measurement, but the sideband harmonics greater than 39 at the sixth harmonic do not stand out from the noise sufficiently to warrant adding additional terms. The accuracy of the deformation shape with 3D-DIC is also called into question since the deformation at this frequency is small, but the 3D-DIC measurement provides significantly better spatial resolution and that is helpful in understanding the shape.

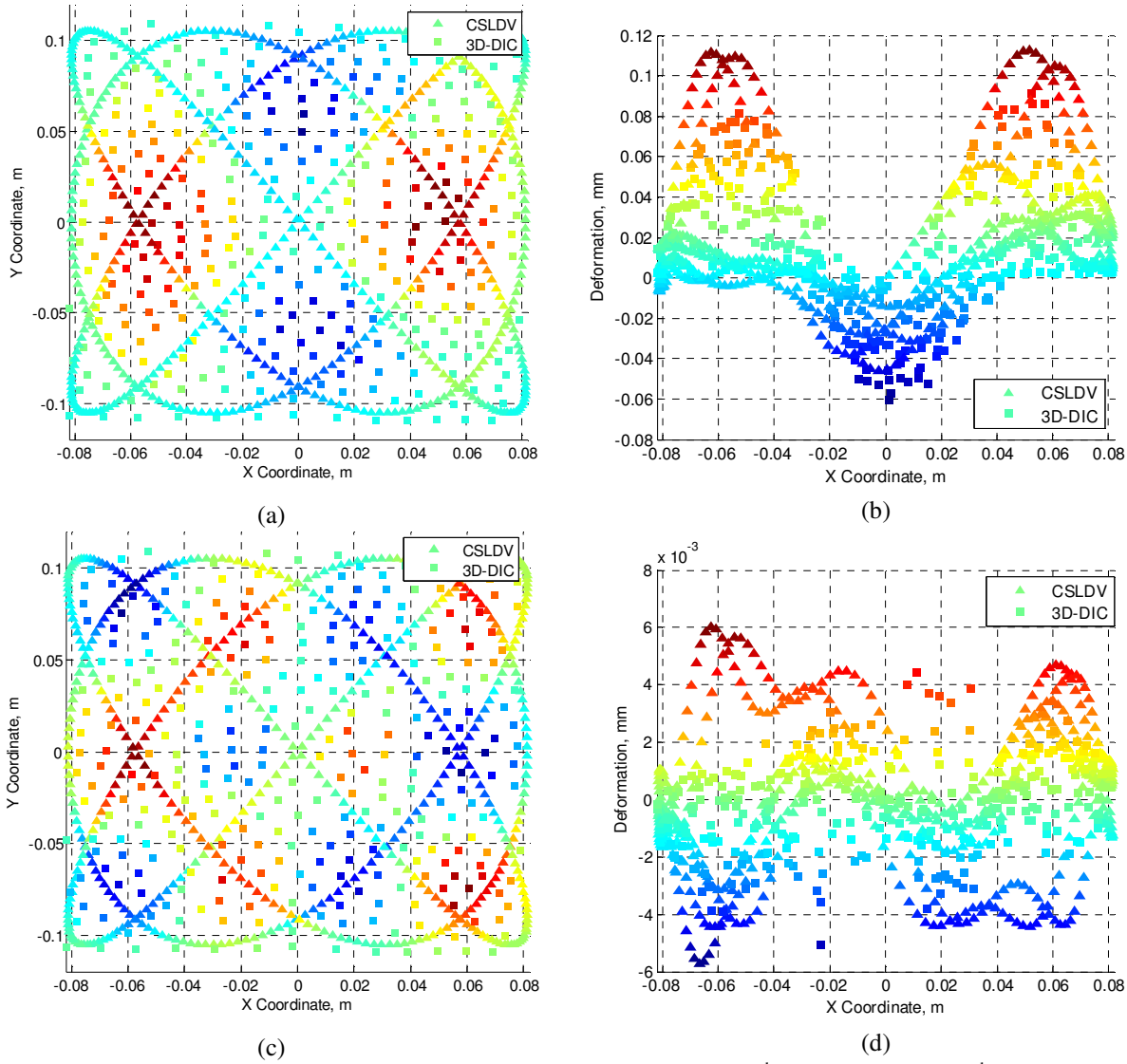

Figure 2.16: Deformation shape of CSLDV and 3D-DIC: a) & b) 3rd harmonic, c) & d) 6th harmonic

2.7 *Summary*

The mode shapes and natural frequencies of a clamped-clamped flat steel beam and a fully clamped rectangular aluminum plate were identified using CSLDV and high speed 3D-DIC. CSLDV was able to measure 1708 points across the surface of the beam and 10240 points across the surface of the plate. However, the information in the measurement is not governed by the number of points used to define the shape but by the number of Fourier coefficients that can be identified to describe the time-varying shape. In fact, decreasing the sample rate, and hence the number of sampled points, has sometimes been found to increase the resolution of the measurement [72]. The number of harmonics is especially important when a more complex 2-D measurement grid is used. Hence, the main disadvantage of CSLDV is that the harmonics describing the shapes are measured rather than the shapes at individual points, and so there may be uncertainty as to whether a feature in the measured deformation is really meaningful.

On the other hand, CSLDV offers a few benefits over high-speed 3D-DIC: CSLDV can measure at large stand off distances, maintains accuracy over larger test specimens, and current LDVs clearly have much higher measurement resolution than DIC, down to tens of nano-meter/s velocities or pico-meter displacements. Some of that resolution can be lost to speckle noise when scanning the laser, and this was observed in the measurement of higher modes for the plate in this study, but even then CSLDV was shown to be more accurate than DIC when capturing the small amplitude linear vibration of the beam and plate. For the (small-amplitude) higher harmonics of the nonlinear response the results were mixed; while CSLDV did have a lower noise floor the number of harmonics required to describe the motion increased significantly and in some cases accurate shapes still could not be measured. Finally, one should note that the

quality of the CSLDV measurement depends on the type of laser, the surface quality, scanning frequency and other parameters so while we expect these trends to hold, the relative performance may be different for other structures.

High speed 3D-DIC was computed with 82 points for the beam and 300 points for the plate; however, a denser measurement grid could have been obtained if needed since the images were stored and post processed to obtain displacements. For the given field of view and geometry, 2500 points can be computed in a 2D grid across the surface of the beam and the measurement resolution is independent of measurement duration or excitation type. (In CSLDV, the spatial information is captured in empty regions between the excitation frequencies lines in the spectrum, and hence one must consider the input type, scan frequency, speckle noise, and the properties of the system to successfully capture measurements.)

The spatial resolution of the acquired mode shape measured with high speed 3D-DIC is dependent on the stand off distance and the camera resolution; therefore, if more accurate measurements are needed, the camera setup needs to be moved closer to the test specimen, or a higher resolution camera is needed. Additionally, since high frequencies correspond to smaller displacements, high-speed 3D-DIC loses ability to measure mode shapes at higher frequencies. One benefit high-speed 3D-DIC has over CSLDV is the ability to provide a 2D grid of measurement points equally spaced across the specimen surface. CSLDV provided measurements over a less optimal grid of points. Furthermore, 3D-DIC measures the three dimensional deformations providing near full-field measurements in all deformation axes. Indeed, with 3D-DIC one can capture the in-plane motions of the surface even more accurately than the out-of-plane motions, whereas CSLDV can only capture the motion along the axis of the

incident laser beam. While the in-plane motions were still too small for 3D-DIC to resolve for the flat structures investigated here, this feature could prove valuable for curved structures.

Both techniques can provide dense measurements along surfaces, as long as each technique can "see" the surface. To provide accurate measurements, both techniques require surface preparation, unless the material used for the test piece fulfills specific requirements (e.g. a random pattern for 3D-DIC and a sufficiently reflective pattern for CSLDV). For DIC, this surface preparation is especially important when response levels are small, or in a structure's linear range. For CSLDV, surface preparation becomes more important when the vibration amplitude becomes small relative to speckle noise, and also as the laser standoff distance (or field of view) increases.

Finally, this study has illustrated that when full-field velocities or displacements are measured (i.e. as opposed to the usual case where the motion is only captured at a few points), inconsistencies in the dynamic behavior of the structure under test can be identified and provide insight to modeling and predicting dynamic behavior. Here, the CSLDV and DIC shapes revealed asymmetry in the 2nd and 3rd bending mode shapes of the beam and a skew in mode 1 of the bending mode shape of the plate, which was probably due to (un-modeled) asymmetry in the boundary conditions or initial geometry of the plate since it is thin. If a traditional test were performed with only a few measurement points, one would not be likely to detect this, nor would they have sufficient information to update the model to account for it.

3 Experimental Identification of Nonlinear Normal Modes

This chapter was taken from a draft of a journal paper that will soon be submitted, and as a result the first few paragraphs repeat some of the theory that was reviewed in the introduction.

3.1 *Introduction*

Over the past several decades a suite of testing and modeling techniques has been developed to quantify the dynamic motion of a structure using modal properties (eg. resonant frequencies, mode shapes, and damping ratios) [5, 73, 74]. The measured or calculated modal properties are typically used to quantify the inertial (mass), elastic (stiffness), and dissipation (damping) characteristics of a structure. Modal properties provide the benefit of describing global dynamics of a structure with a small number of physical degrees of freedom (DOF) due to several attributes inherent to their determination (eg. orthogonality, invariance, and superposition). *Linear Normal Modes* (LNMs) are built on the assumption of linear force-displacement relationships. The classical, undamped LNMs that are our focus here are a special case of *Complex Modes*, and are only valid when the structure exhibits proportional damping or when any coupling of the classical modes due to damping is negligible [75, 76]. The derivation and further description of LNMs can be found in many engineering dynamics or vibrations textbooks [76-79]. When a structure exhibits the nonlinear force-displacement relationships that are typical under large amplitude loading conditions, the concepts behind LNMs break down, the LNMs (e.g. those that could be defined for small deformations about some reference state) become coupled and the resonance frequency shows a strong dependence on amplitude. Therefore, testing and analysis techniques created around a structure's LNMs cannot be directly

used to address nonlinear behavior. For this work, there is a need to distinguish modal coupling due to nonlinear stiffness relationships from modal coupling due to non-proportional damping; the primary focus of this work is on the modal coupling that comes about due to the nonlinear stiffness relationships.

The concept of a mode provides powerful insight into the dynamics of a linear structure, and as a result many researchers have sought to extend this concept to nonlinear systems. Rosenberg [11] defined a nonlinear extension of LNMs which he called *Nonlinear Normal Modes* (NNMs), and which were defined, in essence, as *synchronous oscillations* of the conservative nonlinear equations of motion. Since certain periodic solutions of the undamped equations of motion can be non-synchronous, this definition was later extended by Vakakis and Kerschen to include these by defining an NNM as a *not necessarily synchronous periodic oscillations* of the conservative nonlinear equations of motion [13, 80]. Some NNMs described using this definition are rooted in a structure's LNMs at low response amplitudes, but NNMs also exhibit jumps, bifurcations, internal resonances, modal interactions and sub- and super-harmonic responses which have no counterpart in linear systems [13]. The primary focus of previous work examining NNMs has been on analytical or numerical investigations of low-order lumped-mass systems [11, 13, 50, 52, 53, 81-83], but recent work has sought to extend the numerical calculation of NNMs to higher-order finite element models (FEMs) [84, 85]. Additionally, simulated [21] and physical [16, 47] experimental studies have probed the possible extension of experimental modal analysis (EMA) techniques that use forced responses of a structure to experimentally isolate NNMs. This work explores the effectiveness of these techniques and presents several concepts that can help in isolating the modes of a complex structure.

In EMA, the idea of identifying nonlinearity in the measurement of a structural response is well understood since most techniques break down in the presence of nonlinear behavior [46]. EMA methodologies have therefore been developed to average out observed nonlinearities, avoid nonlinear behavior, or to fit a linear model that approximates the nonlinear behavior of the structure at a specific response amplitude. It must be noted that as experimental technologies have improved accuracy, a much higher incidence of nonlinearity has been observed than in previous years bringing the shortcomings of these linear EMA methodologies to light more frequently [86]. EMA methodologies can be broadly split into two areas classified by the number of LNMs measured during a test. Phase Resonance Methods (PRMs) excite one LNM at a time by tuning the input force so that the measured response is the LNM of interest. Phase Separation Methods (PSMs) excite multiple LNMs at a time with broadband excitation so that the LNMs can be isolated from the measured response by using modal parameter estimation techniques. There are certainly other classifications of modal analysis techniques that can provide a more complete description of the concepts of EMA, but this classification is adequate for the discussion that follows.

The most popular and easily implemented methods available today for EMA are PSMs, where several or all LNMs of interest are excited simultaneously with the use of broadband random, transient, or swept/stepped sine forcing. The modes of vibration are then isolated in these measurements through the use of modal parameter estimation techniques. A good reference for this type of testing and analysis can be found in [5, 73]. In the presence of nonlinearity, PSMs break down in the parameter estimation step since the response no longer has the mathematical form expected for a linear system. The extension of the parameter identification step in PSMs to nonlinear regimes has seen much attention [18, 46]. This is by no

means a complete list of references as no general analysis method is available that can be applied to all nonlinear systems in all instances due to their highly individualistic nature and variation of functional forms. As these methods are applied to higher order systems the number of unknown terms needed in the identification process further complicates their implementation. Therefore, existing phase separation methods have not been regularly applied to industrial practice except, perhaps, for low order systems.

In contrast to PSMs, PRMs focus on a single mode of vibration using a multi-point mono-harmonic forcing vector, and are less popular in linear EMA because they can be time-consuming. However, PRMs are still used in the aerospace industry for ground vibration testing [87, 88] where high levels of accuracy are needed (especially in the measured damping) and modes may be closely spaced or coupled by damping. With PRMs, a normal mode of vibration is isolated in a test when all degrees of freedom displace synchronously with a phase lag of 90 degrees from the input force. For linear systems, several methods have been developed to identify the distribution of the input force needed to fulfill this phase lag criterion [89-92]. PRMs have begun to be extended to the measurement of NNMs through the implementation of different methods of force appropriation. For instance, a force appropriation of nonlinear systems (FANS) method using a multi-point multi-harmonic force vector has been implemented to isolate a single LNM in nonlinear response regimes. This permits the nonlinear characteristics of the isolated mode to be calculated without modal coupling terms. Peeters et al [16, 21] showed that a multi-point multi-harmonic sine wave could isolate a single NNM. It was then demonstrated that a single-point single harmonic force could be used to isolate a response in the neighborhood of a single NNM with good accuracy [16, 47]. In these investigations, once phase lag quadrature was

met, the input force was turned off and the response allowed to decay tracing the backbone of the NNM.

This investigation focuses on measuring the first and third linear normal mode of a flat clamped-clamped beam and its nonlinear continuation at higher response energies. Modal interactions from internal resonances have also been detected and isolated to the level permitted with the experimental setup. To the best of the author's knowledge, this is the first work to experimentally isolate an internal resonance. The next section provides some background information regarding NNMs, presents some new metrics that can be helpful in assessing whether an NNM has been isolated, and uses a simulation based on a finite element model to simulate the experiments that will be performed. Then, the force appropriation techniques are used to experimentally isolate an NNM of the structure.

3.2 *Linear Normal Modes*

3.2.1 Introduction

Linear Normal Modes (LMNs) have become fundamental to the understanding of linear dynamics and are rooted in the conservative free vibration equations of motion (EOM):

$$\mathbf{M}\ddot{\mathbf{x}}(t) + \mathbf{K}\mathbf{x}(t) = 0 \tag{3.1}$$

For an n degree of freedom (DOF) system, $\mathbf{M}$ is the n x n mass matrix, $\mathbf{K}$ is the n x n stiffness matrix, $\mathbf{x}(t)$ is an n x 1 vector of the displacement of the system, and $\ddot{\mathbf{x}}(t)$ is an n x 1 vector of the acceleration of the system. Using the method of undetermined coefficients, the acceleration and displacement of the system can be represented in the exponential form:

$$\ddot{\mathbf{x}}(t) = \mathrm{Re}\left[-\omega^2 \mathbf{X} e^{i\omega t}\right], \mathbf{x}(t) = \mathrm{Re}\left[\mathbf{X} e^{i\omega t}\right] \tag{3.2}$$

Where **X** is a vector of real variables and ω is the excitation frequency. By substituting Eqn. 3.2 into Eqn. 3.2 and rearranging, the EOM can be recast as an eigenvalue/vector problem:

$$\left(\mathbf{K} - \omega^2\mathbf{M}\right)\mathbf{X} = 0 \tag{3.3}$$

The eigenvalues correspond to a structure's LNM frequencies and the eigenvectors correspond to a structure's LNM shapes. For example, Fig. 3.1 shows the first seven LNM shapes of the flat beam used in this investigation.

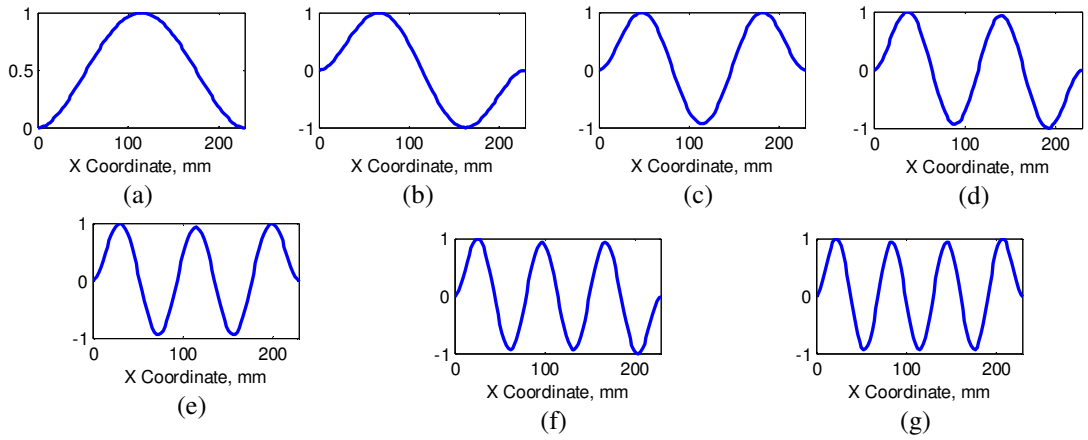

Figure 3.1: The first seven numerically calculated mode shapes of the flat beam used in this investigation.

3.2.2 Measuring Linear Normal Modes with Force Appropriation

As mentioned previously, phase resonance testing is a method whereby a harmonic force is applied to the structure and then tuned through force appropriation until the mode has been isolated. Tuning methods can be split be split into iterative and direct methods [92, 93], but all methods find roots in the characteristic phase lag theory [90].

Beginning with an *N* degree of freedom (DOF) linear system, the equation of motion can be represented by:

$$\mathbf{M}\ddot{\mathbf{x}}(t) + \mathbf{K}\mathbf{x}(t) + \mathbf{f}_\mathbf{d}(\mathbf{x}, \dot{\mathbf{x}}) = \mathbf{f}_\mathbf{in}(t) \tag{3.4}$$

Where $\mathbf{M}$ is the mass matrix, $\mathbf{K}$ is the stiffness matrix, $\mathbf{f_d}$ is the vector of damping forces that depend on the response of the structure, $\mathbf{f_{in}}(t)$ is the input force vector and $\ddot{\mathbf{x}}(t)$, $\dot{\mathbf{x}}(t)$, and $\mathbf{x}(t)$ describe the structure's response. Using the method of undetermined coefficients, the structural response to a harmonic excitation is also assumed to be harmonic. Therefore, it can be assumed that the response and input force shown in Eqn. 3.4, take the forms:

$$\ddot{\mathbf{x}}(t) = \mathrm{Re}\left[-\omega^2 \mathbf{X} e^{(i\omega t-\theta)}\right]; \qquad \mathbf{x}(t) = \mathrm{Re}\left[\mathbf{X} e^{(i\omega t-\theta)}\right]; \qquad \mathbf{f_{in}}(t) = \mathrm{Re}\left[\mathbf{F_{in}} e^{(i\omega t)}\right] \tag{3.5}$$

Where $\mathbf{X}$ and $\mathbf{F_{in}}$ and are vectors of real force and response amplitudes, respectively, variables, ω is the excitation frequency, and θ is the phase lag of the response to the force (all response coordinates also have the same phase lag). There are several forms $\mathbf{f_d}$ can take depending on the dissipation characteristics expected in the structure investigated (e.g. a beam [94]). Two common forms of damping are viscous and structural, which have the following form:

$$\mathbf{f_d} = \mathrm{Re}\left[i\omega \mathbf{C} \mathbf{X} e^{i(\omega t-\theta)} + i\mathbf{D}\mathbf{X} e^{i(\omega t-\theta)}\right] \tag{3.6}$$

Where $i\omega\mathbf{C}$ is related to viscous damping and $i\mathbf{D}$ is related to structural damping, and both are 90 degrees out of phase from the response do the i term in each expression. As a results, both are proportional to a structure's velocity. If only one type of damping is assumed, $\mathbf{C}$ or $\mathbf{D}$ could be set to zero and the general form of damping, $\mathbf{f_d}$, would only contain the remaining damping characteristics. Using the definitions established in Eqns. 3.5 and 3.6, Eqn. 3.4 can be separated into imaginary and real parts with the phase in the complex exponential separated into sine and cosine terms.

$$\left[\left(\mathbf{K} - \omega^2 \mathbf{M}\right)\sin\theta - \mathbf{F_d}\cos\theta\right]\mathbf{X} = 0 \tag{3.7}$$

$$\left[\left(\mathbf{K}-\omega^2\mathbf{M}\right)\cos\theta+\mathbf{F_d}\sin\theta\right]\mathbf{X}=\mathbf{F_{in}} \tag{3.8}$$

As discussed by de Veubeke [90], when the response has a delay of 90 degrees with the input force vector, Eqn. 3.7 only contains the relationship between the stiffness and mass of the structure and Eqn. 3.8 only contains the effect from damping, which is balanced by the input force vector. For this phase criterion, the excitation frequency is at the undamped natural frequency of the structure, $\omega = \omega_n$, and the mono-phased response displacement, **x**, is the *Normal Mode* shape.

Before proceeding to discuss nonlinear systems, it is beneficial to examine force that must be applied to isolate a linear mode using the energy balancing technique [95-97]. If the system is oscillating on a LNM, the power dissipated at any instant is:

$$\mathbf{P}_{diss}=\dot{\mathbf{x}}(t)^{\mathrm{T}}\mathbf{C}\dot{\mathbf{x}}(t) \tag{3.9}$$

and the total energy dissipated for one period of response is:

$$E_{diss/cyc}=\int_0^T\mathbf{P}_{diss}dt=\int_0^T\dot{\mathbf{x}}(t)^{\mathrm{T}}\mathbf{C}\dot{\mathbf{x}}(t)dt \tag{3.10}$$

For an input forcing function $\mathbf{f_{in}}(t)$, the energy the external force inputs into the system is:

$$E_{in/cyc}=\int_0^T\dot{\mathbf{x}}(t)^{\mathrm{T}}\mathbf{f_{in}}(t)dt \tag{3.11}$$

At resonance the energy dissipated by the damping forces must equal the total energy input to the system over the period *T*:

$$E_{diss/cyc}=E_{in/cyc} \tag{3.12}$$

For a structure with well separated modes, a single-point mono-harmonic force is all that is needed to isolate a LNM. Note that such a force is not necessarily a good approximation to the dissipative forces in the structure, but this works because the total energy input per cycle matches the energy dissipated and the energy absorbed by modes other than the mode of interest ends up being very small. In this context, when a single-point, mono-harmonic force is applied at a location n on the structure, with amplitude A, the energy balance criterion in the equation above becomes:

$$\int_0^T \dot{\mathbf{x}}(t)^{\mathrm{T}} \mathbf{C} \dot{\mathbf{x}}(t) dt = A \int_0^T \dot{\mathbf{x}}_n(t)^{\mathrm{T}} e^{i\omega t} dt \tag{3.13}$$

This energy balancing criterion provides a direct link from the computed LNMs to the resonant response of the damped forced system [97]. In an experiment, the tuning of an input force vector to fully appropriate a normal mode, or cancel damping in the structure, is not easily accomplished due to the difficulty in correctly modeling the damping and restrictions based on the experimental setup. An in situ "hard tuning" of the mode is sometimes needed to bring the isolated mode to some specified level of accuracy increasing the required test time to fully appropriate a mode. An overview and comparison of various force appropriation methods can be found in [92].

3.3 *Nonlinear Normal Modes*

3.3.1 Introduction

Similar to the LNMs previously introduced, the NNM definition used in this work is rooted in the conservative nonlinear free vibration EOM:

$$\mathbf{M}\ddot{\mathbf{x}}(t) + \mathbf{K}\mathbf{x}(t) + \mathbf{f}_{\mathbf{nl}}(\mathbf{x}, \mathbf{x} : \mathbf{x}, \mathbf{x}, \mathbf{x}) = 0 \tag{3.14}$$

In addition to the terms in Eqn. 3.1, $\mathbf{f_{nl}}$ is the nonlinear restoring force which is purely a function of displacement (e.g. including only stiffness terms). The nonlinear restoring force can be represented by many functional forms depending on the type of nonlinearity expected (e.g. polynomial stiffness and damping, clearances, impacts, friction, and saturation effects). For the pure geometric nonlinearity expected in the beam investigated here, a polynomial function can be used to describe the nonlinear stiffness. For example, a second order polynomial corresponds to a spring softening effect or decrease in the fundamental frequency of vibration for increasing energy levels, and a third order polynomial corresponds to a spring hardening effect or an increase in fundamental frequency. The clamped-clamped flat beam examined in this work exhibits a nonlinear restoring force that could contain both cubic and quadratic terms as expressed in Eqn. 3.15, both of which come about due to coupling between bending and axial stretching. The EOM becomes more complicated as additional DOF are included, since the polynomials need to include cross terms between all pairs of DOF (e.g. $b_{12}x_1x_2$, see [71, 98] for a more thorough treatment).

$$\mathbf{f}_{\mathbf{nl}}(\mathbf{x}, \mathbf{x} : \mathbf{x}, \mathbf{x}, \mathbf{x}) = \mathbf{a}(x, x) + \mathbf{b}(x, x, x) \tag{3.15}$$

3.3.2 Numerical Example of NNM

Prior to testing, a finite element model (FEM) was created for the flat clamped-clamped beam studied here and in [52]. Several methods have been developed to calculate the NNMs [53, 82] of a finite element models such as this; the numerical results presented here are calculated using the applied modal force numerical continuation technique [52].

For convenience, 'families' of NNMs can be presented in frequency-energy plots (FEPs) based on the fundamental frequency of the response and total energy conserved over a period of the response. Three distinct 'families' of NNMs of the flat beam will be discussed in this chapter. The first 'family' corresponds to the nonlinear continuation of LNM-1, or the backbone of NNM-1 and is shown in Fig. 3.2a in blue. The second 'family' corresponds to a 5:1 harmonic coupling between LNM-1 and LNM3, or an internally resonant NNM-1-3 and is shown in Fig. 3.2a in red. As seen in the FEP presented in Fig. 3.2a, the flat beam exhibits a spring hardening nonlinearity, or an increase in the fundamental frequency of vibration with increased input energy as discussed in [71, 99]. This figure captures a 36% change in the fundamental frequency of vibration in NNM-1, shown in blue, and this large change is observed for relatively small response energies. For reference, a demarcation is added to these plots showing where the maximum displacement amplitude of the beam would be equal to one thickness (e.g. 0.76mm).

Throughout the blue curve (Fig. 3.2b), the LNM-1 dominates the response of the flat beam, although a small broadening of the deformation shape is observed at higher energies due to axial stretching of the beam. Along the red curve (Fig. 3.2b), the deformation shape seems to contain a contribution from LNM-3 at higher energies due to the coupling between NNM-1 and NNM-3. This can be verified through the examination of the deformation of the beam throughout a quarter period of the response (Figs. 3.2c-e) and of the Fourier coefficients of the response (Figs. 3.2f-h). As seen in Figs. 3.2c and 3.2e, which corresponds to Points 1 and 3 marked on the FEP, the LNM-1 dominates the deformation shape and there are minimal contributions from higher harmonics as Figs. 3.2f and 3.2g. The FFT and deformation at Point 2 on the IR branch of NNM-1 are shown in Figs. 3.2d and 3.2g. As the fifth harmonic begins to increase at larger amplitude responses further up the IR branch of NNM-1, the deformation begins to resemble a

combination of mode shapes from LNM-1 and LNM-3, shown in Figs. 3.1a and 3.1c. The LNM-3 shape becomes more pronounced at higher energies on the IR branch eventually dominating the total response of the beam. So, while the LNM-3 shape is not dominant at lower energies (e.g. at Point 2), the interaction between these modes is still visible and can contribute to a larger slope in the deformation of the beam.

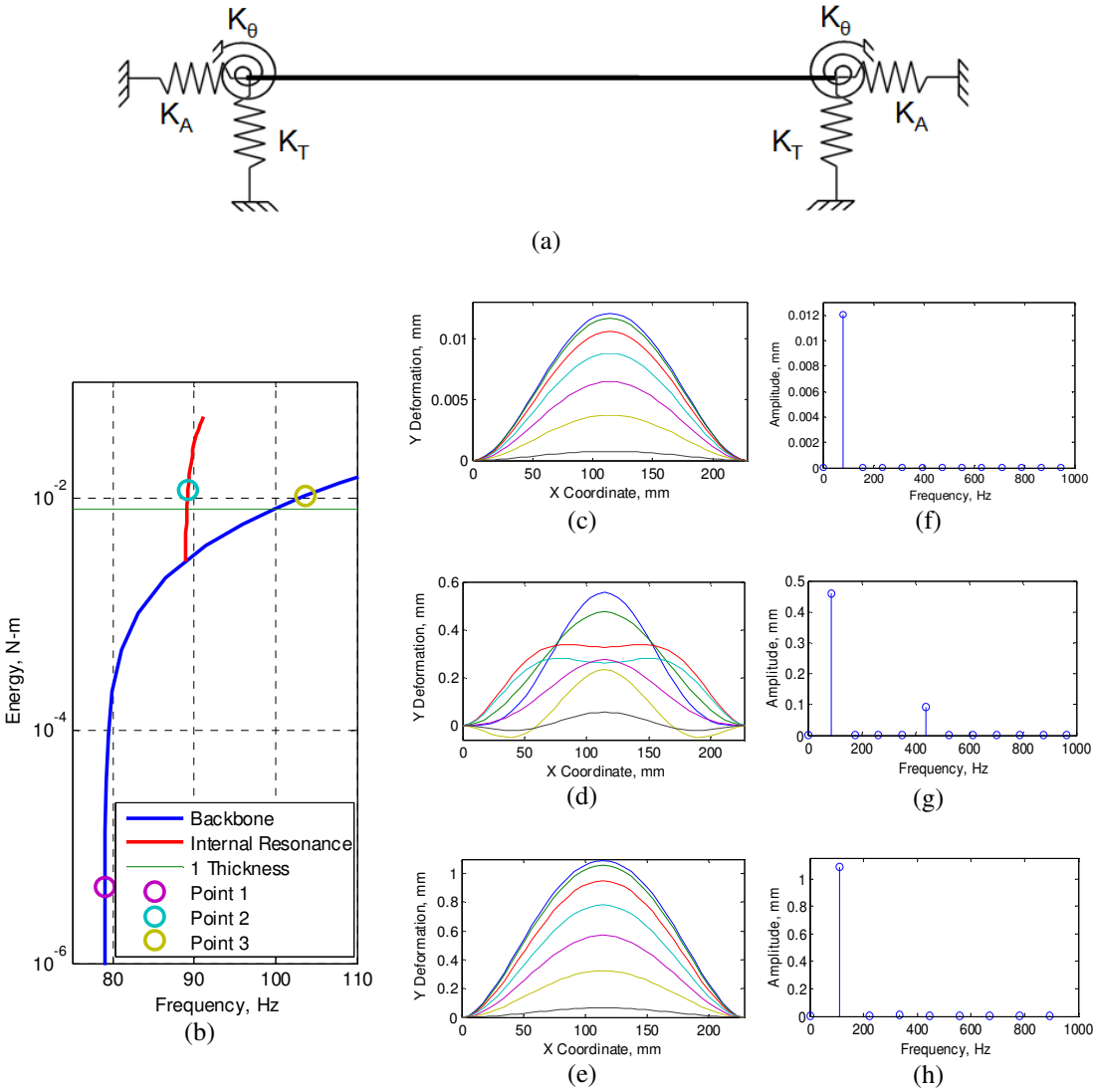

Figure 3.2: Numerical NNM 1 for flat clamped-clamped beam- a) Frequency-energy plot, b-d) Deformation shapes for a quarter period (— 0%, — 4%, — 8%, — 12%, — 16% , — 20%, — 25% of the period) at selected points along the FEP e-g) FFTs of selected points along the FEP

Since the IR branch of NNM-1 shows a coupling with LNM-3 of the beam, it is also of benefit to examine NNM-3, which is shown in Fig. 3.3. Again, a line is added to the FEP in Fig. 3.3a marking a structural deformation corresponding to one beam thickness. It is important to note that over an order of magnitude more energy is required to achieve this deformation level when compared to NNM-1 since the deformation of NNM-3 is more complex and the frequency (hence the stiffness) is higher. Throughout this range, LNM-3 dominates the deformation of the beam at a single frequency while the fundamental frequency increases by 52%. Within this range, no internally resonant branches were detected and NNM-3 is a well behaved nonlinear continuation of LNM-3. This conclusion is verified in Figs. 3.3b-g, where low and high amplitude deformation shapes and FFT's are shown. A similar broadening can be observed in the lobes of the mode shape, due to axial stretching from large amplitude deformations.

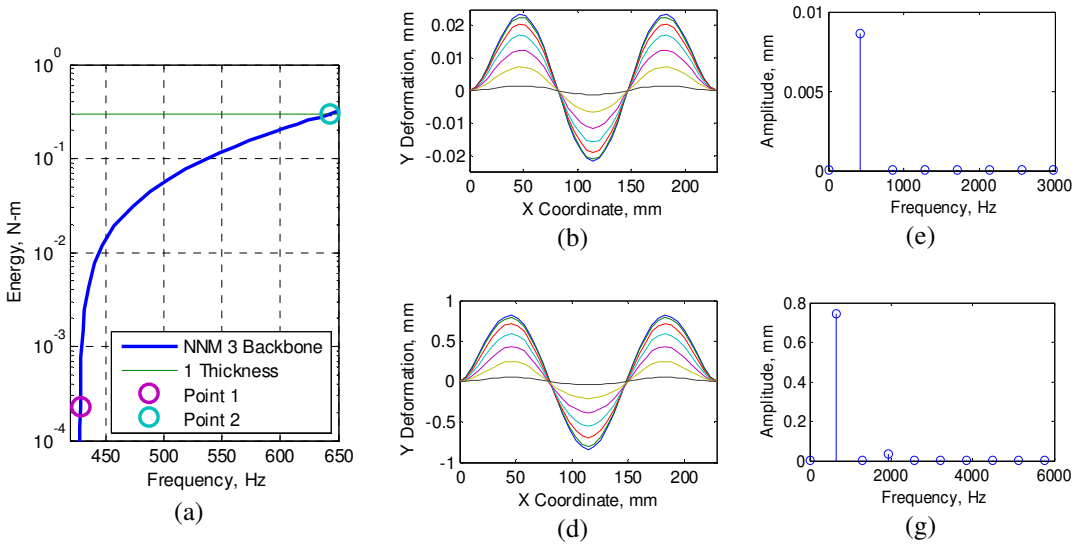

Figure 3.3: Numerical NNM 3 for flat clamped-clamped beam- a) Frequency-energy plot, b-d) Deformation shapes for a quarter period (— 0%, — 4%, — 8%, — 12%, —16% , — 20%, — 25% of the period) at selected points along the FEP e-g) FFTs of selected points along the FEP

3.3.3 Measuring NNMs with Force Appropriation

3.3.3.1 Theoretical Development

The implementation of force appropriation techniques to isolate the periodic solutions related to a NNM requires an extension of the phase lag criterion previously introduced for LNMs. Peeters et al. presented such an extension in [21]. The nonlinear forced response of a structure with a general form of damping can be represented by:

$$\mathbf{M}\ddot{\mathbf{x}}(t) + \mathbf{K}\mathbf{x}(t) + \mathbf{f_d}(\mathbf{x}, \dot{\mathbf{x}}) + \mathbf{f_{nl}}(\mathbf{x}, \mathbf{x} : \mathbf{x}, \mathbf{x}, \mathbf{x}) = \mathbf{f_{in}}(t) \tag{3.16}$$

Where $\mathbf{M}$ is the mass matrix, $\mathbf{K}$ is the stiffness matrix, $\mathbf{f_d}$ is the vector of damping forces of the structure, $\mathbf{f_{nl}}$ is the nonlinear restoring force that is a function of $\mathbf{x}(t)$, and $\mathbf{f_{in}}(t)$ is the external excitation. This equation is similar to the forced response of a linear MDOF system discussed in Eqn. 3.4 with the addition of a nonlinear restoring force. Using the method of harmonic balance [46], it can be shown that $\mathbf{f_{nl}}$ will induce harmonics of the forcing frequency at integer multiples. Therefore it is beneficial to express the structural response as a sum of exponentials:

$$\ddot{\mathbf{x}}(t) = -\sum_{m=1}^{\infty} \mathrm{Re}\left[(m\omega)^2 \mathbf{X}_m e^{i(m\omega t - \theta)}\right]; \mathbf{x}(t) = \sum_{m=1}^{\infty} \mathrm{Re}\left[\mathbf{X}_m e^{i(m\omega t - \theta)}\right] \tag{3.17}$$

It should be noted here that since damping is dependent on the structural response, the damping force should also be expressed as a sum of exponentials:

$$\mathbf{f_d} = \sum_{m=1}^{\infty} \mathrm{Re}\left[i(m\omega\mathbf{C} + \mathbf{D})\mathbf{X} e^{i(m\omega t - \theta)}\right] \tag{3.18}$$

Therefore, an NNM is appropriated when:

$$\mathbf{f_d}(\mathbf{x}, \dot{\mathbf{x}}) = \mathbf{f_{in}}(t) \tag{3.19}$$

Simply stated, the response of a structure is on the NNM when the forcing function exactly cancels the damping forces in the structure for all harmonics. In practice one cannot apply a force that exactly cancels damping, so one wishes to apply a force that approximately isolates an NNM and this can be computed using the energy balancing techniques [96, 97] that was previously discussed. Returning to Eqn. (3.11), the mono-harmonic input force, $\mathbf{f_{in}}(t)$, can be expanded to a multi-harmonic force

$$\mathbf{f_{in}}(t)_j = \begin{cases} \sum_{k=1}^{N} A_k \sin(k\omega t) & j = n \\ 0 & j \neq n \end{cases} \tag{3.20}$$

where n is the point at which the force is applied and $()_j$ denotes the jth element of the vector.

Because the sine function are orthogonal over the fundamental period, T, when this is inserted into the expression for $E_{in/cyc}$, one obtains a sum of terms that give the contribution of each harmonic to $E_{in/cyc}$. Substituting this back into Eqn. (3.13) yields:

$$\int_0^T \dot{\mathbf{x}}(t)^* \mathbf{C}\dot{\mathbf{x}}(t)dt = \sum_{k=1}^{N} A_k \int_0^T \dot{\mathbf{x}}_n(t)^* e^{ik\omega t} dt \tag{3.21}$$

In summary, given the known NNM motion, $\dot{\mathbf{x}}(\mathbf{t})$, and damping matrix, $\mathbf{C}$, the multi-point damping force, $\mathbf{C}\dot{\mathbf{x}}$, can be computed. From this, coefficients, A_k, of a multi-harmonic, single-point force can be determined that would input the same energy per cycle when the structure oscillates in the NNM of interest. This method was used numerically to determine the forced responses needed to isolate a NNM in simulation. In practice the NNM is not known a priori, so we wish to tune the input until an NNM is isolated. We seek a strategy whereby successive

changes in the amplitude and fundamental frequency the input force can be made that isolates an NNM of interest.

For either of the damping models previously described, the damping force lags the displacement of the structure by 90 degrees, or it will be in phase with the structure's velocity. Additionally, measuring the input force and response velocity can often both be measured at the point at which the structure is excited. Returning to Eqn. 3.19, na NNM is appropriated when the input force is equal to the damping forces in the structure, or when the measured input force is exactly 180° out of phase with the measured velocity. It is important to note that although a mathematical model of damping can be assumed, the scaling factor of the damping force is not known a priori, so only the phase information can be used in situ. This force-velocity relationship is easy to monitor in a test and guides the determination of the amplitude and frequency distribution of the force as will be shown both the simulation and experimental results that follow. In order to find a the evolution of an NNM along a branch, this appropriation process can be repeated at subsequent frequency and amplitude levels until the branch of the desired NNM is identified. Since each point along the NNM corresponds to a time invariant periodic response of the structure, the measured time series can be decomposed using a discrete Fourier transform (if the sample increment and period are carefully chosen, or using least squares to solve for the Fourier coefficients, as was done here).

The proposed technique to determine the frequency and amplitude distribution of the force vector strongly depends on the assumption that the dissipative forces are solely dependent on the velocity of the structural response. Therefore it is important to verify the quality of the appropriated response independent of the force applied to the system. For linear structures, the appropriated response is checked using a modal indicator function [92, 100]:

$$\Delta = \frac{\mathrm{Re}\{Z\}^T \mathrm{Re}\{Z\}}{\{Z\}^T \{Z\}} \tag{3.22}$$

Where Z is the complex Fourier coefficient vector of the response. This indicator has been generalized to NNMs, termed the *NNM Appropriation Indicator* (NNMAI) [16]:

$$\Delta_{NNM} = \frac{1}{N_H} \sum_{k=1}^{N_H} \frac{\mathrm{Re}\{Z_k\}^T \mathrm{Re}\{Z_k\}}{\{Z_k\}^T \{Z_k\}} \tag{3.23}$$

Where N_H is the number of harmonics included in the indicator. For a perfectly appropriated mode Δ will give a value of 1 for both indicators.

3.3.3.2 Numerical Example of Stepped Sine Measurement of NNM

This can be demonstrated numerically for the beam previously described by computing the forced response as a NNMs is approached. A Modified Crisfield integration technique is used to find the dynamic response of the beam subjected to a single point input at the center of the beam. For this numerical demonstration, linear modal damping ratios were identified experimentally and applied to the model to create a linear modal damping matrix; the damping is assumed not to change throughout the test. By monitoring the input force and velocity at the center of the beam, one can tell that a mode has been isolated when the area of the input force-velocity goes to zero. This is shown near the three points identified on the numerical NNM as they represent a linear case (Point 1), an internally resonant case (Point 2), and a strongly nonlinear case (Point 3). The results for Point 1 can be seen in Fig. 3.4. In addition to the force/velocity relationship in Fig. 3.4a, MIFs have been calculated for the fundamental frequency of the input and response and are given in the figure's caption. The phases of each harmonic are

provided in Tab. 3.1 and will be discussed subsequently. Each line color corresponds to an increase in input frequency until the MIF is close to 1, while the input force amplitude is held constant. As seen in Fig. 3.4a and 3.4b, with the increase in frequency, the response amplitude increases. Since Point 1 is the near linear case, the higher harmonic content is minimal and the force/velocity relationship appears to be linear once the NNM is isolated. For comparison with Fig. 3.4b, the deformation over a quarter of a cycle is shown in Fig. 3.4c and is dominated by the LNM-1 shape.

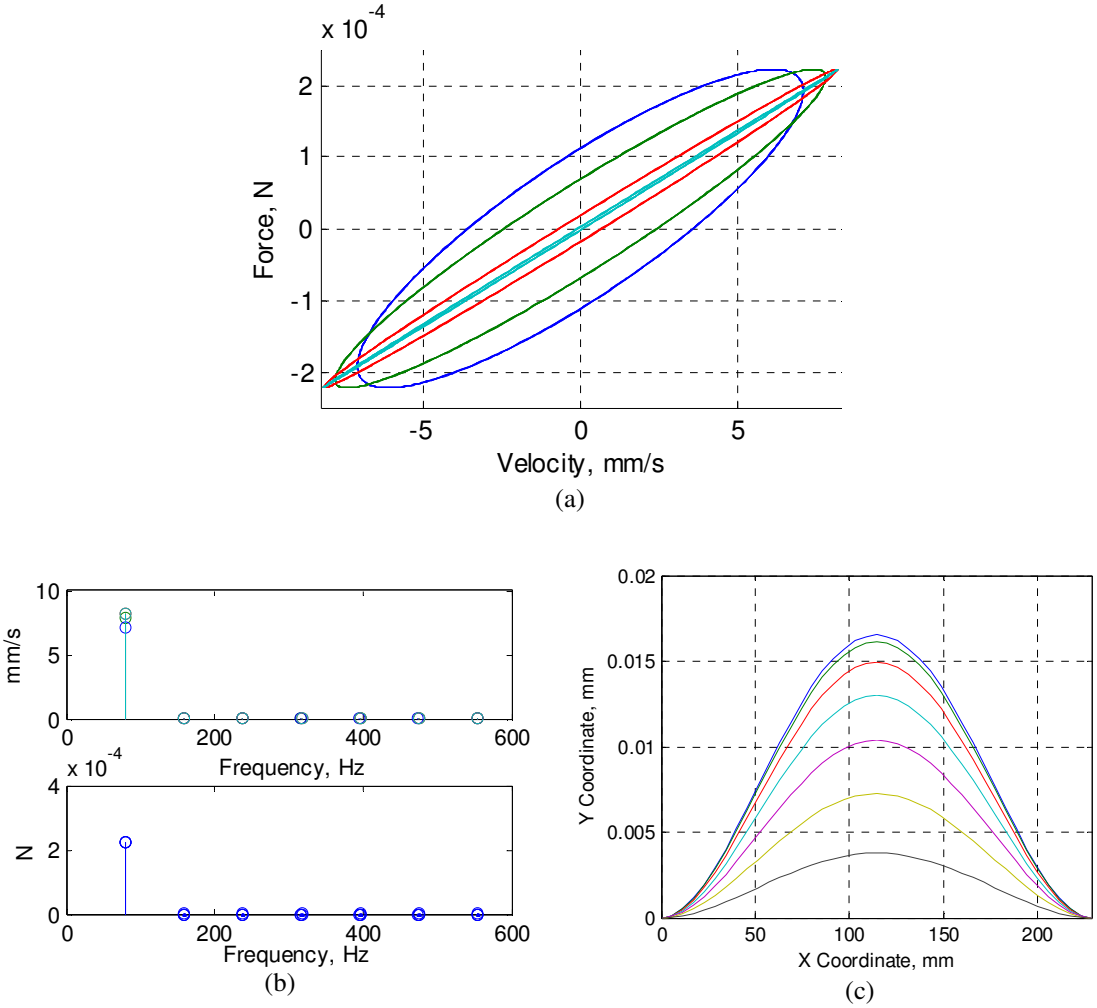

Figure 3.4: Appropriated force for Point 1 on NNM-1. a) Input force versus response velocity and b) Amplitude of force and velocity Fourier coefficients at steps along the forced response of the beam for increasing MIF values (Δ): — 0.7456, — 0.9034, — 0.9931, — 0.9999, c) Deformation shapes for a quarter period (— 0%, — 4%, — 8%, — 12%, —16% , — 20%, — 25% of the period)

Continuing on to Point 2, which is the internal resonance, a strong coupling is observed between LNM-1 and LNM-3 as previously discussed. The steady-state responses for a single-input multi-harmonic forcing amplitude as the frequency is increased are shown in Fig. 3.5. A nonlinear force/velocity relationship is observed in Fig. 3.5a, and once again the area enclosed by the curve decreases as the response approaches the true NNM as evidenced by the MIFs that are given in the figure's caption. The total deformation of the response, shown in Fig. 3.5c, resembles the deformation shape shown in Fig. 3.2c.

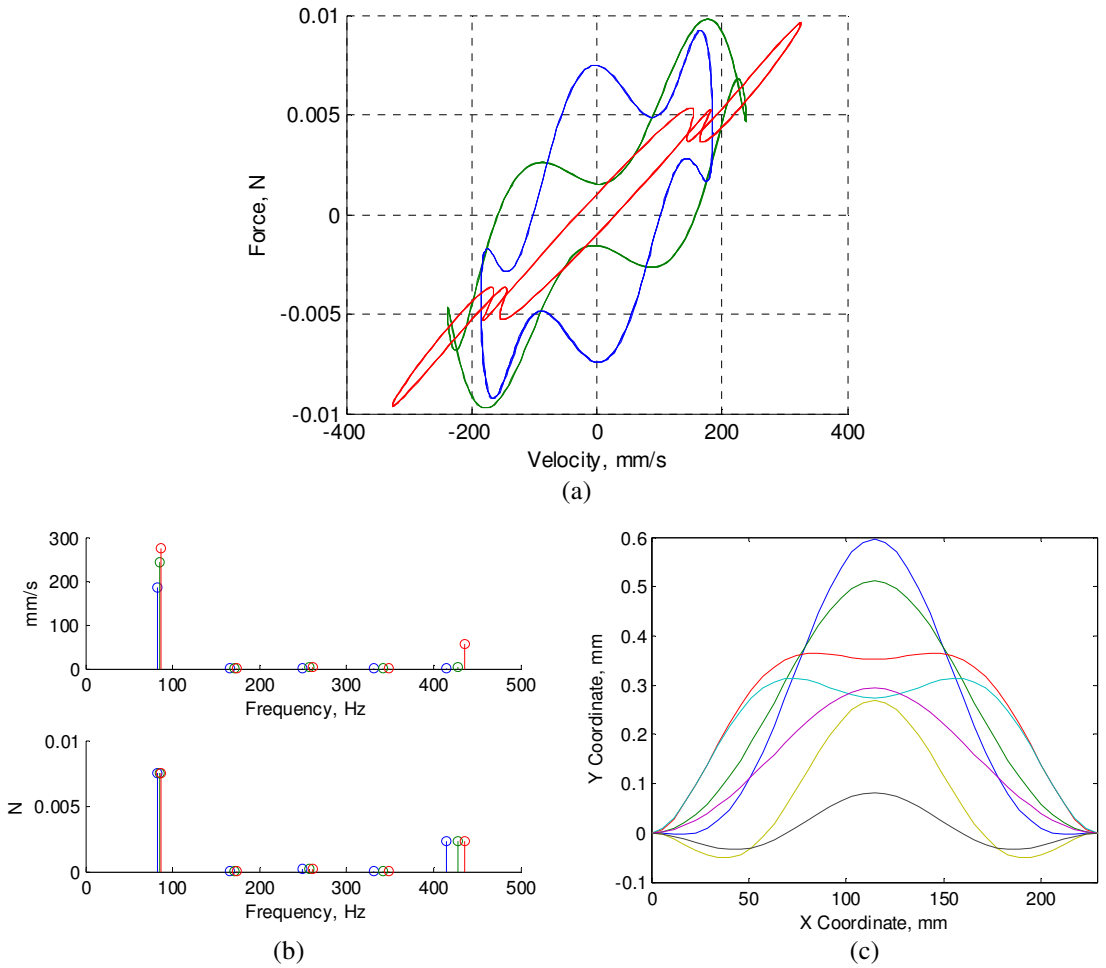

Figure 3.5: Appropriated force for Point 2. a) Input force versus response velocity and b) Amplitude of force and velocity Fourier coefficients at steps along the forced response of the beam at increasing MIF values (Δ): — 0.5153, — 0.7747, — 0.9933, c) Deformation shapes for a half of a period (— 0%, — 4%, — 7%, — 11%, —14% , — 18%, — 25%) of the period

Returning to the main backbone of NNM-1, the results for Point 3 can be seen in Fig. 3.6. The force/velocity relationship in Fig. 3.6a in the appropriated case shows curvature near the ends due to the cubic nonlinearity in the response. The full results of the phase for each harmonic are provided in Tab. 3.1. As seen in Fig. 3.6a and 3.6b, with the increase in frequency, the response amplitude increases. Since Point 3 is on the main backbone of LNM-1, the higher harmonic content is minimal. For comparison with Fig. 3.2d, the deformation over a quarter of a cycle is shown in Fig. 3.6c and is dominated by the LNM-1 shape.

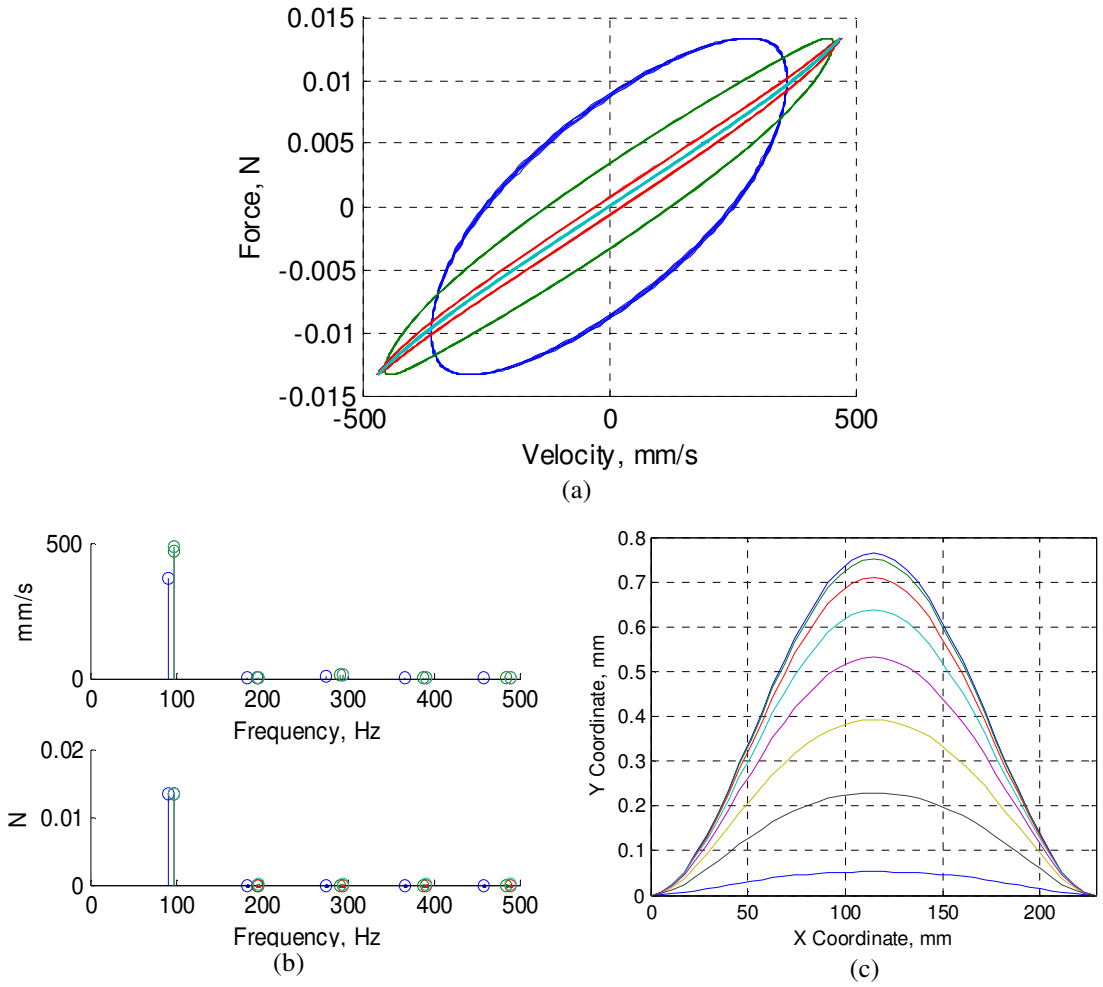

Figure 3.6: Appropriated force for Point 3. a) Force vs. Velocity, b) Amplitude of Fourier coefficients MIF values: — 0.5671, — 0.9358, — 0.9972, — 1.0000. c) Deformation shapes for a half of a period (— 0%, — 4%, — 7%, — 11%, —14% , — 18%, — 25%) of the period

Table 3.1 summarizes the results for these three points. It is interesting to note that quite a good approximation of the NNM is obtained even when the MIF is quite far from 1. For example, at Point 1 the frequency of NNM1 when the MIF is 0.746 is within 0.2 Hz (0.25%) of that when the MIF is 1.000. The phase is found to be even more sensitive; the phase in the fundamental harmonic is off by 30^{o} at this same point and the phases in the higher harmonics are nowhere near the 90^{o} ideal condition. Similar conclusions could be drawn at the other points

Table 3.1: Frequency, MIF, and Phase results for Numerically Appropriated NNMs. The highlighted cells correspond to the harmonics that were injected into the excitation force.

Test Description		Frequency	MIF	Harmonic Number						
				1	2	3	4	5	6	7
Point 1	1	79.0210	0.745	-59.71	150.89	1.00	-33.19	158.33	25.58	-99.79
	2	79.1355	0.903	-71.89	128.68	-35.50	-153.51	34.53	-127.50	18.29
	3	79.2303	0.993	-85.25	99.16	-75.63	134.69	-78.36	-80.17	-1.50
	4	79.2541	0.999	-89.44	83.76	-88.26	3.74	-166.16	-57.75	71.48
Point 2	1	82.9853	0.515	-45.88	36.53	41.40	-174.42	97.75	172.15	166.54
	2	85.6058	0.774	-61.67	46.43	-4.75	49.45	-86.59	109.65	-31.44
	3	87.2655	0.993	-85.42	73.04	-73.85	154.75	-83.42	-96.70	-74.01
Point 3	1	91.6597	0.567	-48.86	61.73	33.23	124.14	-58.16	-36.26	36.01
	2	97.0329	0.935	-75.32	106.81	-45.83	-39.14	164.01	20.62	-166.15
	3	97.8942	0.997	-86.98	94.96	-80.80	-88.95	105.67	-117.66	111.75
	4	97.9379	1.000	-90.24	89.49	-90.58	-91.64	89.41	-92.87	89.01

3.3.3.3 Numerical Example of Free Decay Measurement of NNM

As mentioned previously, the stepped sine approach is time consuming since the NNM must be isolated at each amplitude of interest. For systems exhibiting light damping, the stepped sine approach can be avoided by examining the damped free decay of the system from an isolated high energy NNM as described in [21]. This approach relies on two assumptions about the dynamics of the structure. First, the definition of a NNM must be recast into the damped nonlinear mode as developed by Shaw [101] and Jiang et al [81]. In that description, a NNM can be considered an *invariant* manifold, that describes the evolution of a pair of state variables in

linear modal phase space. (Note that to describe interactions of modes one must retain a pari of coordinates, (e.g. modal displacement and velocity), for each mode involved in the NNM response yet that is not considered in any of the works on the resonant decay method of which the authors are aware). Due to the *invariance* property of these manifolds, a motion that initiates on the defined manifold will remain on the manifold for all time. Only under these conditions can one be assured that the response will not depart from the manifold of interest as the energy decays. Second, the undamped NNM must be viewed as an attractor of the damped free response of the system, so that motions that initiate near the undamped NNM are drawn to it and decay along the manifold. Third, the damping should be light so that the damped manifold is well approximated by the undamped manifold. Under these conditions the free decay of a system initiated on a NNM can be considered an approximation of the undamped NNM. Since the time series measurements of the free decay are time variant, more complex signal processing techniques such as the Wavelet Transform [102] and Hilbert Transform [103] are needed. A recent interesting contribution to this type of analysis can be found here [19].

Returning to the simulation results for the fully appropriated responses at Point 2 and Point 3, the force used to cancel damping within the system is turned off and the response is calculated as the system decays. The Wavelet Transform and the Hilbert Transform can be used to describe this decaying response. Using the building Wavelet toolbox in MATLAB®, a Morlet wavelet is selected as the base family for the wavelet analysis. For the decay corresponding to the Point 2 appropriated NNM, the time series and the wavelet transform are presented in Figs. 3.7a and 3.7b. The Wavelet Transform, shown in Fig. 3.7b, shows two dominant frequencies in the response at 85.91Hz and 430Hz corresponding to a 5:1 harmonic interaction of the response, although the response of the fundamental harmonic is an order of magnitude larger than the fifth

harmonic. For Point 3, the time series and the Wavelet Transform are presented in Figs. 3.7c and 3.7d. Through the Wavelet Decay analysis shown in Fig. 3.7d, two harmonics are initially observed in this response at 110.7Hz and 335.7Hz corresponding to a 3:1 harmonic interaction in the response; however, the fundamental harmonic dominates the response by more than an order of magnitude when compared with the third harmonic. While the MIF can be used to determine when a forced response is on an NNM, a similar metric has not been developed for the free response and so one cannot tell whether these responses have decayed along an NNM. It is therefore helpful to compare the true NNM-1 with the results of these free decay simulations and with the stepped-sine simulations.

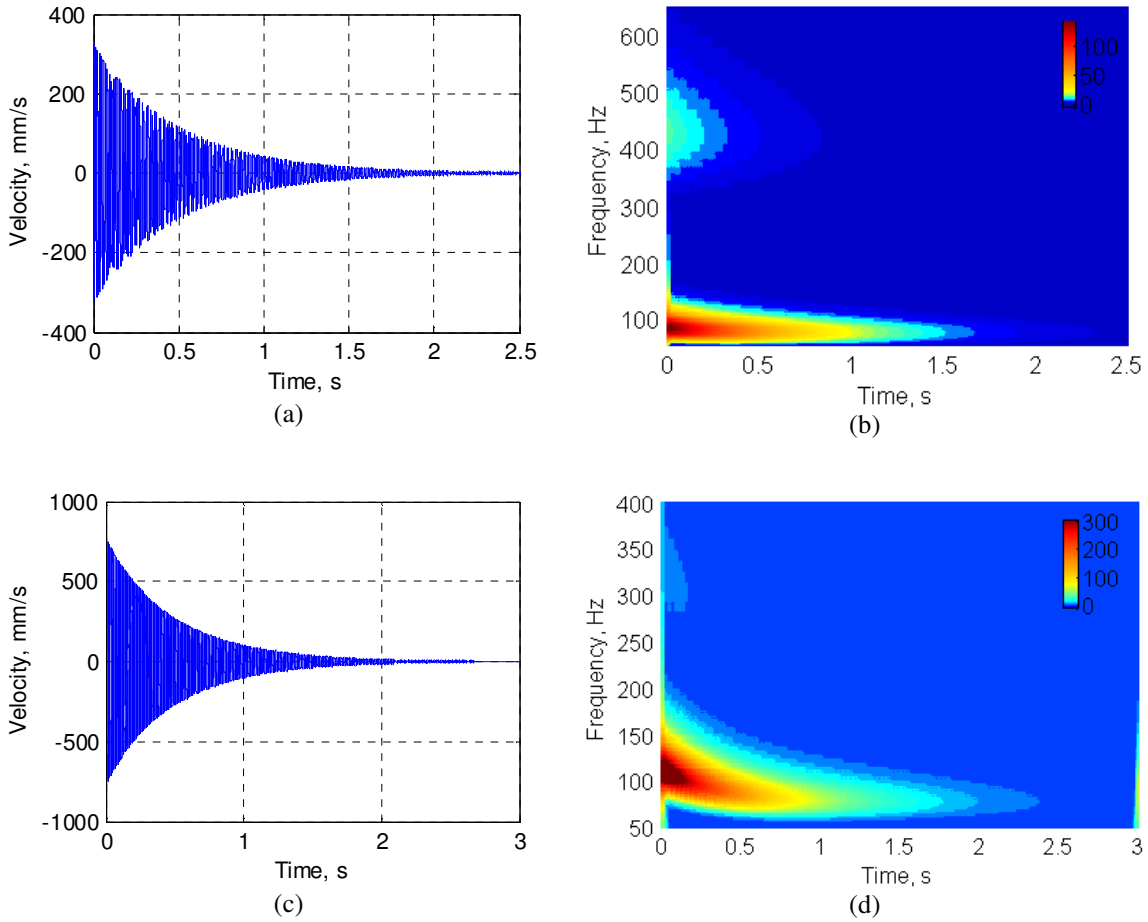

Figure 3.7: Wavelet analysis of free decay of appropriated NNMs. a) Time series and b) Wavelet decay of NNM appropriated at Point 2. c) Time series and d) Wavelet decay of NNM appropriated at Point 3

3.3.3.4 Comparison of NNM Measurement Methods

Figure 3.8 compares the isolated NNM responses for the stepped-sine and free decay experiments. The stepped-sine results were analyzed using Fourier series techniques and the instantaneous amplitude and frequency of the decaying response was determined using the Hilbert Transform. For the NNM-1 backbone, two decays were performed. Each decay was initiated with the highest level of forcing amplitude, but at two different frequencies corresponding to two different MIF values (1.000 and 0.5114) and therefore two levels of accuracy in the appropriated forcing. The decay of the fully appropriated NNM-1 at Point 3 (MIF = 1.000), is shown with a blue line and the decay of the partially appropriated response at Point 3 (MIF = 0.5114), is shown with the green line. Both decays overlay well showing the effectiveness of the free decay in the isolation of NNM-1, even when the force does not perfectly isolate the NNM. The blue and green circles show the starting points of each of these decays. Two additional points were added, shown with cyan and magenta circles, corresponding to NNMs that were isolated by iterating on the stepped sine input until a high MIF value was obtained. This response appears to backbone of NNM-1 through the internal resonance branch presented in Fig. 3.2. The third decay, shown in red, corresponds to the decay of the response off of the IR branch of NNM-1. The starting point of this decay is shown as a red circle. It is interesting to note that this decaying response does not solely decay on the internal resonance branch (at 430Hz) before following the backbone of NNM-1, but instead follows a different path with a dominant frequency closer to the NNM-1 backbone until settling onto LNM-1. This illustrates a limitation to the free decay technique when the NNM exhibits strong modal coupling as additional forcing is potentially need to follow the IR branch of NNM-1.

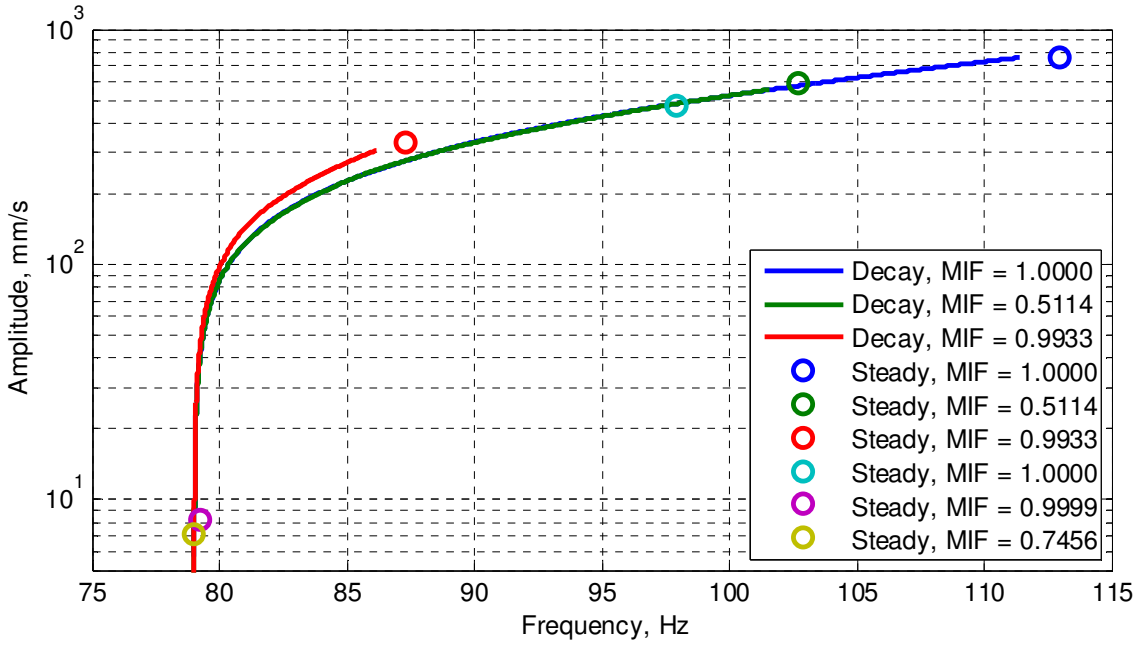

Figure 3.8: Comparison of NNM measurement techniques.

3.4 *Application to Clamped-Clamped Flat Beam with Geometric Nonlinearity*

3.4.1 Flat Beam Description

The structure used for this investigation is a precision-machined feeler gauge made from high-carbon, spring-steel in a clamped-clamped configuration previously studied in [67]. The beam has a nominal effective length of 228mm, a width of 12mm, and a thickness of 0.76mm. It is important to note that all presented dimensions are nominal and subject to variation from clamping and stress variations from machining process to obtain the desired thickness. Prior to clamping, the beam was prepared for three dimensional digital image correlation (3D-DIC) and continuous-scan laser Doppler vibrometry (CSLDV) as discussed in [42] and shown in Fig. 3.9. The clamping force was provided by four 6.35-28 UNF-2B bolts tightened to 9 N-m from left to right. After clamping the beam to the fixture, a single-input single-output modal hammer test was

performed on the beam so linear natural frequencies and damping ratios could be identified as well as a static 3D-DIC measurement so any initial geometry variations could be identified. Additionally, operational modal analysis and CSLDV [63] were used to determine the mode shapes of the beam. Results of the natural frequencies and damping ratios of the first ten modes identified from the modal hammer test are shown in Tab. 3.2, and results of the first seven elastic bending mode shapes are shown in Fig. 3.10. In Fig. 3.10, forward and backward sweeps of the CSLDV setup were used independently to reconstruct the mode shapes, so deviations between the two measurements give an indication of error in the measured shapes. For example, the lower left lobe of the third mode shape shows a small difference between the forward and backward sweep reconstructed shape indicating a deviation in the isolated mode. Since these errors are relatively small, the two shapes are averaged, and the new averaged shape is used to decompose the nonlinear CSLDV measurements as shown in the results section.

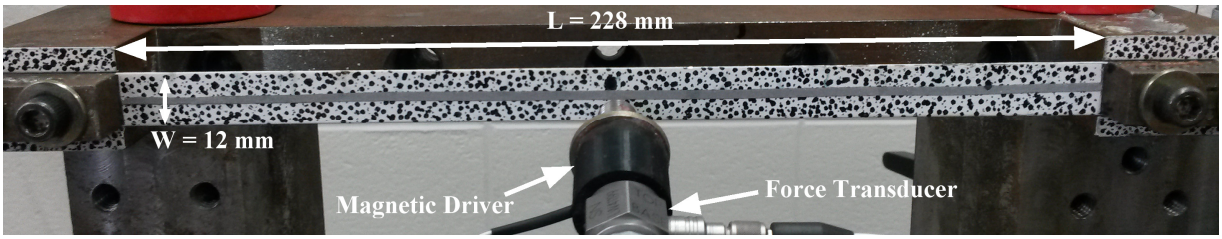

Figure 3.9: Beam Specimen

Table 3.2: Linear (low amplitude) natural frequencies of flat clamped-clamped beam

	Mode 1	Mode 2	Mode 3	Mode 4	Mode 5	Mode 6	Mode 7	Mode 8	Mode 9	Mode 10
f, Hz	45.8	171.6	371.7	638.7	973.7	1376.5	1847.7	2387.2	2586.5	2994.7
$\zeta 1$, %	0.38	0.12	0.09	0.08	0.08	0.07	0.06	0.06	0.04	0.06

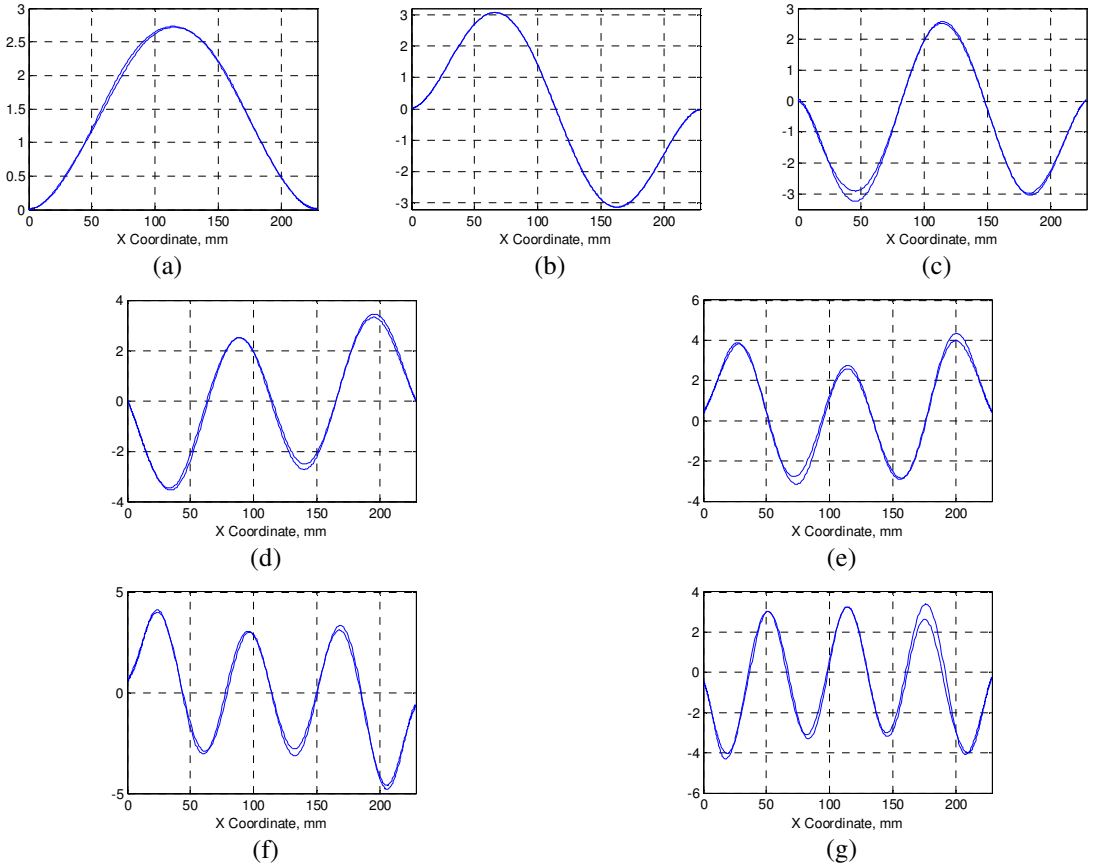

Figure 3.10: The first seven mode shapes of the beam. a-g) Modes 1-7

3.4.2 Experimental Setup

For this experimental setup, there are 3 systems: 1) exciter/controller, 2) Continuous-scan Laser Doppler Vibrometer measurement system, and 3) system for force appropriation:

1) Due to the thin nature of the beam, any application of force due to a contacting exciter would modify the dynamic response considerably. Therefore, excitation of the structure was provided by a non-contacting magnetic driver powered with a Piezo Amplifier. Although not ideal, the input force exerted by the magnetic driver was measured using a PCB force transducer mounted between the magnetic driver setup and a solid base. At lower forcing amplitudes,

complementary results between the input voltage and measured force were found but showed a small phase difference. At higher forcing amplitudes, the magnetic driver setup further contaminated the measured force as discussed in the results section. At low and high forcing amplitudes the response of the beam follows the input voltage building confidence in the use of the voltage signal as the input force level.

2) Full-field dynamic measurements were taken using Continuous-scan laser Doppler vibrometry (CSLDV) and full-static measurements were taken using three dimensional digital image correlation (3D-DIC). Details for both of these measurement techniques can be found [42]. 3D-DIC will be used to determine any initial curvature of the structure and CSLDV will be used to determine the LNMs participating in the nonlinear response.

3) Prior to scanning the single point laser Doppler vibrometer (LDV) was used to measure the response of the beam as it was subjected to a single frequency sinusoid at a specified excitation amplitude. The voltage input to the exciter was measured as well as the input force for the magnetic driver and the base acceleration for the shaker. The velocity response and input voltage signals were measured in real time and displayed in a built LabView program capable of modifying the amplitude and frequency distribution of the external force being input to the beam. Here, the input voltage was used instead of the measured force to limit noise contamination from the measurement sensors. The input frequency and amplitude distribution could then be determined by adjusting the frequency of the fundamental harmonic and amplitudes of the input harmonics until the input voltage and response velocity traced a line (e.g. the area enclosed by the curve was zero). In a post processing step, the phase relationship for all harmonics was examined more precisely.

3.4.3 Flat Beam Experimental Results

3.4.3.1 Effect of Magnetic Driver on the Dynamics of the Beam

As previously mentioned, the magnetic driver used for the experimental setup interacts with the structure and care must be taken so that this does not contaminate the results. For illustration, a schematic of the force transducer, magnetic driver, and beam cross section is shown in Fig. 3.11. The magnetic driver has a permanent magnet embedded in the inductor, so there is a magnetic field produced even when there is no voltage supplied. A low amplitude hammer test was performed on the beam before and after the magnetic driver was placed in front of the beam to find the initial effect the magnetic driver has on the response of the beam. The results of the error between the identified natural frequencies and damping ratios before and after the magnetic driver was placed in front of the beam are presented in Tab. 3.3. It is shown that the magnetic field has a greater effect on the damping of the beam than the natural frequencies for low amplitude vibrations.

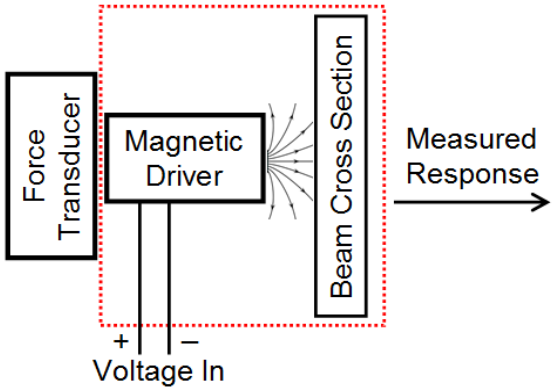

Figure 3.11: Schematic of Magnetic Driver and Beam Interaction

Table 3.3: Percent Error of Identified Natural Frequencies and Damping Ratios when the magnetic driver is near the beam

Percent Error	Mode 1	Mode 2	Mode 3	Mode 4	Mode 5	Mode 6	Mode 7
f	2.07	0.88	0.36	0.26	0.02	0.17	0.12
ξ	-5.45	90.0	-35.0	0.0	-22.2	-6.7	0.0

Since the expected beam deflections are large, any nonlinearity in the driver could potentially contaminate the measured NNMs. To determine whether the voltage signal is representative of the input force, the power input from each harmonic was determined using the reaction force and measured velocity at the excitation point. Figs. 3.12a and 3.12b show the comparison between the measured force, voltage, and velocity of the structure at a low and high amplitude resonance responses. The input voltage closely resembles the response of the beam, but the measured reaction force exhibits a small phase shift for the low amplitude response and completely different characteristics for the large amplitude response.

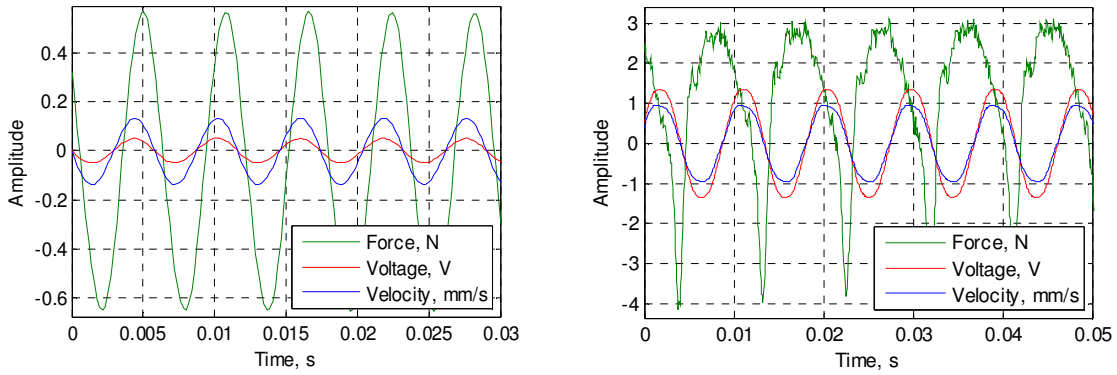

Figure 3.12: Comparison of force, voltage and velocity signals.
a) Low amplitude response. b) High amplitude response.

This is initially concerning as it would appear that the magnetic driver induces a force on the beam that is not well characterized by the input voltage (which was the signal that was used as a surrogate for the force when tuning the input force). However, if the input force does not induce a deformation in the beam, it will not contribute to the energy input to the beam needed to cancel the dissipation due to damping. The energy input:

$$E_{in} = \int_0^T v(t) f_{reaction}(t) dt \tag{3.24}$$

was calculated by multiplying the measured input force and response velocity and then numerically integrating over a period. Several harmonics are present in the measured force, so the energy was further decomposed into the contribution of each harmonic to the energy input. The process was then repeated at each of the three points described previously and the result is shown in Tab. 3.4. For all three points, the first harmonic dominates the power input to the beam. At Point 2, which corresponds to NNM-1-3, the power input for the fifth harmonic appears to have a significant contribution as well. In contrast, the second harmonic, which is responsible for much of the distortion in the measured force in Fig. 3.12b, contributes negligible power and hence its effect will be ignored.

Table 3.4: Power Input to the Beam

	Harmonic 1	Harmonic 2	Harmonic 3	Harmonic 4	Harmonic 5	Harmonic 6	Harmonic 7
Point 1	0.003	0.000	0.000	0.000	0.000	0.000	0.000
Point 2	12.155	0.061	-0.137	0.017	-1.333	0.033	0.206
Point 3	44.266	0.203	0.629	0.199	-0.180	-0.003	-0.003

3.4.3.2 Voltage-Velocity plots and phase lag of harmonics

Following the point specifications described in Fig. 3.2, the appropriated force will be examined at three similar points along the experimentally measured NNMs. The time and Fourier domain descriptions of the force/velocity relationship for Point 1 are shown in Figs. 3.13a and 3.13b. At Point 1, three successive measurements were taken in the determination of the appropriated force where a harmonic was added to the forcing function at each measurement. This is shown in the bottom plot of Fig. 3.13b, where the blue line corresponds to a single harmonic force, the green line is a two harmonic force, and the red line is a three harmonic force. It is interesting to note that although higher harmonic content was added to the input force, the second and third harmonics of the response, shown in the top plot of Fig. 3.13b, are relatively

unchanged. The added harmonic content primarily changes the phase relationship between the voltage and the velocity which can be shown in Fig. 3.13a where the time trace of the voltage and velocity is seen. The values of the phase angle between the input voltage and velocity for Point 1 are shown in Tab. 3.5 where the cells filled in with blue correspond to the harmonics that are included in the force for each test. As expected, each subsequent step of appropriation brings the voltage and response more closely into quadrature. Returning for a moment to Fig. 3.4, where the appropriated force vector is determined numerically with a single-point mono-harmonic force, the force/velocity relationship expected is a line. However, until the phases are examined in Tab. 3.5, one does not know which is a better estimate of the NNM. Tab. 3.5 does reveal that the mode is more closely isolated once the second and third harmonics are injected into the force, but the third has an almost negligible effect.

It is peculiar that a second harmonic should be needed. One possible explanation, is that the voltage is the input to the coupled magnetic-driver-beam system (outlined in red in Fig. 3.11) so perhaps the second harmonic is needed to cancel a nonlinearity due to the magnetic driver.

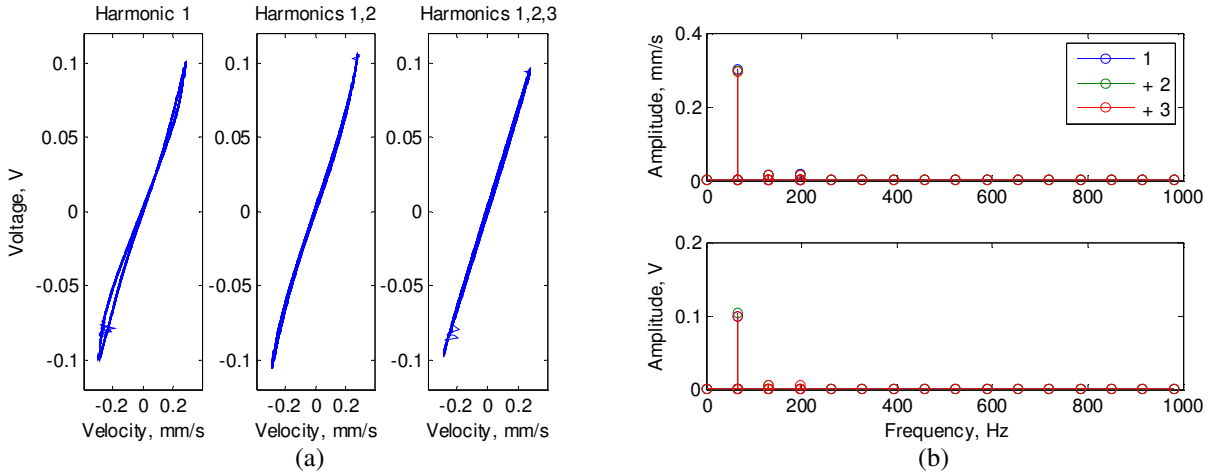

Figure 3.13: Appropriated force for Point 1. a) Voltage vs. Velocity, b) Amplitude of Fourier coefficients

This process is repeated for Points 2 and 3. Again, converging values of the phase are observed between the voltage and velocity as higher harmonics are added to the input voltage. It should be noted that since Point 2 (Fig. 3.14) and Point 3 (Fig. 3.15) correspond to a greater nonlinear behavior of the beam, more harmonic content is needed to cancel the damping observed. In the tests performed, the harmonics were tuned in an effort to minimize the enclosed area in the curve. In the appropriated response for Point 2, Fig. 3.14, the voltage/velocity relationship indicates that as higher harmonics are added, the shape of the voltage/velocity plot changes providing insight to how each added harmonic changes the response. When compared with the numerically calculated force/velocity relationship, Fig. 3.5, the force characteristics that that includes only the first and fifth harmonics best matches the appropriated response indicating the best experimental force distribution. Similarly, the voltage/velocity relationship observed for Point 3 (Fig. 3.15) indicates that the force that includes only the first and third harmonic better matches the numerically determined force/velocity relationship established in Fig. 3.6.

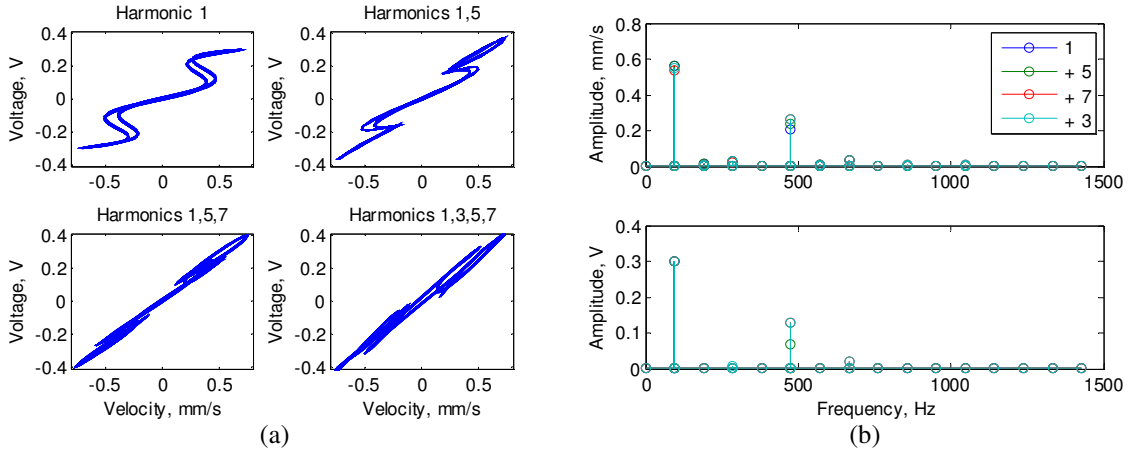

Figure 3.14: Appropriated force for Point 2. a) Voltage vs. Velocity, b) Amplitude of Fourier coefficients

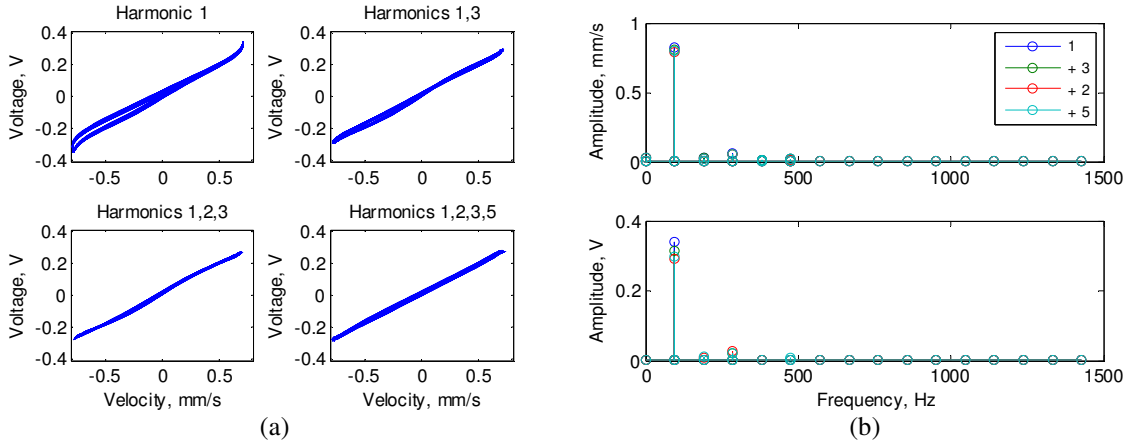

Figure 3.15: Appropriated force for Point 3. a) Voltage vs. Velocity, b) Amplitude of Fourier coefficients

Table 3.5: Phase relationships between the first harmonic of the Input Voltage and all harmonics of the measured response

Test Description		Harmonic Number						
		1	2	3	4	5	6	7
Point 1	1	1.18	-91.87	177.74	88.51	-0.62	102.83	27.42
	2	1.05	-92.37	177.19	83.59	-4.41	88.85	58.86
	3	1.30	-91.86	177.97	86.11	-2.59	92.81	67.82
Point 2	1	1.87	-89.96	-173.23	-113.58	-18.44	-107.99	163.15
	2	1.90	-90.07	-172.63	-110.74	-17.08	-107.89	164.51
	3	3.51	-86.57	-164.18	-108.60	-13.46	-103.35	171.77
	4	2.92	-87.95	-166.86	-108.87	-14.40	-104.66	169.54
Point 3	1	2.14	-90.07	-177.65	94.06	-176.90	-75.11	4.87
	2	0.79	-93.01	178.34	89.44	176.50	-79.48	-4.22
	3	0.63	-93.25	177.73	89.62	175.64	-78.04	-4.46
	4	0.59	-93.49	177.67	89.18	175.40	-78.54	-5.23

Using the calculated phase from the fundamental harmonic of the velocity response, subsequent higher harmonics are shifted so the relative phase is identified. Results of this shifted phase relationship are shown in Tab. 3.6, where again, cells filled in with blue correspond to the harmonics that are included in the force for that test. Here, the harmonics of the velocity do not converge to an in phase value as observed in the relationship between the force and velocity. This can be confirmed by looking at the NNMAI introduced in Eqn. 3.23 and shown in Tab. 3.6.

Three NNMAIs are computed at all harmonics, the odd harmonics, and the even harmonics of the response. The maximum value of each NNMAI at each Point is highlighted in orange where it is observed that the maximum NNMAI for all harmonics occurs when the even harmonics are also better appropriated. However, due to the nonlinearity seen in the beam, the odd harmonics are expected to dominate the nonlinear response, which is observed for Point 2 in Fig. 3.14. For Point 1 and Point 3, the higher harmonics occur at least an order of magnitude lower than the fundamental harmonic. The lower importance of these harmonics provides some insight as to the location of the maximum NNMAI value for the odd harmonics. In an ad hoc manner, if only the harmonics that are an order of magnitude or greater are included, Point 1 would consist of the first harmonic, Point 2 would consist of the first and fifth harmonic, and Point 3 would consist of the first and third harmonic. If this had been used as a rule when selecting the forcing harmonics, the responses obtained would have the largest NNMAI values, computed over the odd harmonics of all of the cases considered.

Table 3.6: Phase relationships between the fundamental and higher harmonics of the response

Test Description		Harmonic Number							NNMAI		
		1	2	3	4	5	6	7	All	Odd	Even
Point 1	1	0.00	-94.23	174.21	83.79	-6.52	95.75	19.16	0.5398	0.9643	0.0091
	2	0.00	-94.47	174.04	79.40	-9.65	82.56	51.53	0.5406	0.8337	0.1743
	3	0.00	-94.45	174.09	80.93	-9.06	85.04	58.75	0.4738	0.8398	0.0162
Point 2	1	0.00	-93.69	-178.83	-121.05	-27.78	-119.19	150.07	0.5539	0.8834	0.2244
	2	0.00	-93.86	-178.33	-118.34	-26.57	-119.28	151.22	0.5533	0.8918	0.2148
	3	0.00	-93.59	-174.71	-122.65	-31.02	-124.43	147.18	0.5254	0.8581	0.1927
	4	0.00	-93.78	-175.61	-120.54	-28.98	-122.16	149.13	0.5212	0.8740	0.1684
Point 3	1	0.00	-94.35	175.93	85.50	172.40	-87.95	-10.11	0.5208	0.9867	0.0549
	2	0.00	-94.60	175.95	86.26	172.52	-84.25	-9.78	0.5586	0.9873	0.1300
	3	0.00	-94.52	175.83	87.08	172.47	-81.85	-8.91	0.5054	0.9884	0.0224
	4	0.00	-94.68	175.89	86.81	172.43	-82.10	-9.38	0.5841	0.9877	0.1805

For any of the selected force distributions, the odd harmonics can be considered well appropriated (e.g. all NNMAI values are above 0.83) and this confirms that the stepped-sine backbone is well appropriated if the structure is governed only by the odd harmonics. If all harmonics are considered, NNMAI values greater than 0.5 are obtained for the appropriated responses still provides a well appropriated NNM when compared with simulation results .

3.4.3.3 Experimental Frequency-Amplitude Results

The two NNMs previously discussed were isolated in an experiment using the previously described techniques. As discussed previously, the appropriation was probably not perfect, but seems to be as accurate as possible given the limitations of the experimental setup. Before examining the NNMs, it is beneficial to examine the two time series decays and their corresponding Morlet wavelet transform coefficients, shown in Fig. 3.16. For reference, the two decays were initiated near the previously described Point 2 and Point 3 shown in Figs. 3.5 and 3.6. Figures 3.16a and 3.16b are the time series and wavelet transform results from the Point 3 decay measured with the single point LDV at the center of the beam. The decay is initiated at 106.98 Hz, consequent of a 61.18 Hz shift in the first mode of the beam, and is expected to tracks the NNM backbone through the bifurcation of the backbone to the IR. There is a bump in the time series and in the amplitude vs. time of the fifth harmonic from the wavelet near 2.5 seconds. It will be shown later that this occurs near the 5:1 internal resonance on NNM-1.

Figures 3.16c and 3.16d show the time series and wavelet transform results from the decay from Point 2 with the same experimental setup. Although the decay is initiated at only 82.60 Hz, consequent of a 36.80 Hz shift in the first mode of the beam, the peak amplitude of the

time response prior to the decay is near that of the Point 3 decay shown in Fig. 3.16a. This can be related to the numeric results previously presented where periodic solutions can occur at two different fundamental frequencies and the same energy levels, only here this is observed in terms of peak amplitude instead of energy. For the decay of Point 2, wavelet coefficients at the 5th harmonic are on a similar scale as the fundamental harmonic as seen in Fig. 3.16d. This can be related to a larger amount of energy being transferred to the 5:1 IR NNSPS, so this harmonic will need to be included in the reconstruction of the NNM.

Similarly, a decay experiment was performed on NNM-3. Only one decay experiment is needed since no coupling was predicted in the numerical model of NNM-3. This is confirmed by examining the wavelet transform shown in Fig. 3.16f where no coupling with higher modes is present. A small but interesting "coupling" occurs with LNM-1, which can be seen near the bottom of the plot in light blue. This "coupling" only occurs once the force has been turned off and does not see any change in frequency throughout the decay. Therefore, it was concluded that the observed "coupling" is most likely a result of how the force was removed for the decay, which was not always at the static equilibrium point of the deformation of the beam, and not a true indication of nonlinear coupling in the beam. Additionally, since NNM-3 occurs at a higher frequency, the response decays in a third of the time required for NNM-1 to decay. This is a well defined occurrence in structural dynamics, but is repeated here as it can affect the ability of the wavelet transform to detect higher harmonics of the response if the sampling frequency and length of time recorded are not sufficiently large.

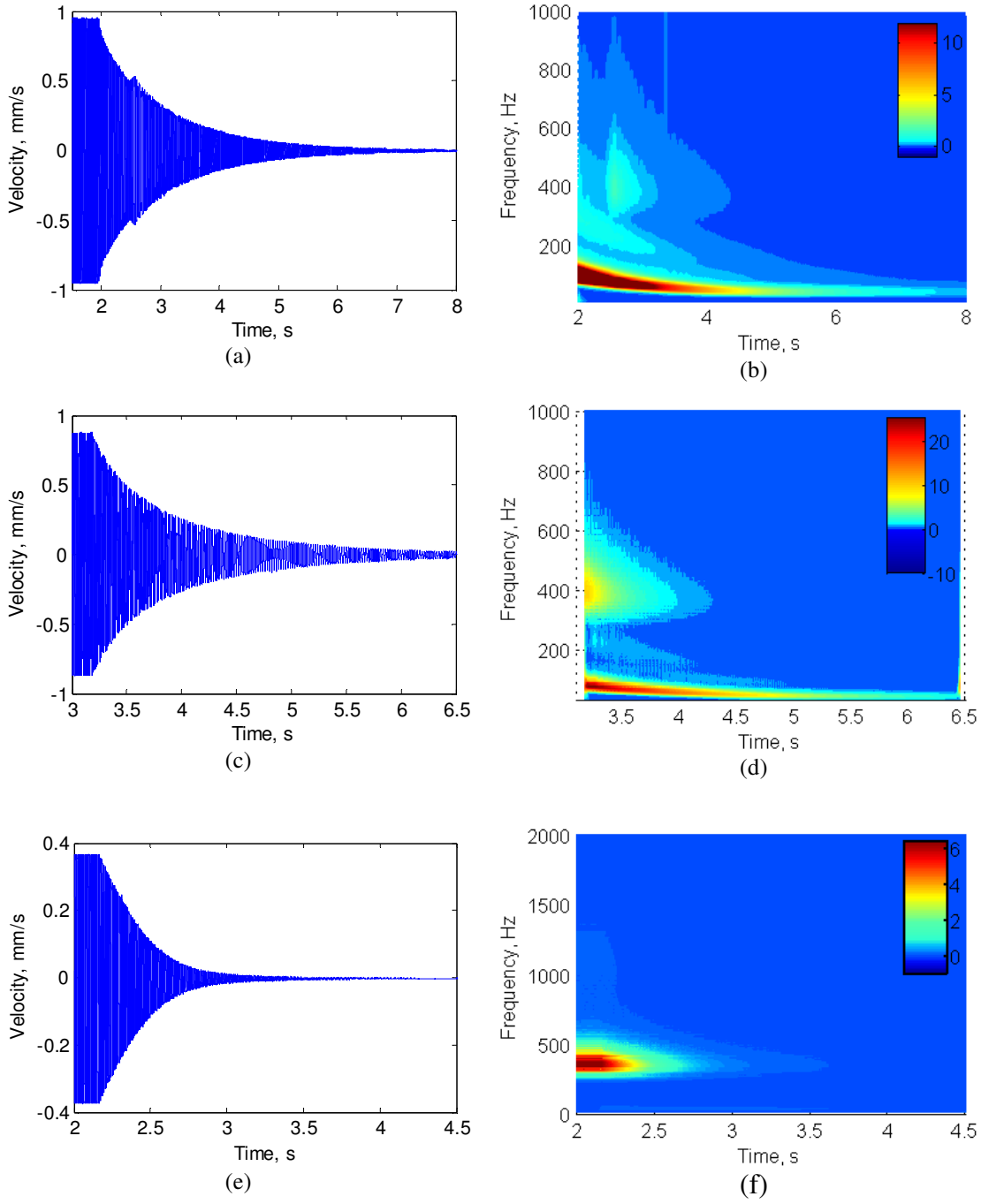

Figure 3.16: Time series and wavelet transform of the three free decays. a) Time series and b) Wavelet transform corresponding to the NNM-1 Point 3 decay, c) Time series and d) Wavelet transform corresponding to the NNM-1 Point 2 decay, e) Time series and f) Wavelet transform corresponding to the NNM-3 Point 2 decay.

For the stepped-sinusoid testing, the dominant harmonics of the response are identified in the Fourier domain, and a multi-harmonic Fourier series analysis is used to identify the amplitude of the frequency components of the signal at each point along the NNM curves. By summing the amplitudes of the higher harmonics and plotting them versus the fundamental frequency, the frequency-amplitude behavior at each point is determined. A comparison of the frequency-amplitude behavior of the single point LDV measurements is presented in Fig. 3.17 where the blue curves are related to the backbone of the NNM, the red curves are related to the IR branch of the NNM-1, and the black dot is the peak amplitude and identified mode 1 from the modal hammer tests. Since the modal hammer result lies higher up on the identified backbone, it is expected that the input hammer hits were slightly nonlinear.

For the backbone of NNM-1, the blue circles are the results from the stepped-sine testing and the blue line is the result from the Hilbert transform. At higher amplitudes, these two results compare quite favorably and they begin to deviate after the decaying time series passes the start of the IR branch. By the time the signal decays to the noise at the lowest measured amplitude, the frequency deviation is 2.71 Hz. There are at least two possible reasons for this difference. First, it is possible that the damped response simply does not follow the undamped NNM manifold as it decays, but instead follows some other path in the state space. Second, the system may have changed slightly between the stepped sine testing and the free decay measurement, causing the NNM along which the response decays to change. Indeed, there is some scatter in the lowest amplitude stepped sine responses, and this could be caused by relaxation of the beam within the clamps.

When comparing the free decay that started near the IR branch, in red, we see a larger deviation between the path followed by the free decay and the NNM. Although somewhat scattered at higher amplitudes, the stepped-sine measurements appear to capture the point of bifurcation from the backbone well and to follow up the internal resonance. This is not the case when looking at the free decay from the IR branch. The amplitude of the decaying signal has a significantly higher amplitude than the NNM estimated from the stepped-sine measurements, until the amplitude becomes low and the two curves converge. Interestingly, this free response tracks the measured stepped-sine NNM better than the free response that was initiated on the stepped sine backbone.

There are several possible explanations as to why this is could occur. First, it should be noted that the appropriated force was at a lower quality on the IR branch than on the backbone which could explain why the NNM was not as closely followed. Second, since the IR branch involves an interaction between two NNMs, it could be that the decaying response is being pulled between two attractors and hence not following either NNM precisely.

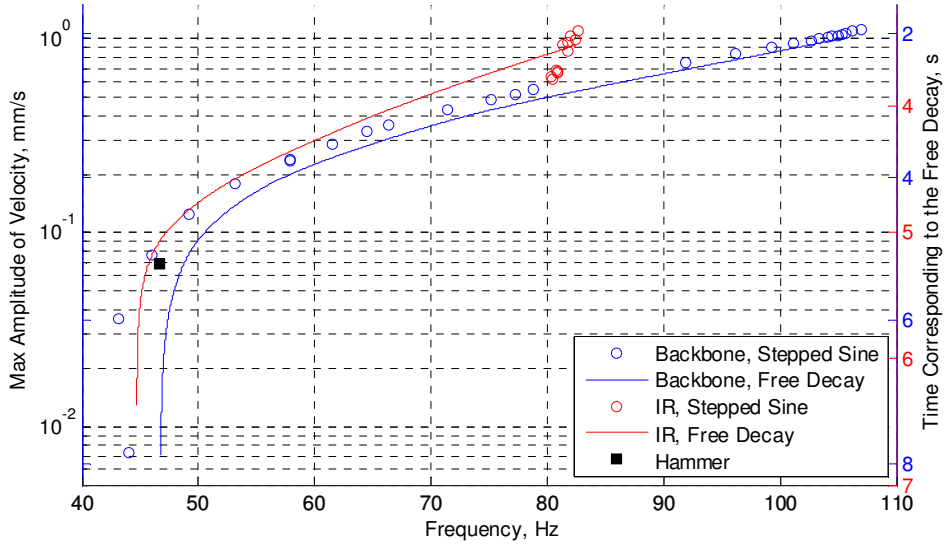

Figure 3.17: Frequency-Amplitude behavior of NNM-1 and NNM-1-3

A similar comparison can be made between the stepped sine and free decay experiments performed on NNM-3, shown in Fig. 3.18. The maximum percent error between the free decay and stepped-sine methods is 0.95%. Again, there is an offset between the free decays results and the stepped sine estimated NNM, but there was also a difference in the frequency between the linear hammer test and the stepped-sine results of 1.5%, so once again it is possible that the boundary conditions changed from one test to the next.

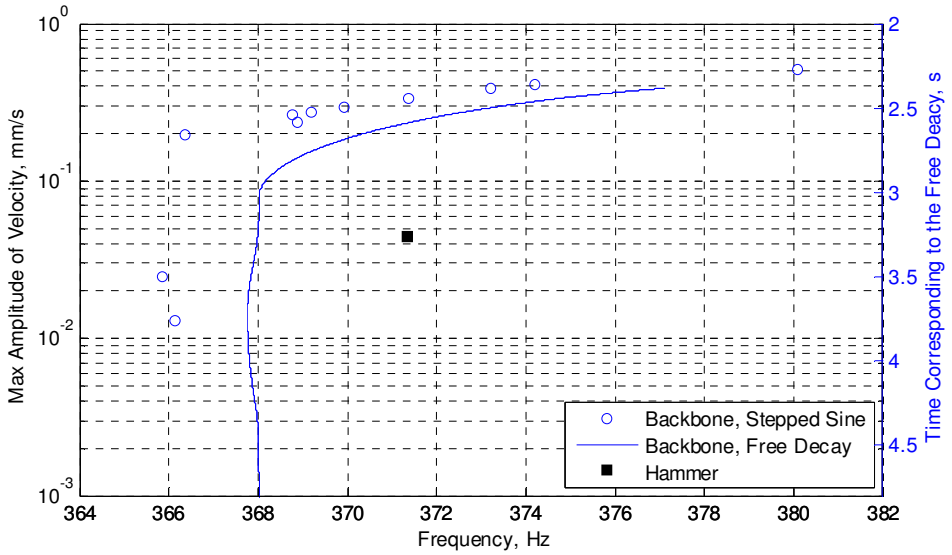

Figure 3.18: Frequency-Amplitude behavior of NNM-3

3.4.3.4 Full-Field Deformation Shapes

Another benefit to the use of stepped-sine testing is the ability to use advanced full-field measurement techniques effectively. As seen with the numerical results, the examination of the deformation shapes along the NNM for the beam provides insight to how the LNMs of the structure couple. Due to the relatively small deformation expected in the beam, continuous-scan laser Doppler vibrometry (CSLDV) is used to measure the surface using a line scan pattern as

detailed in Chapter 2. Again following the three Points identified for NNM-1 described in Fig. 3.2, the measured deformation shapes are presented in Fig. 3.19. As expected, the deformation corresponding to Point 1, Fig. 3.19a, is dominated by Mode 1. Similarly, the deformation corresponding to Point 2, Fig. 3.19c, shows the 5:1 harmonic interaction corresponding to a coupling between LNM-1 and LNM-3. It is interesting to note, that for the isolated NNM measurement at Point 3, as the beam passes through zero, there is an apparent interaction between LNM-2 that is not predicted in the simulation Fig. 3.6.

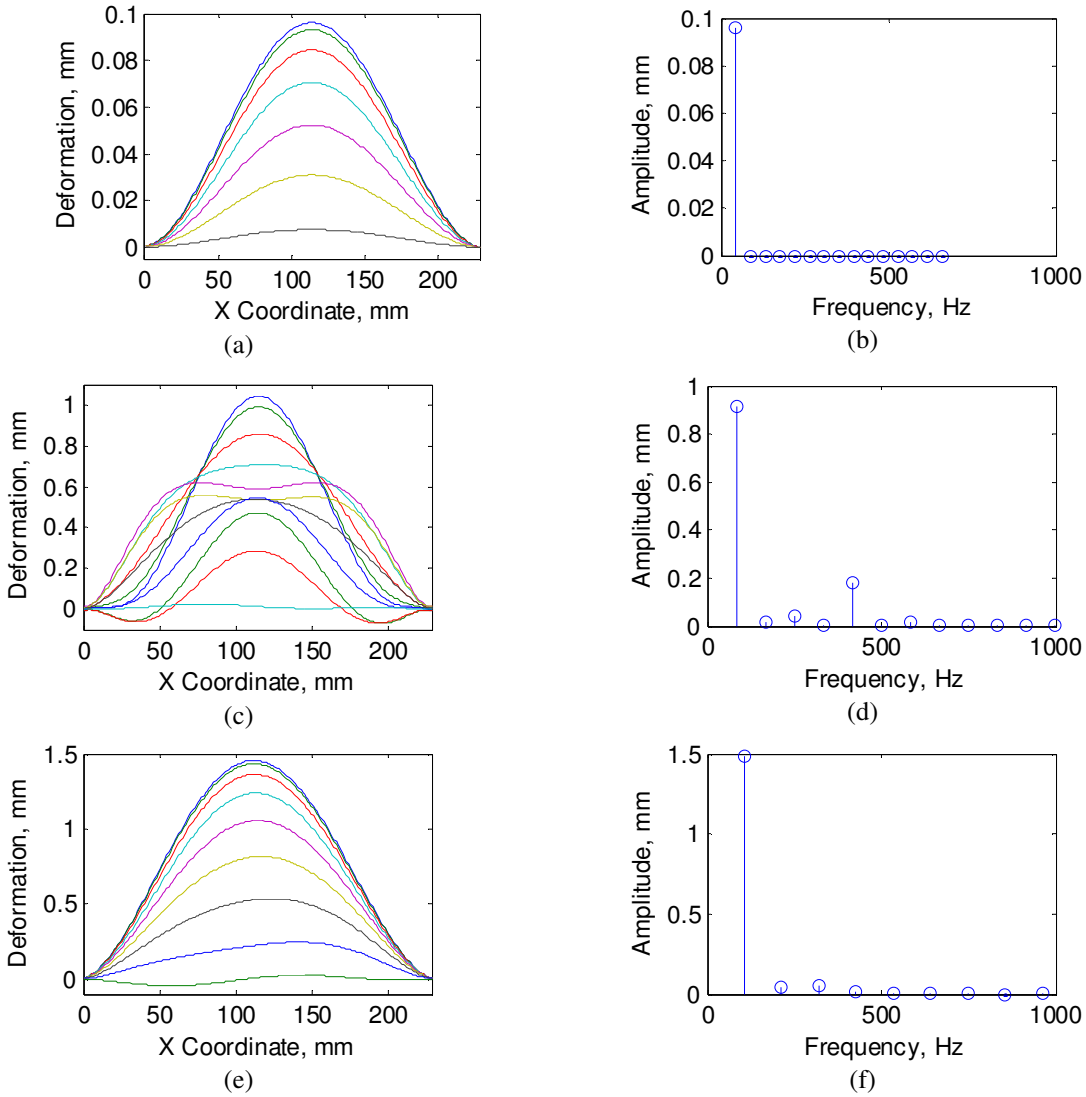

Figure 3.19: Full-Field deformation results measured with CSLDV at the three points of the

A further decomposition of the harmonics of the response and projection onto the LNMs further identify the nonlinear coupling between the LNMs. For nonlinear systems, the measurement of the deformation shapes at each harmonic also provides insight and these shapes can then be projected onto the LNMs to understand where they come from and perhaps even create a nonlinear reduced order model (NLROM) with the LNMs as a basis (as discussed in Chapter **Error! Reference source not found.**: Future Work).

3.5 *Application to Axi-symmetric Curved Plate with Geometric Nonlinearity*

3.5.1 Plate Description

The second article under investigation is a circular perforated plate with rolled ends which is shown in Fig. 3.20. A mechanical punch was used to create the circular perforations in a flat 16 gauge (1.52 mm thick) 409 stainless steel plate in an array of equilateral triangles with 10.16 mm long edges. Once this process was completed, the plate was formed around a 317.5 mm diameter mold with the excess trimmed so a lip of 12 mm remained. The plate was then welded to a 89 mm high cylinder made from a 14 gauge (1.9 mm thick) 409 stainless steel plate that was cold rolled to the 317.5 mm diameter. The welded plate assembly was then bolted to a 317.5 mm diameter by 19 mm thick aluminum fixture with twelve 6.4 mm evenly spaced holes. Due to the relatively complex processes used to create this test piece, it is important to note that all stated dimensions are nominal and subject to variation. Additionally, the processes the plate is subjected to can induce residual stresses in the structure which also might modify the dynamics of the plate in its final configuration and are not considered here.

CSLDV was not used in this experiment due to the discontinuities from the perforations. Instead the surface was prepared for high speed 3D-DIC, as shown in Fig. 3.20. 3D-DIC was able to provide the full-field measurements of the plate since there was enough room between the perforations to capture surface deformations. Additionally, Fig. 3.20 also shows the location of the single point laser Doppler vibrometers (LDV). After mounting, a single-input single-output modal hammer test was performed on the plate so natural frequencies and damping ratios could be identified. Results for the first nine modes are shown in Tab. 3.7. A linear mode shape comparison between a roving hammer test and the nominal model for the first six identified modes is shown in Fig. 3.21.

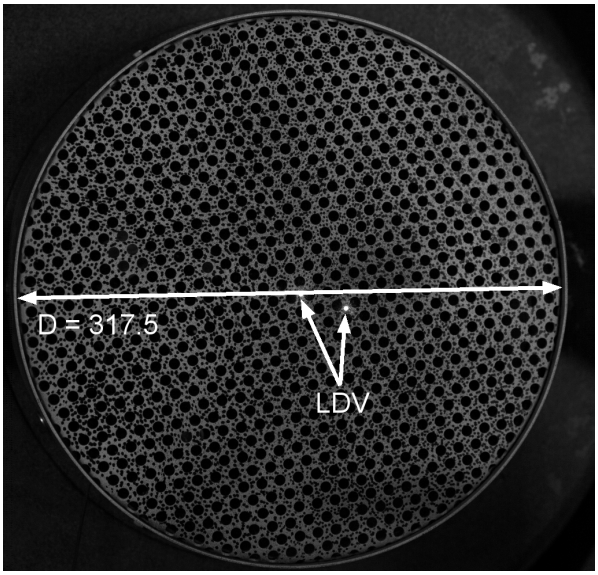

Figure 3.20: Final Mounted Perforated Plate

Table 3.7: Linear (low amplitude) natural frequencies of curved axi-symmetric plate

	Mode 1	Mode 2	Mode 3	Mode 4	Mode 5	Mode 6	Mode 7	Mode 8	Mode 9
f, Hz	202.2	324	342.8	489.7	509.9	554.1	697.2	777.9	794.2
ζ1 , %	0.2	0.13	0.31	0.092	0.15	0.087	0.11	0.49	0.43

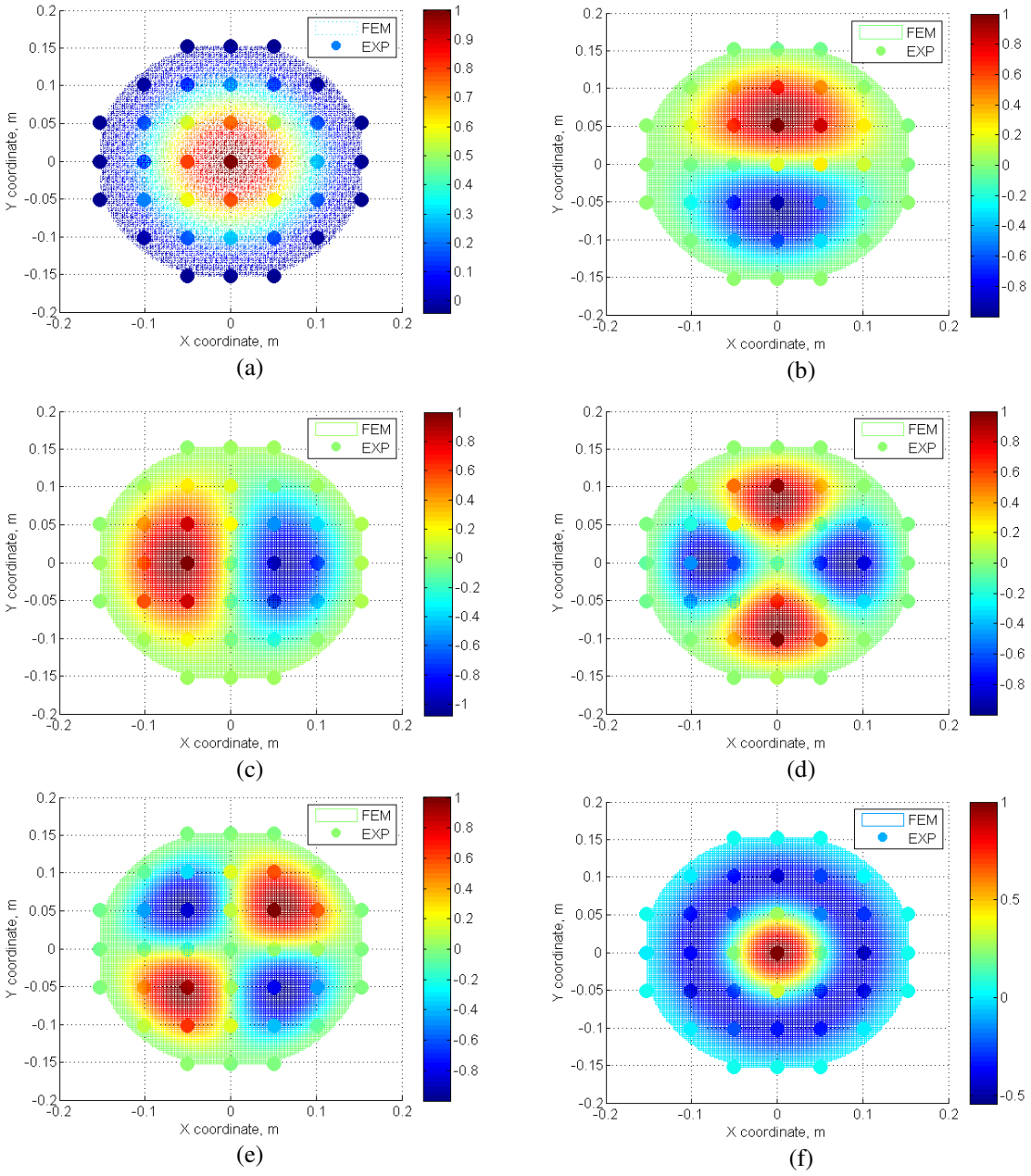

Figure 3.21: First six mode shapes for the Nominally Flat Model compared with a roving hammer test

While this system is relatively simple compared to the engine to which it is designed to be attached, the nominal model provides relatively large number of DOF than structures previously investigated in this dissertation. Since the previously discussed NNM analysis techniques have been focused on low DOF systems, a nonlinear reduced order model (NLROM)

is needed to determine the numerical NNMs of the structure. This can potentially lead to a variety of subtle details that might easily be neglected initially, and yet they could change the response considerably. Therefore, there is a greater reliance on experimental techniques in this case that can readily identify any nonlinear coupling that can occur between the LNMs. In this context, the use of full-field measurement techniques provides the information needed to confirm the NLROM captures the nonlinear behavior well.

3.5.2 Plate NNM Calculation

Fig. 3.22a shows the NNM-1 FEP for the curved axi-symmetric plate with an added line denoting 1-thickness of deformation (e.g. 1.52mm for the plate). The numerically calculated backbone was determined with a reduce-order model (ROM) where the continuation of the first linear normal mode to higher energies was isolated. While this limits the ability to calculate internal resonances in the plate, this one mode ROM still provides insight into the frequency-energy dependence of NNM-1. As observed here, the NNM undergoes a change in the characteristic nonlinearity as the fundamental frequency of vibration undergoes a decrease prior to increasing. This softening to hardening characteristic can commonly be found in curved structures [104, 105] and can be potentially damaging to the structure.

Similar to the flat beam, deformations of the curved axi-symmetric plate can also be examined at points along the FEP to explore changes of the deformation shape due to the increased response amplitudes. Since only mode 1 was used to calculate the NNM, Deformation 1 and 2, shown in Fig. 3.22b and Fig. 3.22c, are purely mode 1 shapes with different scale factors. The effect of higher modes on an initially flat axi-symmetry plate was examined numerically in [85] providing insight to the dynamics of an axi-symmetric plate, even though the

structure previously investigated was flat. Kuether found that LNM-1 and LNM-6 were both important to the description of the response along the NNM backbone providing insight to possible modal interactions, which will be explored experimentally.

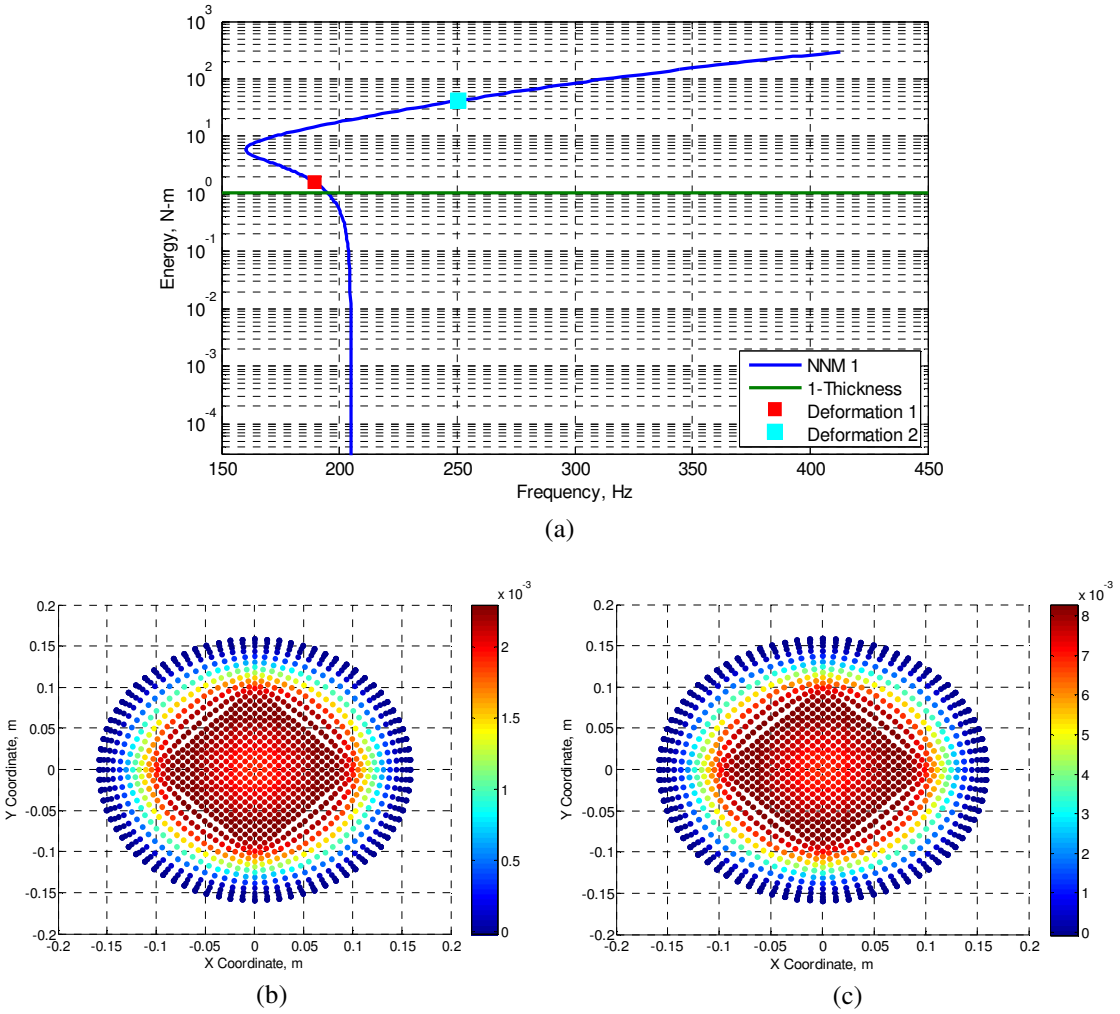

Figure 3.22: NNM 1 for axi-symmetric plate - a) Frequency-energy plot, b) Deformation 1 shape, c) Deformation 2 shape

3.5.3 Plate NNM Measurement

Following a similar methodology to that of the flat beam previously discussed, NNM-1 was experimentally measured for the curved axi-symmetric plate using 3D-DIC. Figure 3.23 shows the experimentally measured NNM of the curved axi-symmetric plate with the velocity response measured at the LDV point located at the [x,y] coordinates of [0.01,-0.03]. Similar to the numerically calculated NNM in 3.22a, the experimentally measured NNM shows the characteristic spring softening to hardening effect or a decrease of the fundamental frequency of vibration which begins to increase at a specific input force level. Unfortunately, limited data was gathered on the structure in the linear region of response due to inadequate capabilities of the shaker to obtain lower forcing amplitudes. Also, the plate cracked when a higher input force amplitude was attempted, so further testing at low amplitudes was impossible. Failure initially occurred at the [x,y] coordinates of [-0.01,-0.01] which can be identified in 3.23c and d. With the use of high speed 3D-digital image correlation, maximum deformation shapes of the plate at low and higher energy are shown in 3.23b-e. Figures 3.23b and c show the deformation shape at an instant in time at the low energy point marked “deformation 1” in 3.23a. The deformation at this frequency-energy point resembles mode 1 of a flat plate as expected in linear results. Figure 3.23d & e show the deformation shape at the high energy point, or deformation 2 also shown in 3.23a.

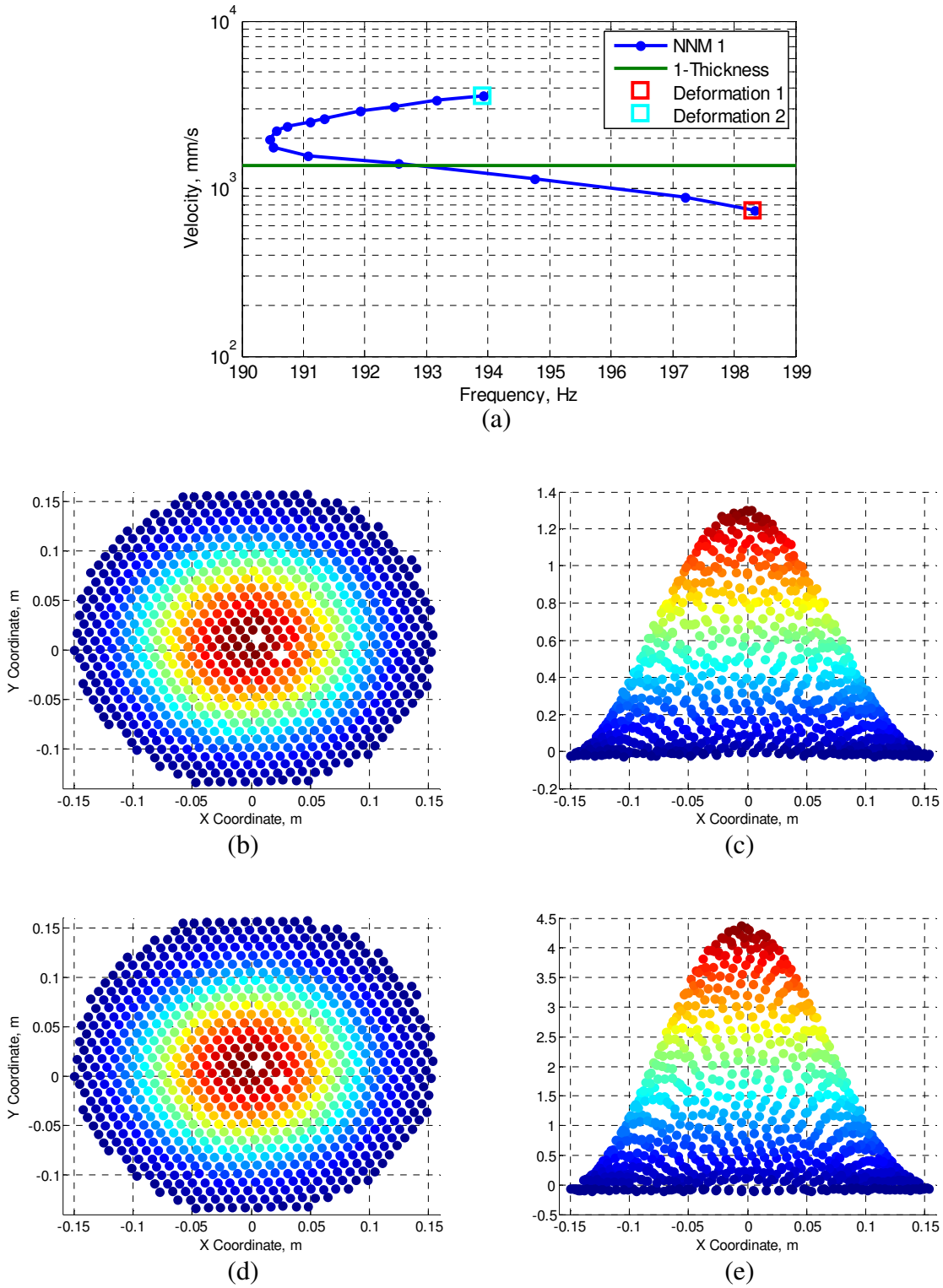

Figure 3.23: Experimental NNM 1 for axi-symmetric plate- a) Frequency-velocity plot, b) Deformation 1 shape, c) Deformation 2 shape

To obtain further insights, the measured response is decomposed into its harmonics in Fig. 3.24a. Interestingly, this shows that while the fundamental harmonic is dominant at low amplitude, as the response begins to turn from softening to hardening the higher harmonics become large in the response. This is evident as the third harmonic of the measured velocity is near equal to the first harmonic when the plate fails. Hence, while no internal resonances are present the response of this NNM is multi-modal along the backbone. Unfortunately, the phase of the harmonics, shown in 3.24b, reveal that the higher harmonics for the plate are not in quadrature with the input force. So one cannot be sure that the NNM has been completely isolated; however, since the excitation is mono-harmonic the phases of the higher harmonics could be miss-leading since no force has been added. The first harmonic stays near 180 degrees phase, but it is less accurate in the spring hardening regime, or on the lower amplitudes of the response.

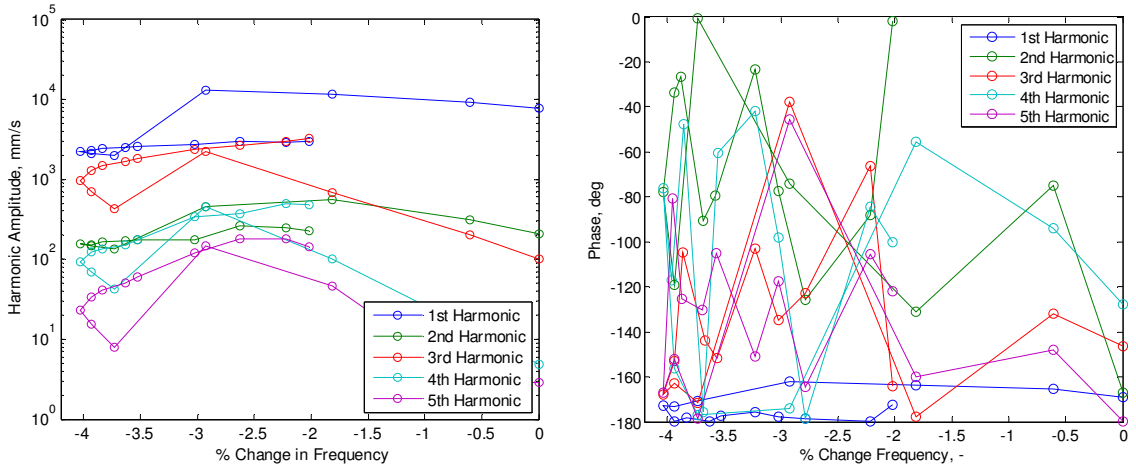

Figure 3.24: NNM results for the axi-symmetric plate - a) FFT amplitude of harmonics in the response and b) Phase results of harmonics in the response

The full field deformation shapes were examined for each harmonic to better understand the evolution of the response along the backbone, and are shown in Fig. 3.25. It is particularly interesting to note that the response near the third harmonic deforms in a shape similar to the sixth linear mode of the plate. In [85] a finite element model of a similar plate (but with no initial curvature) was studied and LNM-1 and LNM-6 were both found to be important to describe the response along the NNM-1 backbone. These experimental results corroborate this finding. At the highest level on the FEP, the measurements show that the magnitude of the third harmonic of the velocity response at the center of the plate is on the same order of the fundamental harmonic. This indicates the level of the harmonic coupling observed experimentally. By examining the deformation shape at this harmonic, it is observed that this harmonic coupling corresponds to a modal coupling between LNM-1 and LNM-6 of the plate. It is also interesting to note that the fundamental harmonic experiences a broadening in the peak curvature of the deformation shape when comparing deformation 1 and deformation 2, shown in Figs. 3.25a and b. This broadening and the strong modal coupling could be the root causes to the failure that observed in the plate.

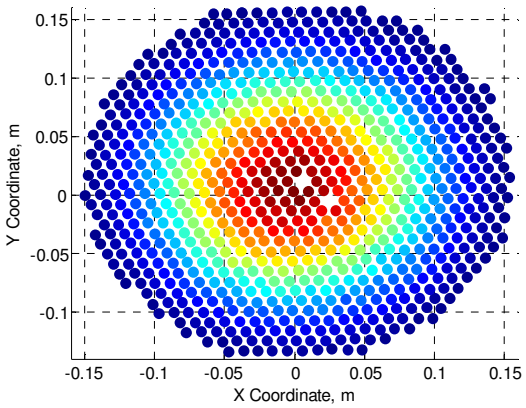

(a) Def 1, 1st harmonic

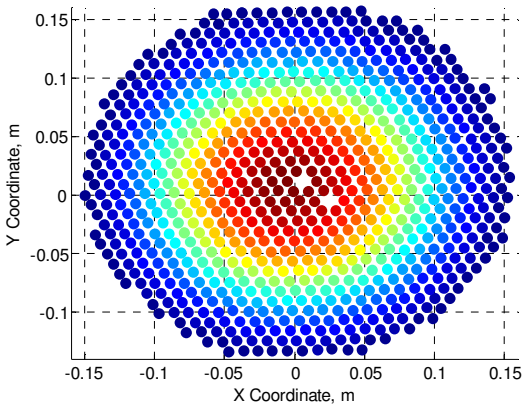

(b) Def. 2, 1st harmonic

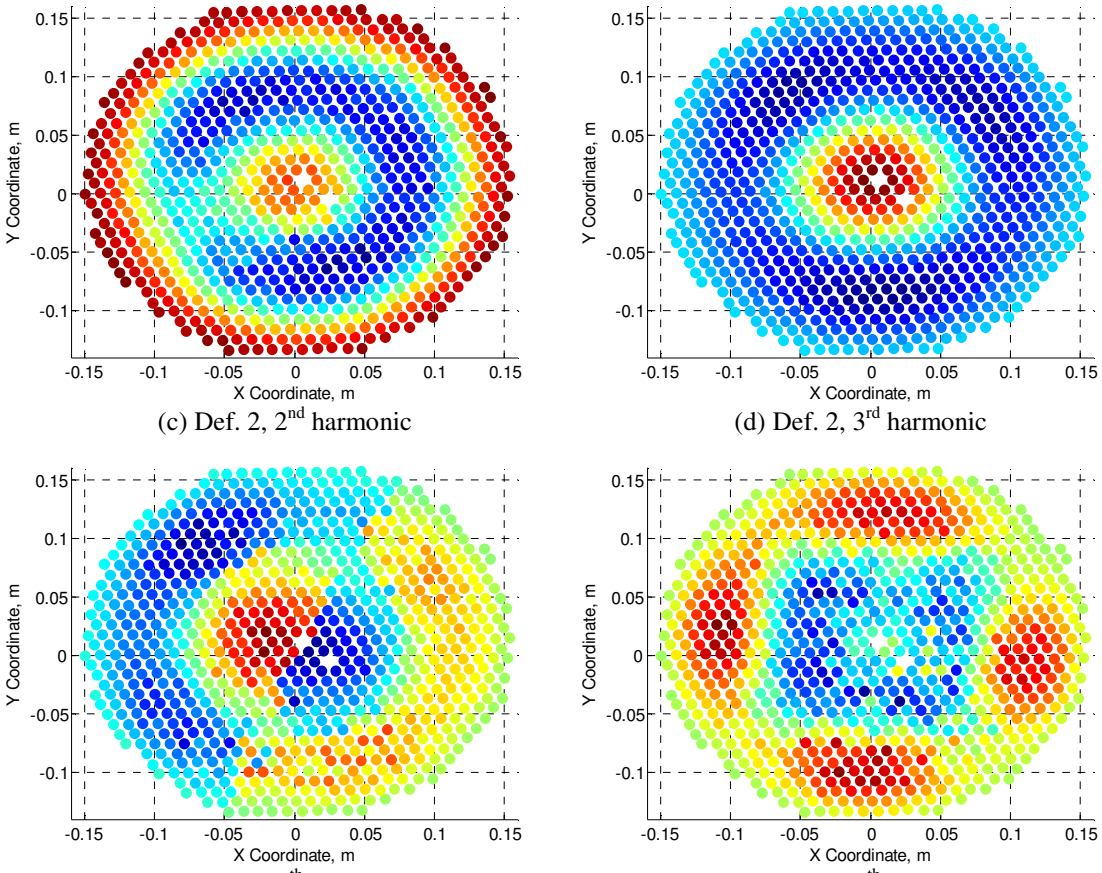

(c) Def. 2, 2nd harmonic (d) Def. 2, 3rd harmonic

(e) Def. 2, 4th harmonic (f) Def. 2, 5th harmonic

Figure 3.25: Deformation patterns of plate at various harmonics for two points along the backbone curve: a) 1st harmonic of deformation 1, b-f) 1st harmonic, 2nd harmonic, 3rd harmonic, 4th harmonic, and 5th harmonics respectively of deformation 2

3.6 *Summary*

The results shown here demonstrate the capability of mono-harmonic force appropriation to isolate NNMs in two structures exhibiting rich dynamics. Additionally, it was shown that higher harmonics are needed in the input force to fully appropriate a NNM when there is strong harmonic coupling between the LNMs of a structure. The measured response of the flat beam shows the ability to achieve a quality dynamic response in the neighborhood of the beam's first NNM with mono- and multi-harmonic forcing. In addition to capturing the expected frequency-energy relationship, a modal interaction between the first and third mode of the beam was identified and isolated. The measured response of the curved axi-symmetric plate also shows the

ability to achieve a dynamic response in the neighborhood of the first NNM of a more complex structure. The quality of the appropriated response for the plate was not on the same level of the beam when looking at the phase of the input and response possibly demonstrating a limitation of a mono-harmonic force to appropriate the response in the neighborhood of the expected NNM.

For both structures investigated, full-field deformation measurements were key to the identification of nonlinear coupling between the LNMs of the structure. These measurements are particularly beneficial when examining the more complex curved axi-symmetric plate, since the ability of current modeling techniques limits the full examination of the structures nonlinear properties. With the identification of the nonlinear coupling of the LNMs, experimental nonlinear modal models can be created and tuned to better match the nonlinear dynamics. This idea emphasizes an important area this work can be expanded upon where nonlinear modal analysis techniques can be used to examine nonlinear coupling between LNMs tying together linear and nonlinear experimental modal analysis.

4 Model Updating and Validation using Experimentally Measured Linear and Nonlinear Normal Modes

4.1 *Introduction*

When the comparison between model and experiment reveals that the model is inaccurate, it is important to determine which model parameters or features in the model should be updated to improve the correlation. Typically, each of these parameters is slightly perturbed to see whether they cause important changes in the validation metrics used (e.g. linear natural frequencies and mode shapes). While brute force approaches based on optimization are used in some applications, in this work the focus is on a physics based approach where the only parameters updated are those that are justifiably uncertain.

Since elastic geometric nonlinear deformations are examined here, nominal dimensions and material properties are used to build an initial model with the focus being the characterization of the static equilibrium position. The error between the calculated and measured natural frequencies are then used to update material properties and boundary conditions providing models that better represent the structure's linear dynamics using well established techniques [4]. Additionally, the structures' NNMs are used as a validation metric after changes are made to the material properties and boundary conditions of the initial model based on its linear modal parameters. Since NNMs are not directly used in the model updating procedure, the updated models may or may not improve the correlation of the NNMs (e.g. the extension of the linear modes to higher energy). Hence, the results show that it is critical to simultaneously consider both the linear and the nonlinear behavior of the model in the model updating process.

The model updating approach is demonstrated in this chapter on two structures, a nominally flat and a nominally curved beam with rigid (nominally clamped) boundary conditions.

4.2 *Modeling Considerations*

Although beams are relatively simple structures, validating FEMs with experimental measurements involves some engineering judgment and physical insight to the inherent uncertainty of the total physical assembly. For the clamped-clamped beams under investigation, uncertainties in initial geometry, material properties, and boundary conditions are expected to dominate variations in the dynamic response. Therefore, a general model, shown schematically in Fig. 4.1 **4.1**for the flat beam, is considered. In Fig. 4.1, K_A represents the axial stiffness of the boundary, K_T the transverse stiffness, K_θ the rotational stiffness of the boundary, the black line represents nominal geometry, and the orange line represents the measured initial geometry. The starting point for the model updating procedure uses the nominal geometry (shown in black), nominal material properties, and fixed boundary conditions ($K_A = K_T = K_\theta =$ infinity). Variations in the initial geometry (shown in orange) are taken into account with the use of full-field coordinate measurements of the beam surface. The remaining variation between the model and measurements are accounted for the in the modulus of elasticity and boundary conditions.

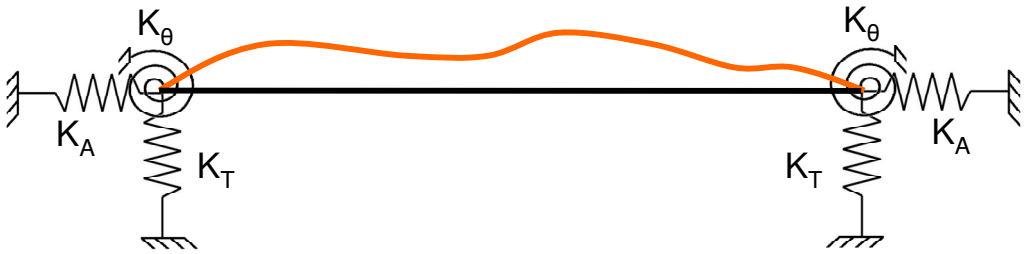

Figure 4.1: Boundary Condition Schematic

4.3 *Model updating of Clamped-Clamped Flat Beam with Geometric Nonlinearity*

4.3.1 Flat Beam Description

Again, a precision-machined feeler gauge made from high-carbon, spring-steel in a clamped configuration is first examined. The beam has an effective length of 228.6mm, a nominal width of 12.7mm, and a thickness of 0.762mm but dimensions are nominal and subject to variation from clamping and from the machining process to obtain the desired thickness. Prior to clamping, the beam was prepared for three dimensional digital image correlation (3D-DIC) and continuous-scan laser Doppler vibrometry (CSLDV) as discussed in [42] and shown in Fig. 4.2**4.24.2**. The clamping force was provided by the four 6.35-28 UNF-2B bolts located on the inside of the clamping fixture and tightened to 7 N*m. Before and after clamping the beam in the fixture, static 3D-DIC was used to measure the initial curvature of the clamped beam and the result is shown in Fig. 4.2**4.2**b. It is interesting to note that although the beam is assumed to be nominally flat, before and after clamping the beam has an initial deflection of 4% and 0.01% of the beam thickness, which is not obvious to the observer. This change of initial curvature has little effect on the linear analyses, but could change the characteristic nonlinearity of the beam (e.g. softening to hardening effect) which will be shown later in this section. A 7^{th} order polynomial, shown in Fig. 4.2c, was then fit to the measured curvature and used to approximate the initial geometry. The polynomial was used to build the initially updated models

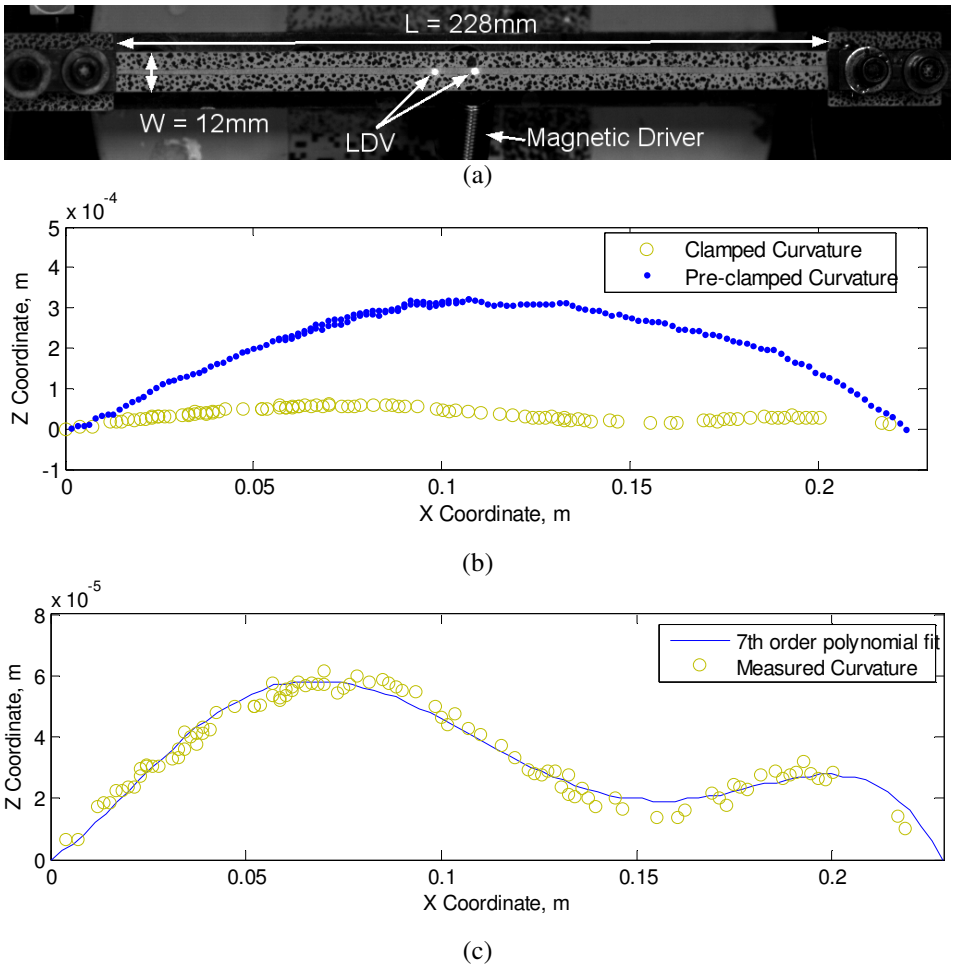

Figure 4.2: Flat Beam in Clamp: a) XY Plane image of beam, b) measured XZ geometry of beam

4.3.2 Flat Beam Linear Comparison

Four finite element models were created to explore the effect of the model parameters on the linear and nonlinear dynamics. All models used 81 Abaqus® beam elements evenly spaced along the x-coordinate of the beam. For each model, linear natural frequencies and mode shapes were calculated and used for comparison with the experimentally measured natural frequencies. The first model created was based on the nominal dimensions previously described and under the assumption of fixed boundary conditions. As seen in Tab. 4.1, the natural frequencies of the

nominal beam model did not match well with the measured values resulting in large percent error between the two sets of natural frequencies with a RMS value of 27.53 (PE_{RMS}=27.53).

The second model created updated the initial geometry of the beam to include the measured curvature of the beam, but the fixed boundary conditions were retained (e.g. $K_A = K_T = K_\theta$ = infinity). The addition of curvature to this model showed a decrease in frequency in all modes (PE_{RMS}=25.99) and a reduction in percent error when compared with the measured values, but percent errors were still not within ±5%.

The third model created took into account variations in boundary conditions by including the axial (K_A), transverse (K_T), and torsion (K_θ) springs at the boundaries schematically shown in Fig.**4.2** 4.2. Initial values for these springs were based on results from [67] and are shown in Tab. 4.2. Adding these springs further lowered the natural frequencies of the FEM of the beam, but percent errors were still out of acceptable ranges (PE_{RMS}=24.40), so variation in the elastic modulus and boundary condition springs was allowed to better match the model to the experiment.

Using gradient based optimization and constraining the change in modulus to the maximum value in literature, this lead to a factor of 100 increase in the axial and transverse spring values and a factor of 0.5 decrease in the torsion springs value. This updated model brought the error in the natural frequencies within an acceptable range of error for the first four modes as seen in Tab. 4.1 (PE_{RMS}=20.86). Next the modulus was allowed to vary from 2.31 GPa to 2.74 GPa, and gradient based optimization was again performed resulting in a factor of 1000 increase in the axial spring, a factor of 0.000001 decrease in the transverse spring, and factor of 0.71 decrease in the torsion spring value. This resulted in smaller frequency error with all but the 5th mode (PE_{RMS}=20.06). With the fully updated models, it is interesting to note that the large

variation in boundary conditions are not surprising for the clamped-clamped configuration used and can make updating difficult. Also, with the increase of modulus, it is expected that pre-stress from clamping needs to be accounted, but is not attempted in this work.

Table 4.1: Flat Beam Correlation Results

Mode	Test, Frequency	Nominal Flat Beam	% Error	IC-FF Initial Curvature, fixed-fixed	% Error	IC-NS Initial Curvature, Nominal Boundaries	% Error	IC-US Initial Curvature, Updated Springs	% Error	IC-USM Initial Curvature, Updated Springs/ Modulus	% Error
1	65.05	79.02	21.47	78.18	20.18	76.97	18.32	65.82	1.19	65.31	0.40
2	194.86	217.92	11.84	215.61	10.65	212.29	8.95	189.37	-2.82	193.16	-0.87
3	394.31	427.46	8.41	422.38	7.12	415.98	5.50	382.78	-2.92	394.00	-0.08
4	661.42	707.15	6.91	698.12	5.55	687.67	3.97	647.55	-2.10	665.11	0.56
5	856.16	1057.30	23.49	1042.90	21.81	1027.50	20.01	984.82	15.03	1000.70	16.88
6	995.53	1478.40	48.50	1456.80	46.33	1435.50	44.20	1395.20	40.15	1392.00	39.83
7	1397.83	1970.70	40.98	1939.80	38.77	1911.70	36.76	1879.00	34.42	1827.60	30.75

Table 4.2: Updated Elastic Modulus and Spring Values for the Flat Beam

	E, Pa	K_A, N/m	K_T, N/m	K_θ, N*m/rad
IC-NS	$2.00*10^{11}$	$3.50E*10^{08}$	$5.20*10^{08}$	113
IC-US	$2.31*10^{11}$	$3.50E*10^{10}$	$3.97*10^{10}$	5.65
IC-USM	$2.74*10^{11}$	$1.09E*10^{13}$	$1.71*10^{05}$	4.03

4.3.3 Flat Beam Nonlinear Comparison

As the beam's response increases into a nonlinear regime, the fundamental frequency of vibration becomes a function of input energy. Instead of calculating the energy of the beam at increased force levels from the experiment, the directly measured maximum displacement at the center point of the beam is used to create a frequency-displacement plot for comparison between analysis and test. The first NNM was calculated for each model created during the model updating process using the applied modal force method [52] and are presented in Fig. 4.2.

Fig. 4.2a shows the frequency-displacement plots for each step of the model updating, and emphasizes that as the linear frequency converges to the desired value, the nonlinearity experiences a drastic change in the frequency-energy relationship. By scaling the frequency of the representative FEP to the model's linear natural frequency, this relationship is further emphasized as seen in Fig. 4.2b. Starting with the flat fixed-fixed beam, shown in blue, the nonlinear frequency-energy relation changes with each successive change in the model parameters. The greatest change in the nonlinearity is observed when the initial curvature is added to the model, shown in green. This occurs because a curved beam is less stiff axially, so as bending and axial deformations couple, the stiffening effect on the bending modes is not as great as with a flat beam. When compared with the flat fixed-fixed beam, the updated geometry changed the first linear natural frequency 1.1% while the frequency-displacement relationship for NNM 1 was reduced by approximately 50% for the input range investigated, showing the sensitivity of the nonlinearity to initial geometry. With the addition of boundary condition springs, the linear model showed a decrease of 1.5% of the first natural frequency, where NNM 1 showed an increase in the frequency-displacement relationship of 5%. This shows that the relationship between the change in linear natural frequency and the nonlinear frequency-displacement relationship is not linear in nature, as expected. The remaining two models showed a larger change in the first linear natural frequency than in the nonlinear portion of the representative FEP.

Based on the results of the comparison in Fig. 4.2 and Tab. 4.1 it appears that either of the models denoted IC-US or IC-SM should accurately describe the dynamics of the beam when dominated by the first mode. Improved accuracy in the nonlinear region of the model could be

made with the inclusion of pre-stress. Similar comparisons can also be made with higher NNMs if the response is dominated by higher modes.

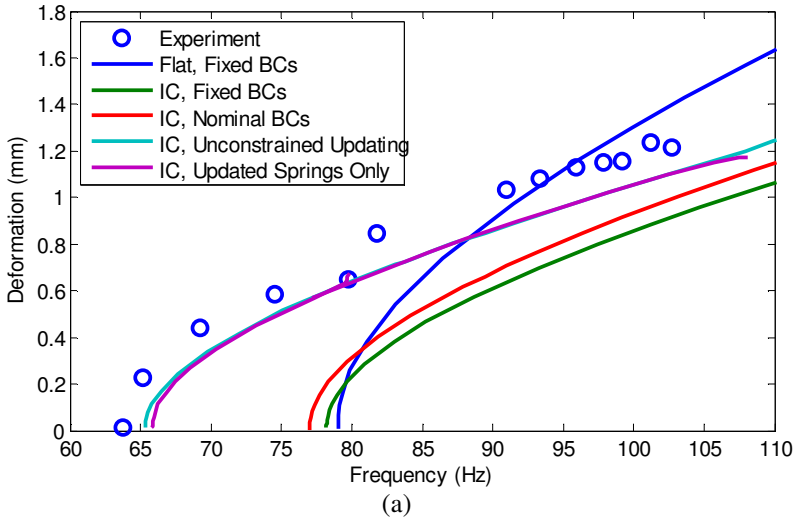

(a)

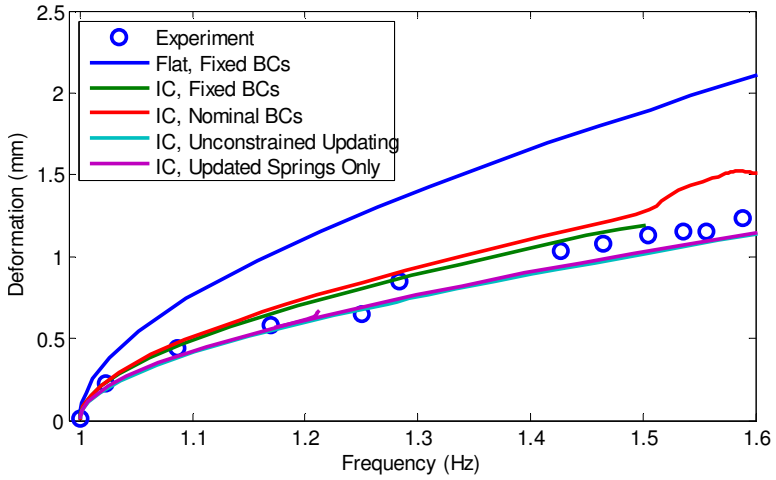

(b)

Figure 4.3: Maximum Displacement Backbone Curves of Center Point of Beam: a) Linear and nonlinear comparison, b) Nonlinear comparison with scaled to the linear frequency

4.4 *Model updating of Clamped-Clamped Curved Beam with Geometric Nonlinearity*

4.4.1 Curved Beam Description

The second structure investigate is a cold rolled curved beam made from high-carbon, spring-steel in a clamped configuration. The beam has an effective length of 304.85mm, a nominal width of 12.7mm, and a thickness of 0.508mm. The cold rolling was done to induce an initial curvature of 3048mm, but as with the flat beam, all presented dimensions are nominal and subject to variation. The clamping force was provided by the two 6.35-28 UNF-2B bolts located on the inside of the clamping fixture, which is the same fixture used in [39].

Before and after clamping the beam in the fixture, static 3D-DIC was again used to measure the initial curvature of the clamped beam as shown in Fig. 4.4b. It is observed here that the clamping induces an asymmetric preload to the final configuration of the beam, which is not accounted for in the model. Similar to the flat beam, an 8^{th} order polynomial was then fit to the measured curvature and used to approximate the initial geometry of the beam as shown in Fig. 4.4c. As with the flat beam, single-input single-output modal hammer tests were performed throughout testing on the curved beam to identify natural frequencies and damping ratios. Results from these hammer tests showed a 7% variation in the first natural frequency of the final clamped beam, which can be expected due to the variation in the experimental setup.

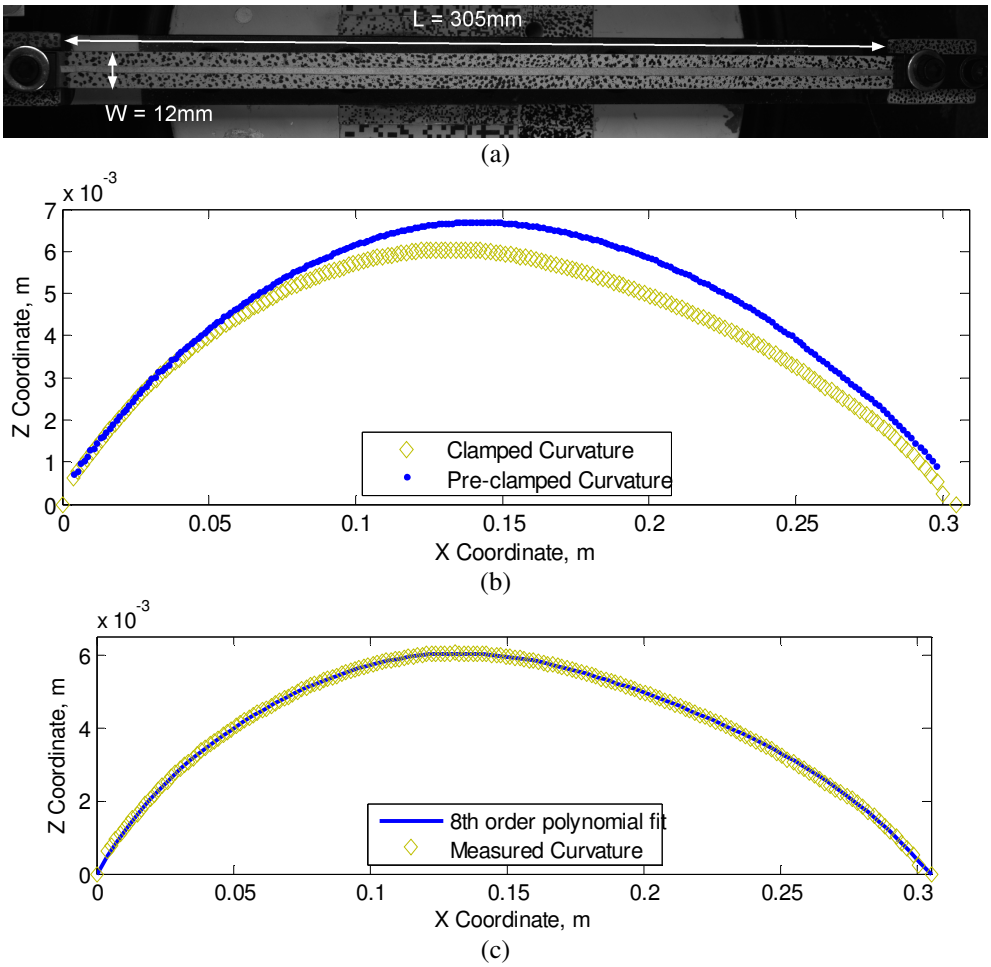

Figure 4.4: Curved Beam in Clamp: XY Plane image of beam, b) XZ geometry of beam

4.4.2 Curved Beam Linear Comparison

The model updating procedure described for the nominally flat beam was repeated for the nominally curved beam. Again, four finite element models were created and each model used 81 Abaqus® beam elements evenly spaced along the x-coordinate of the beam. For each model, the linear natural frequencies and mode shapes were calculated and used for comparison with the experimentally measured natural frequencies.

The first model created was based on the nominal dimensions previously described for the curved beam and under the assumption of fixed boundary conditions. As seen in Tab. 4.3, the

natural frequencies of the nominal beam model again did not match well with the measured values as the percent frequency error between the models had an RMS value of 16.98 (PE_{RMS}=16.98).

The second model created updated the initial geometry of the beam to include the measured curvature of the beam, but the fixed boundary conditions were retained (e.g. $K_A = K_T = K_\theta$ = infinity). The addition of curvature to this model showed an increase in frequency in all modes and a reduction in frequency errors (PE_{RMS}=4.41) when compared with the measured values, with modes 4 and 5 outside the desired ±5%.

Since a similar clamp was used, the third model created used the same nominal values for the boundary condition springs that were used for the flat beam as shown in Tab. 4.4. The addition of these springs had varying effects to the natural frequencies of the beam (PE_{RMS}=4.03), but the frequency errors for modes 4 and 5 were still larger than desired.

The elastic modulus and boundary condition springs were varied using gradient based optimization while also constraining the change in modulus to the maximum value in literature. This lead to a factor of 10^7 increase in the axial spring stiffness, a factor of 100 increase in transverse spring, and a factor of 6000 increase in the torsion springs value. This updated model reduced the error in modes 4 and 5, but overall the errors in the natural frequencies (PE_{RMS}=7.02) are larger than for the model with nominal boundary springs and the large error in the first natural frequency is certainly a concern.

Finally, the modulus was allowed to vary from 2.31 GPa to 2.76 GPa, and gradient based optimization was again performed resulting in a factor of 10^5 increase in the axial spring and no change in the transverse and torsion spring values. This updated model brought all natural

frequencies within about 2% of the measured values (PE_{RMS}=1.08), with many of the frequency errors well below 1%, so no further tuning was attempted.

Table 4.3: Curved Beam Correlation Results

Mode	Experiment	Nominal Curved Beam	% Error	IC-FF Initial Curvature, fixed-fixed	% Error	IC-NB Initial Curvature, Nominal Boundaries	% Error	IC-US Initial Curvature, Updated Springs	% Error	IC-USM Initial Curvature, Updated Springs/ Modulus	% Error
1	87.33	78.96	-9.59	85.43	-2.18	85.04	-2.62	78.41	-10.22	85.48	-2.12
2	151.48	132.14	-12.77	151.22	-0.17	150.26	-0.81	138.80	-8.37	149.60	-1.24
3	296.03	216.12	-26.99	294.98	-0.36	293.68	-0.79	270.77	-8.53	295.56	-0.16
4	319.72	256.00	-19.93	346.63	8.42	343.67	7.49	318.22	-0.47	318.36	-0.43
5	508.20	387.34	-23.78	559.21	10.04	555.17	9.24	513.34	1.01	511.38	0.63
6	620.41	534.43	-13.86	623.46	0.49	620.77	0.06	572.40	-7.74	620.23	-0.03
7	841.58	712.89	-15.29	873.25	3.76	869.19	3.28	801.77	-4.73	851.01	1.12
8	1057.02	914.52	-13.48	1056.80	-0.02	1052.40	-0.44	970.60	-8.18	1057.80	0.07
9	1326.11	1143.20	-13.79	1340.10	1.05	1334.50	0.63	1231.00	-7.17	1333.50	0.56
10	1583.64	1396.70	-11.80	1609.80	1.65	1603.00	1.22	1479.00	-6.61	1612.90	1.85

Table 4.4: Updated Elastic Modulus and Spring Values for the Curved Beam

	E, Pa	K_A, N/m	K_T, N/m	K_θ, N*m/rad
IC-NB	$2.00*10^{11}$	$3.50*10^{08}$	$5.20*10^{08}$	113
IC-US	$2.31*10^{11}$	$1.56*10^{15}$	$5.20*10^{10}$	$6.93*10^{05}$
IC-USM	$2.76*10^{11}$	$1.79*10^{11}$	$5.20*10^{10}$	$6.93*10^{05}$

4.4.3 Curved Beam Nonlinear Comparison

As previously shown, the increased curvature in the curved beam induces a change in the nonlinear behavior. Previous results have shown that the numerical model and experimental measurement displayed a spring softening to spring hardening characteristic for NNM 1. The comparison between analysis and measurement is shown in Fig. 4.5. Fig. 4.5a shows the un-scaled results emphasizing the discrepancy between the liner and nonlinear part of the NNM. Fig. 4.5b shows the scaled results emphasizing the differences in the nonlinear behavior. As

shown in Fig. 4.5b, the nominally curved model, shown with a blue line, and the experiment, shown with blue circles, show a large difference in the "turning point", or change from spring softening to spring hardening, of the characteristic FEP. When the initial curvature of the beam is changed to match the measured shape of the beam, the result shown with a green line reveals that the characteristic of the nonlinearity changes to initially spring hardening and then spring softening; this is the opposite of what is observed experimentally. So, even though this change to the model improves the correspondence of the linear natural frequencies, this comparison reveals that the model now represents the nonlinear behavior less accurately.

The models IC-NB and IC-US with nominal and updated values for the boundary condition springs also predict initial hardening and then softening, further underscoring the fact that updating the model based on its linear behavior alone is not sufficient to bring the nonlinear behavior into agreement. It is also interesting to note that while the large changes (10^7 change in axial spring, 10^2 change in transverse spring, and the 10^3 change in torsion spring) change the location of the turning point in the FEP, the hardening to softening characteristic is maintained; apparently this characteristic is a function of the geometry alone or of some other parameter that was not considered. Although the linear portion of the fully updated model matches experiment well, it does not do any better at capturing the nonlinearity. So, further updating will be needed to bring this model into correspondence with measurements. Considering Fig. 4.4, it could be posed that pre-stress in the beam due to clamping into the fixture may be important, so it will be allowed to vary in future models.

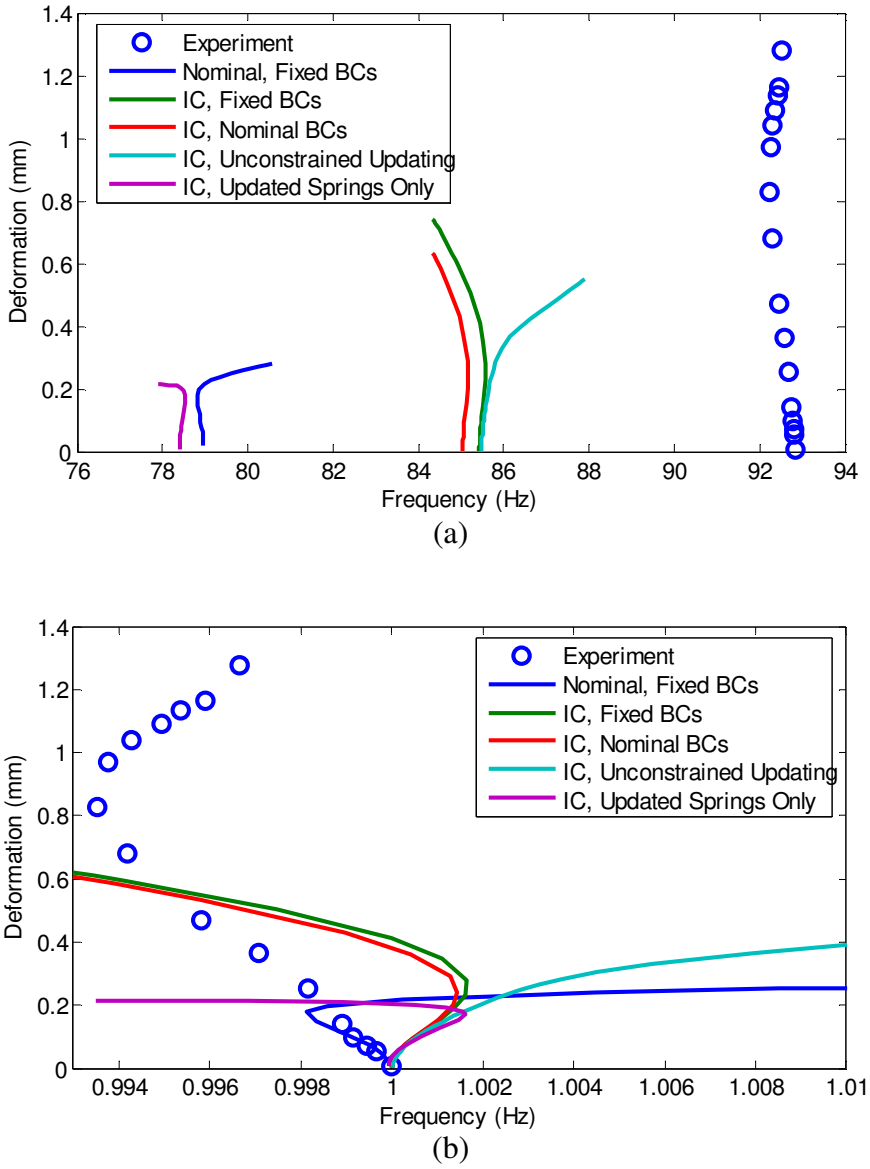

Figure 4.5: Maximum Displacement Backbone Curves of Quarter Point of Curved Beam: a) Linear and nonlinear comparison, b) Nonlinear comparison

4.5 *Summary*

Through the examination of single point responses on each of the beam's surface, the frequency-displacement relationship is presented. For the nominally flat beam, the inclusion of this curvature is an important step to the accurate estimation of the nonlinear energy dependence

of the fundamental frequency of vibration. Additionally, through the change of boundary conditions, this energy dependence can be tuned to match experimental measurements. Here, it is important to include axial and transverse springs due to the small initial curvature. If the beam was flat, only axial springs would be needed for model updating and tuning of the nonlinearity, but for the presented results, the transverse springs were as significant as the axial springs. For the nominally curved beam, changing the curvature and boundary conditions has been shown to change the fundamental characteristic of the nonlinearity inherent to the structure. Therefore, more care must be taken in the model updating procedure to ensure that the true nonlinearity is accounted.

Future work will seek to add effects from asymmetries and pre-stress induced from clamping. With the use of NNM force appropriation and full-field measurements, as described in [45], an examination of the effect of asymmetries to the dynamic response is possible. With the examination of the change in mode shapes at higher response levels, more insight can be gained for the improved correlation of the nonlinearity, which would be especially information for structures with complex changes in nonlinearity (e.g. the curved beam). Also, work will seek to use NNM backbones as a quantitative metric for nonlinear model updating using a global metric instead of through the uses of full-field experimental and numerical data examining only single location responses. The addition of full-field deformations shapes gives additional clues about how we might need to update the model to improve validation of the NNMs.

5 Summary

This dissertation has contributed to the state of the art in several areas. First, two advanced full field measurement methodologies were compared and found to be useful when characterizing nonlinear deformations of thin structures. The full field measurements that they provide were found to give unique insights into how the linear modes couple, information which could be helpful when creating or updating reduced order models. Second, new metrics were developed that simplify the process of isolating an NNM in a measurement using stepped-sine testing. The metrics were validated in simulation and experiments were presented in which an internal resonance was isolated for the first time (although with some inaccuracy due to the experimental setup). Finally, these methods were applied to nonlinear model updating of several geometrically nonlinear structures producing encouraging results. These contributions are discussed in more detail below.

5.1 *Continuous-scan Laser Doppler Vibrometry and Three Dimensional-Digital Image Correlation*

In Chapter 2 it was shown that Continuous-scan Laser Doppler Vibrometry (CSLDV) and Three Dimensional-Digital Image Correlation (3D-DIC) can be used to obtain full-field measurements of a structure vibrating in linear and nonlinear response regimes. This was demonstrated on two structures: a clamped-clamped flat beam and a fully clamped flat plate. For low amplitude, linear deformations, it was shown that CSLDV was able to reconstruct the measured deformation shapes more accurately than 3D-DIC due to 3D-DIC's limited resolution at low amplitudes. When using CSLDV, the spatial measurement information is not governed by the number of points used to define the shape but by the number of Fourier coefficients that can

be identified to describe the time-varying shape. The number of harmonics is especially important when a more complex 2-D measurement grid is used, as demonstrated with the flat panel. Hence, the main disadvantage of CSLDV is that the harmonics describing the shapes are measured rather than the shapes at individual points, and so there may be uncertainty as to whether a feature in the measured deformation is really meaningful. For higher amplitude, nonlinear deformations, 3D-DIC was shown to reconstruct more complex spatial deformations at higher harmonics more accurately than CSLDV, further emphasizing the reliance of higher harmonics for the correct reconstruction of the deformation shape.

Both techniques can provide dense measurements along surfaces, as long as each technique can "see" the surface. To provide accurate measurements, both techniques require surface preparation, unless the material used for the test piece fulfills specific requirements (e.g. a random pattern for 3D-DIC and a sufficiently reflective pattern for CSLDV). For DIC, this surface preparation is especially important when response levels are small, or in a structure's linear range. For CSLDV, surface preparation becomes more important when the vibration amplitude becomes small relative to speckle noise, and also as the laser standoff distance (or field of view) increases.

Finally, this study has illustrated that when full-field velocities or displacements are measured (i.e. as opposed to the usual case where the motion is only captured at a few points), inconsistencies in the dynamic behavior of the structure under test can be identified and provide insight to modeling and predicting dynamic behavior. Here, the CSLDV and DIC shapes revealed asymmetry in the 2nd and 3rd bending mode shapes of the beam and a skew in mode 1 of the bending mode shape of the plate, which was probably due to (un-modeled) asymmetry in the boundary conditions or initial geometry of the plate since it is thin. If a traditional test were

performed with only a few measurement points, one would not be likely to detect this, nor would they have sufficient information to update the model to account for it.

5.2 *Experimental Identification of Nonlinear Normal Modes*

In Chapter 3, a method to determine the numerical and experimental single point force needed to appropriate a nonlinear normal mode (NNM) was demonstrated on a clamped-clamped flat beam and curved axi-symmetric perforated plate. It was shown that higher harmonics are needed in the input force to fully appropriate a NNM when there is strong harmonic coupling between the LNMs of a structure. For both structures, a strong harmonic coupling was observed, 5:1 coupling for the flat beam and a 3:1 coupling for the curved axi-symmetric plate. The measured response of the flat beam shows the ability to achieve an appropriated NNM response in the neighborhood of the beam's first NNM with mono- and multi-harmonic forcing. The measured response of the curved axi-symmetric plate also shows the ability to achieve a dynamic response in the neighborhood of the first NNM of a more complex structure.

For both structures investigated, full-field deformation measurements were key to the identification of nonlinear coupling between the LNMs of the structure. These measurements are particularly beneficial when examining the more complex curved axi-symmetric plate. With the identification of the nonlinear coupling of the LNMs, experimental nonlinear modal models can be created and tuned to better match the nonlinear dynamics. This idea emphasizes an important area this work can be expanded upon where nonlinear modal analysis techniques can be used to examine nonlinear coupling between LNMs tying together linear and nonlinear experimental modal analysis.

5.3 *Model Updating and Validation using Experimentally and Numerically Determined Linear and Nonlinear Normal Modes*

Through the examination of single point responses on each of the beam's surface, the frequency-displacement relationship is presented. For the geometrically nonlinear beams investigated, the inclusion of this curvature is an important step to the accurate estimation of the nonlinear energy dependence of the fundamental frequency of vibration. Additionally, through the change of boundary conditions, this energy dependence can be further tuned to match experimental measurements. For the nominally flat beam, this resulted in a well tuned model; however, this was not the case for the beam with an initial curvature. For the curved beam, changing the curvature and boundary conditions change the fundamental characteristic of the nonlinearity inherent to the structure so, more care must be taken in the model updating procedure to determine which features in the model need to be updated. In this regard, it is hoped that full field measurements will provide insights into what changes to the model are needed.

6 Future Work

6.1 *Characterization and Optimization of Experimental Setup for Continuous-scan Laser Doppler Vibrometry and Three Dimensional-Digital Image Correlation*

Continuous-scan Laser Doppler Vibrometry (CSLDV) and Three Dimensional-Digital Image Correlation (3D-DIC) was successfully used to measure the full-field linear and nonlinear deformations of a structure; however, the use of each technique is currently more of an art than a science. For CSLDV, parameters such as the laser standoff distance, scan frequency, and scan pattern are selected based on the experimenter's experience and knowledge of the structural response being measured. An experienced operator typically needs to perform trial and error experiments when a structure exhibits unexpected responses. For 3D-DIC, parameters such as the camera standoff distance, camera angle, calibration parameters, and application of speckle pattern are based on the experimenter's experience and knowledge of the interaction between all parameters in the measured of a deforming structure. Similar to CSLDV, a series of trial and error experiments are needed to find an optimal setup. Both measurement methods would benefit from a more formal definition of the optimum experimental parameters used.

6.2 *Experimental Identification of Nonlinear Normal Modes*

The presented methods developed to isolate the nonlinear normal modes (NNMs) of a structure require much user interaction. Therefore, the identification of NNMs is dependent on the experimenters knowledge of how the damped forced response manifests in nonlinear regimes. Automation of the identification of NNMs is further complicated since structures

exhibit dynamics such as jumps, quasi- or fully chaotic responses requiring a continuous tuning of the force distribution and harmonic content step size used in the isolation of an NNM to remain on a forced response curve. The use of power balance methods along with real time tonal analysis methods to determine the phase relationships between the force and response at all harmonics dynamically would be one path to the development of automatic NNM identification algorithms.

6.3 *Update Models using Nonlinear Normal Modes*

As shown, nonlinear normal modes (NNMs) provide a useful representation of a structure's bifurcations, internal resonances, and a strong dependence on input energy through the use of frequency energy plots (FEPs). Additionally, the time-series domain of the periodic solutions for each harmonic provides a description of how higher harmonics appear in the response throughout increasingly nonlinear response regimes. This response can be projected onto the linear normal modes (LNMs) of the response providing a characterization of the nonlinear coupling of the LNMs over desired ranges of the dynamic response.

6.4 *Model Validation using Nonlinear Measured and Simulated Responses*

Though NNMs provide an excellent tool to validate a model in nonlinear response regimes, it is also beneficial to further validate the updated models when subjected to other types of loading. Therefore, during previous testing, additional low and high amplitude response data was measured when the structures of interest were subjected to a band limited random excitation. This random response data can be used to validate the fully updated models through the examination of the measured and simulated response power spectral densities (PSDs). Schoneman et al. [106] recently used this type of model validation to validate nonlinear reduced

order models (NLROMs) of a flat beam. It was observed that the coupled dynamics between mode 1, 3, and 5 was key to the accurate prediction of the response PSDs. Without the inclusion of mode 1, the response PSD did not capture the nonlinear behavior of the flat beam investigated. A similar use of the response PSDs will be implemented to provide a final validation step for the fully updated models.

Acknowledgements

Support for this research was provided by the University of Wisconsin – Madison Graduate School with funding from the Wisconsin Alumni Research Foundation and through the Structural Sciences Center in the Air Force Research Laboratory's summer internship program.

Appendix – Publications of PhD work

Journal Papers

- **Ehrhardt, D.A.**, Yang, S., Beberniss, T.J., and Allen, M.S., "Full Field Measurements of beams and plates with Continuous-Scan Laser Doppler Vibrometry and 3D-Digital Image Correlation," Mechanical Systems and Signal Processing (Submitted)
- **Ehrhardt, D.A.**, Allen, M.S., and Beberniss, T.J., "Measurement of Nonlinear Normal Modes using Mono-Harmonic Force Appropriation and Full Field Measurements," Mechanical Systems and Signal Processing Special Issue Dedicated to the Identification of Nonlinear Mechanical Systems (in preparation)
- **Ehrhardt, D.A.** and Allen, M.S., "Model Updating of Geometrically Nonlinear Flat and Curved Beam with Nonlinear Normal Modes," AIAA Journal (in preparation)

Conference Papers

- **Ehrhardt, D.A.**, Yang, S., Beberniss, T.J., and Allen, M.S., " Linear and Nonlinear Response of a Rectangular Plate Measured with Continuous-Scan Laser Doppler Vibrometry and 3D-Digital Image Correlation," 33rd International Modal Analysis Conference, February 2-5, 2015.
- **Ehrhardt, D.A.**, Allen, M.S., " Measurement of Nonlinear Normal Modes using Mono-harmonic Force Appropriation: Experimental Investigation," 33rd International Modal Analysis Conference, February 2-5, 2015.
- **Ehrhardt, D.A.**, Kuether, R.J., and Allen, M.S., "Nonlinear Normal Modes in Finite Element Model Validation of Geometrically Nonlinear Flat and Curved Beams," AIAA SciTech 2015, January 5-9, 2015.
- **Ehrhardt, D.A.**, Yang, S., Beberniss, T.J., and Allen, M.S., "Mode Shape Comparison Using Continuous-scan Laser Doppler Vibrometry and High Speed 3D Digital Image Correlation," 32nd International Modal Analysis Conference, February 3-6, 2014.

- **Ehrhardt, D.A.**, Harris, R.B., and Allen, M.S., "Numerical and Experimental Determination of Nonlinear Normal Modes of a Circular Perforated Plate," 32nd International Modal Analysis Conference, February 3-6, 2014.
- **Ehrhardt, D.A.** and Beberniss, T.J., "Experimental Investigation of Dynamic out of Plane Displacement Error in 3D Digital Image Correlation," AIAA Conference, April 8-11, 2013. DOI: 10.2514/6.2013-1779.
- **Ehrhardt, D.A.**, Abanto-Bueno, J.A., Shukla, A., and Parks, C., "Non-contact Experimental Modal Analysis of a Curved Beam using a Full-Field Optical Technique," AIAA, April 4-7, 2011. DOI: 10.2514/6.211-1945.

References

[1] ASME, "Guide for Verification and Validation in Computational Solid Mechanics," vol. V V 10-2006, ed, 2006.

[2] R. J. Allemang, "Editorial: Verification and Validation," *Sound and Vibration,* January 2013.

[3] J. H. Ginsberg, *Mechanical and Structural Vibrations*, First ed. New York: John Wiley and Sons, 2001.

[4] M. I. Friswell, and Mottershead, J.E., *Finite Element Model Updating in Structural Dynamics*: Kluwer Academic Publishers, 1995.

[5] D. J. Ewins, *Modal Analysis Theory, Practice, and Application*, Second Edition ed.: Research Studies Press Ltd., 2000.

[6] T. Abrahamsson, and Kammer, D., "Finite Element Model Calibration using Frequency Responses and Damping Equalization," presented at the 32nd International Modal Analysis Conference, Orlando, FL., 2013.

[7] R. J. Allemang, "The Modal Assurance Criterion (MAC): Twenty Years of Use and Abuse," in *XX International Modal Analysis Conference*, Los Angeles, CA, 2002.

[8] R. R. Craig, and Kurdila, A.J., *Fundamentals of Structural Dynamics*, 2nd ed.: Wiley, 2006.

[9] A. B. Stanbridge and D. J. Ewins, "Modal Testing Using a Scanning Laser Doppler Vibrometer," *Mechanical Systems and Signal Processing,* vol. 13, pp. 255-270, 1999.

[10] M. A. Sutton, Orteu, J.J., and Schreier, H., *Image Correlation for Shape, Motion, and Deformation Measurements: Basic Concepts, Theory, and Applications*. New York, NY: Springer, 2009.

[11] R. M. Rosenberg, "Normal Modes of Nonlinear Dual-Mode Systems," *Journal of Applied Mechanics,* vol. 27, pp. 263-268, 1960.

[12] A. F. Vakakis, Manevitch, L.I., Mikhlin, Y.V., Pilipchuk, V.M., and Zeven, A.A., *Normal Modes and Localization in Nonlinear Systems*. New York: John Wiley & Sons, 1996.

[13] G. Kerschen, M. Peeters, J. C. Golinval, and A. F. Vakakis, "Nonlinear normal modes, Part I: A useful framework for the structural dynamicist," *Mechanical Systems and Signal Processing,* vol. 23, pp. 170-194, 2009.

[14] A. H. Nayfeh, *Nonlinear Interactions: Analytical, Computational, and Experimental Methods*. New Your, NY, 2000.

[15] A. H. Nayfeh, *Nonlinear Oscillations*. New York: John Wiley and Sons, 1979.

[16] M. Peeters, G. Kerschen, and J. C. Golinval, "Modal testing of nonlinear vibrating structures based on nonlinear normal modes: Experimental demonstration," *Mechanical Systems and Signal Processing,* vol. 25, pp. 1227-1247, 2011.

[17] J. L. Zapico-Valle and M. García-Diéguez, "Dynamic modeling and identification of the Uniovi structure," *Int. J. Simul. Multidisci. Des. Optim.,* vol. 5, p. A06, 2014.

[18] G. Kerschen, K. Worden, A. F. Vakakis, and J.-C. Golinval, "Past, present and future of nonlinear system identification in structural dynamics," *Mechanical Systems and Signal Processing,* vol. 20, pp. 505-592, 2006.

[19] M. Kurt, "Identificatoin, Reduced Order Modeling, and Model Updating of Nonlinear Mechanical Systems," PhD, Mechanical Engineering, University of Illinois at Urbana-Champaign, Urbana, Illinois, 2014.
[20] J. P. Noel, Renson, L., Grappasonni, C., and Kerschen, G., "Identification of Nonlinear Normal Modes of Engineering Structures under Broadband Forcing," *Mechanical Systems and Signal Processing*.
[21] M. Peeters, G. Kerschen, and J. C. Golinval, "Dynamic testing of nonlinear vibrating structures using nonlinear normal modes," *Journal of Sound and Vibration,* vol. 330, pp. 486-509, 2011.
[22] P. A. Atkins, Wright, J.R., and Worden, K., "An Extension of Force Appropriation to the Identification of Nonlinear Multi Degree of Freedom Systems," *Journal of Sound and Vibration,* vol. 237, pp. 23-43, 2000.
[23] N. M. Wereley, "Analysis and Control of Linear Periodically Time Varying Systems," Ph.D. Ph.D., Aeronautics and Astronautics, Massachusetts Institute of Technology, Cambridge, 1991.
[24] A. B. Stanbridge, D. J. Ewins, and A. Z. Khan, "Modal testing using impact excitation and a scanning LDV," *Shock & Vibration,* vol. 7, p. 91, 2000.
[25] M. Martarelli, "Exploiting the Laser Scanning Facility for Vibration Measurements," Ph.D. Ph.D. , Technology & Medice, Imperial College, London, 2001.
[26] A. B. Stanbridge, M. Martarelli, and D. J. Ewins, "Measuring area vibration mode shapes with a continuous-scan LDV," *Measurement,* vol. 35, pp. 181-189, 2004.
[27] C. W. Schwingshackl, A. B. Stanbridge, C. Zang, and D. J. Ewins, "Full-Field Vibration Measurement of Cylindrical Structures using a Continuous Scanning LDV Technique," presented at the 25th International Modal Analysis Confernce (IMAC XXV), Orlando, Florida, 2007.
[28] M. S. Allen, "Frequency-Domain Identification of Linear Time-Periodic Systems using LTI Techniques," *Journal of Computational and Nonlinear Dynamics* vol. 4, 24 Aug. 2009.
[29] S. Yang, M. W. Sracic, and M. S. Allen, "Two algorithms for mass normalizing mode shapes from impact excited continuous-scan laser Doppler vibrometry," *Journal of Vibration and Acoustics,* vol. 134, p. 021004, 2012.
[30] N. M. Wereley, "Analysis and Control of Linear Periodically Time Varying Systems," PhD, Department of Aeronautics and Astronautics, Massachusetts Institute of Technology, Cambridge, 1991.
[31] N. M. Wereley and S. R. Hall, "Linear time periodic systems: transfer functions, poles, transmission zeroes and directional properties," presented at the Proceedings of the 1991 American Control Conference, Boston, MA, USA, 1991.
[32] N. M. Wereley and S. R. Hall, "Frequency response of linear time periodic systems," Honolulu, HI, USA, 1990, pp. 3650-3655.
[33] S. Yang, "Modal Identification of Linear Time Periodic Systems with Applications to Continuous-Scan Laser Doppler Vibrometry," Ph.D, Engineering Physics, University of Wisconsin-Madison, 2013.
[34] T. E. Schmidt, J. Tyson, K. Galanulis, D. M. Revilock, and M. E. Melis, "Full-field dynamic deformation and strain measurements using high-speed digital cameras," in *26th International Congress on High-Speed Photography and Photonics*, Bellingham, WA, 2005, pp. 174-185.

[35] V. Tiwari, Sutton, M.A., Shultis, G., McNeill, S.R., Xu, S., Deng, X., Fourney, W.L., and Bretall, D., "Measuring full-field transient plate deformation using high speed imaging systems and 3D-DIC," in *Proceedings of the Society for Experimental Mechanics Annual Conference*, Albuquerque, 2009.

[36] C. Niezrecki, P. Avitabile, C. Warren, P. Pingle, and M. Helfrick, "A Review of Digital Image Correlation Applied to Structural Dynamics," *AIP Conference Proceedings,* vol. 1253, pp. 219-232, 2010.

[37] M. Helfrick, "3D Digital Image Correlation Methods for Full-Field Vibration Measurement," *Mechanical Systems and Signal Processing,* vol. 25, pp. 917-927, 2011.

[38] C. Warren, C. Niezrecki, P. Avitabile, and P. Pingle, "Comparison of FRF measurements and mode shapes determined using optically image based, laser, and accelerometer measurements," *Mechanical Systems and Signal Processing,* vol. 25, pp. 2191-2202, 2011.

[39] J. Abanto-Bueno, Ehrhardt, D., Shukla, A., and Parks, C., "Non-Contact Experimental Modal Analysis of a Curved Beam using a Full-Field Optical Technique," in *52nd AIAA/ASME/ASCE/AHS/ASC Structures, Structural Dynamics and Materials Conference*, ed: American Institute of Aeronautics and Astronautics, 2011.

[40] D. A. Ehrhardt and T. J. Beberniss, "Experimental investigation of dynamic out of plane displacement error in 3D digital image correlation," in *54th AIAA/ASME/ASCE/AHS/ASC Structures, Structural Dynamics and Materials Conference, April 8, 2013 - April 11, 2013*, Boston, MA, United states, 2013.

[41] T. J. Beberniss, and Ehrhardt, D.A., "Temporal Aliasing in High-Speed 3-Dimensional Digital Image Correlation Vibration Measurement," presented at the SciTech 2015, Kissimmee, FL, 2015.

[42] D. A. Ehrhardt, Yang, S., Beberniss, T.J., and Allen, M.S., "Mode Shape Comparison Using Continuous-Scan Laser Doppler Vibrometry and High Speed 3D Digital Image Correlation," presented at the International Modal Analysis Conference XXXII, Orlando, FL, 2014.

[43] D. A. Ehrhardt, Yang, S., Beberniss, T.J., and Allen, M.S., "Linear and Nonlinear Response of a Rectangular Plate Measured with Continuous-Scan Laser Doppler Vibrometry and 3D-Digital Image Correlation," presented at the International Modal Analysis Conference XXXIII, Orlando, Florida, 2015.

[44] Y. S. Lee, Kerschen, G., Vakakis, A.F., Panagopoulos, P., Bergman, L., and McFarland, D.M., "Complicated Dynamics of a Linear Oscillator with a Light Essentially Nonlinear Attachment," *Physica D,* vol. 204, pp. 41-69, 2005.

[45] D. A. Ehrhardt, Allen, M.S., Beberniss, T.J., "Measurement of Nonlinear Normal Modes using Mono-harmonic Force Appropriation: Experimental Investigation," in *International Modal Analysis Conference 33*, Orlando, FL, 2015.

[46] K. Worden, and Tomlinson, G.R., *Nonlinearity in Structural Dynamics: Detection, Identification, and Modeling*. Bristol and Philadelphia: Institute of Physics Publishing, 2001.

[47] M. Peeters, G. Kerschen, J. C. Golinval, C. Stéphan, and P. Lubrina, "Nonlinear Normal Modes of a Full-Scale Aircraft," in *Modal Analysis Topics, Volume 3*, T. Proulx, Ed., ed: Springer New York, 2011, pp. 223-242.

[48] D. A. Ehrhardt, Harris, R.B., and Allen, M.S., "Numerical and Experimental Determination of Nonlinear Normal Modes of a Circular Perforated Plate," in *International Modal Analysis Conference XXXII*, Orlando, Fl, 2014, pp. 239-251.
[49] A. H. Nayfeh, *Introduction to Perturbation Techniques*. New York: Wiley, 1981.
[50] W. Lacarbonara, Rega, G., Nayfeh, A.H., "Resonant Nonlinear Normal Modes Part I: Analytical Treatment for Structural One-dimensional Systems," *International Journal for Nonlinear Mechanics,* vol. 38, pp. 851-872, 2003.
[51] R. Arquier, Bellizzi, S., Bouc, R., and Cochelin, B., "Two methods for the computation of nonlinear modes of vibrating systems at large amplitudes," *Computers and Structures,* vol. 84, pp. 1565-1576, 1996.
[52] R. J. Kuether, and Allen, M.S., "A numerical approach to directly compute nonlinear normal modes of geometrically nonlinear finite element models," *Mechanical Systems and Signal Processing,* vol. 46, pp. 1-15, 2014.
[53] M. Peeters, Viguie, R., Serandour, G., Kerschen, G., and Golinval, J.C., "Nonlinear Normal Modes, Part II: Toward a Practical Computation using Numerical Continuation Techniques," *Mechanical Systems and Signal Processing,* vol. 23, pp. 195-216, 2009.
[54] R. J. Kuether, Allen, M.S., "Computing Nonlinear Normal Modes using Numerical Continuation and Force Appropriation," in *ASME 2012 International Design Engineering Technical Conferences & Computers and Information in Engineering Conference*, Chicago IL, 2012.
[55] M. S. Allen, R. J. Kuether, B. Deaner, and M. W. Sracic, "A Numerical Continuation Method to Compute Nonlinear Normal Modes Using Modal Reduction," presented at the 53rd AIAA Structures, Structural Dynamics, and Materials Conference, Honolulu, Hawaii, 2012.
[56] R. J. Kuether and M. S. Allen, "Structural Modification of Nonlinear FEA Subcomponents Using Nonlinear Normal Modes," presented at the 31st International Modal Analysis Conference (IMAC XXXI), Garden Grove, California, 2013.
[57] A. B. Stanbridge, A. Z. Khan, and D. J. Ewins, "Modal testing using impact excitation and a scanning LDV," *Shock and Vibration,* vol. 7, pp. 91-100, 2000.
[58] D. Di Maio, Ewins, D.J., "Continuous Scan, A Method for Performing Modal Testing Using Meaningful Measurement Parameters Part I," *Mechanical Systems and Signal Processing,* vol. 25, pp. 3024-42, 2011.
[59] M. S. Allen, "Frequency-Domain Identification of Linear Time-Periodic Systems Using LTI Techniques," *Journal of Computational and Nonlinear Dynamics,* vol. 4, pp. 041004-041004, 2009.
[60] N. M. Wereley and S. R. Hall, "Frequency response of linear time periodic systems," in *Decision and Control, 1990., Proceedings of the 29th IEEE Conference on*, 1990, pp. 3650-3655 vol.6.
[61] N. M. Wereley and S. R. Hall, "Linear Time Periodic Systems: Transfer Function, Poles, Transmission Zeroes and Directional Properties," in *American Control Conference, 1991*, 1991, pp. 1179-1184.
[62] S. Yang, and Allen, M.S., "Harmonic Transfer Function to Measure Translational and Rotational Velocities With Continuous-Scan Laser Doppler Vibrometry," *Journal of Vibration and Acoustics,* vol. 136, pp. 021025-021025, 2014.

[63] S. Yang, and Allen, M.S., "Output-Only Modal Analysis Using Continuous-Scan Laser Doppler Vibrometry and Application to a 20kW Wind Turbine," *Mechanical Systems and Signal Processing,* vol. 31, August 2012 2011.
[64] S. Yang, and Allen, M.S., "Lifting approach to simplify output-only continuous-scan laser vibrometry," *Mechanical Systems and Signal Processing,* vol. 45, pp. 267-282, 2014.
[65] G. mbH, "Aramis," 6.3.0 ed. Braunschweig, Germany, 2011.
[66] G. mbH, "IVIEW Real Time Sensor," 6.3.0 ed. Braunschweig, Germany, 2011.
[67] R. W. Gordon, Hollkamp, J.J., and Spottswood, S. M., "Non-linear Response of a Clamped-Clamped Beam to Random Base Excitation," presented at the VIII International Conference on Recent Advances in Structural Dynamics, Southampton, United Kingdom, 2003.
[68] R. W. Gordon, and Hollkamp, J.J., "Nonlinear Random Response of a Clamped Plate: A Well Characterized Experiment," *47th AIAA/ASME/ASCE/AHS/ASC Structures, Structural Dynamics, and Materials Conference,* vol. 6, pp. 4007-4024, 2006.
[69] R. J. Kuether and M. S. Allen, "A Numerical Approach to Directly Compute Nonlinear Normal Modes of Geometrically Nonlinear Finite Element Models," *Mechanical Systems and Signal Processing,* vol. 46, pp. 1–15, 2014.
[70] G. Kerschen, M. Peeters, J. C. Golinval, and A. F. Vakakis, "Nonlinear normal modes. Part I. A useful framework for the structural dynamicist," *Mechanical Systems and Signal Processing,* vol. 23, pp. 170-94, 2009.
[71] R. W. Gordon and J. J. Hollkamp, "Reduced-order Models for Acoustic Response Prediction," Air Force Research Laboratory, AFRL-RB-WP-TR-2011-3040, Dayton, OH2011.
[72] M. W. Sracic, and Allen, M.S., "Experimental Investigation of the Effect of Speckle Noise on Continuous Scan Laser Doppler Vibrometer Measurements," presented at the XXVII International Modal Analysis Conference, Orlando, FL, 2009.
[73] R. J. Allemang, and Brown, D.L., *Chapter 21: Experimental Modal Analysis*, 6th ed.: McGraw-Hill Book Company, 2008.
[74] G. Kerschen, and Golinval, J.C. (2015). *Experimental Modal Analysis*. Available: www.ltas-vis.ulg.ac.be/cmsms/uploads/File/Mvibr_notes.pdf
[75] G. F. Lang, "Matrix Madness and Complex Confusion... A Review of Complex Modes from Multiple Viewpoints," *Journal of Sound and Vibration,* vol. 46, 2012.
[76] J. H. Ginsberg, *Mechanical and Structural Vibrations Theory and Applications*: John Wiley and Sons Inc., 2001.
[77] W. T. Thomson, and Dahleh, M.D., *Theory of Vibration with Applications*, 5th ed. Upper Saddle River, New Jersey: Prentice-Hall Inc., 1998.
[78] R. C. Hibbeler, *Dynamics*, 13 ed. Upper Saddle River, NJ: Prentice Hall, 2010.
[79] F. Costanzo, Plesha, M.E., and Gray, G.L., *Statics and Dynamics*. New York, NY: The McGraw-Hill Companies Inc., 2010.
[80] A. F. Vakakis, "NonLinear Normal Modes and Their Applications in Vibration Theory: An Overview," *Mechanical Systems and Signal Processing,* vol. 11, pp. 3-22, 1997.
[81] D. Jiang, Pierre, C., and Shaw, S.W.,, "The Construction of Non-Linear Normal Modes for Systems with Internal Resonance," *International Journal for Nonlinear Mechanics,* vol. 40, pp. 729-46, 2005.

[82] S. A. Neild, Cammarano, A., and Wagg, D.J.,, "Towards a Technique for Nonlinear Modal Analysis," in *ASME International Design Engineering Technical Conferences and Computers and Information in Engineering Conference*, 2012.

[83] H. Ardeh and M. Allen, "Investigating Cases of Jump Phenomenon in a Nonlinear Oscillatory System," in *Topics in Nonlinear Dynamics, Volume 1*. vol. 35, G. Kerschen, D. Adams, and A. Carrella, Eds., ed: Springer New York, 2013, pp. 299-318.

[84] R. J. Kuether, and Allen, M.S., "Computing Nonlinear Normal Modes Using Numerical Continuation and Force Appropriation," presented at the 24th Conference on Mechanical Vibration and Noise, 2012.

[85] R. J. Kuether, B. Deaner, M. S. Allen, and J. J. Hollkamp, "Evaluation of Geometrically Nonlinear Reduced Order Models with Nonlinear Normal Modes," *AIAA Journal,* vol. Submitted August, 2014.

[86] D. J. Ewins, "Basics and State-of-the-art of Modal Testing," *Sadhana,* vol. 25, pp. 207-20, 2000.

[87] D. Goge, Boswald, M., Fullekrug, U., and Lubrina, P.,, "Ground Vibration Testing of Large Aircraft - State of the Art and Future Perspectives," presented at the XXV International Modal Analysis Conference, Orlando, FL, 2011.

[88] B. Peeters, Climent, H., de Diego, R., de Alba, J., Rodriques Ahlquist, J., Martinez Carreno, J., Hendricx W., Rega, A., Garcia, G., Deweer, J., and Debille, J.,, "Modern Solutions for Ground Vibration Testing of Large Aircraft," presented at the XXVI International Modal Analysis Conference, Orlando, FL, 2008.

[89] R. C. Lewis, and Wrisley, D.L., "A System for the Excitation of Pure Natural Modes of Complex Structure," *Journal of the Aeronautical Sciences (Institute of the Aeronautical Sciences),* vol. 17, pp. 705-722, 1950/11/01 1950.

[90] B. Fraeijs de Veubeke, *A variational approach to pure mode excitation based on characteristic phase lag theory*. Paris, France: North Atlantic Treaty Organization, Advisory Group for Aerospace Research and Development, 1956.

[91] D. Otte, Van der Auweraer, H., Debille, J., and Leuridan, J., "Enhanced Force Vector Appropriation Methods for Normal Mode Testing," in *Preeceedings of the 17th International Seminar on Modal Analysis*, 1992.

[92] J. R. Wright, Cooper, J.E., and Desforges, M.J., "Normal Mode Force Appropriation - Theory and Application," *Mechanical Systems and Signal Processing,* vol. 13, pp. 217-240, 1999.

[93] K. Alexiou, and Wright, J.R., "Comparison of MultiPoint Vibration Test Methods," presented at the IX International Modal Analysis Conference, Florence, Italy, 1991.

[94] H. T. Banks, Inman, D. J., "On Damping Mechanisms in Beams," *Journal of Applied Mechanics,* vol. 58, pp. 716-723, 1991.

[95] M. Geradin, and Rixen, D., *Mechanical Vibrations; Theory and Application to Structural Dynamics*: Wiley, 1997.

[96] T. L. Hill, Cammarano, A., Neild, S.A., and Wagg, D.J., "Interpreting the Forced Response of a Two-Degree-of-Freedom Nonlinear Oscillator using Backbone Curves," *Journal of Sound and Vibration,* vol. Submitted, 2014.

[97] R. J. Kuether, Renson, L., Detroux, T., Grappasonni, C., Kerschen, G, and Allen, M.S., "Nonlinear Normal Modes, Modal Interactions, and Isolated Resonance Curves," *Mechanical Systems and Signal Processing,* vol. Submitted, 2015.

[98] A. A. Muravyov, and Rizzi, S.A., "Determination of Nonlinear Stiffness with Application to Random Vibration of Geometrically Nonlinear Structures," *Computers and Structures,* vol. 81, pp. 1513-1523, 2003.
[99] J. J. Hollkamp and R. W. Gordon, "Reduced-order models for nonlinear response prediction: Implicit condensation and expansion," *Journal of Sound and Vibration,* vol. 318, pp. 1139-1153, 2008.
[100] E. J. Breitbach, "A Semi-Automatic Modal Survey Test Technique for Complex Aircraft and Spacecraft Structures," in *Proceedings of 3rd ESA Testing Symposium*, 1973, pp. 519-528.
[101] S. W. Shaw, "An Invariant Manifold Approach to Nonlinear Normal Modes of Oscillation," *Journal of Nonlinear Science,* vol. 4, pp. 419-448, 1994.
[102] C. Torrence, and Compo, G.P., "A Practical Guide to Wavelet Analysis," *Bulletin of the American Meteorological Society,* vol. 79, 1998.
[103] M. Feldman, "Hilbert Transform in Vibration Analysis," *Mechanical Systems and Signal Processing,* vol. 25, pp. 735-802, 2011.
[104] L. N. Virgin, *Vibration of Axially Loaded Structures*. Cambridge, United Kingdom: Cambridge University Press, 2007.
[105] L. N. Virgin, *Introduction to Experimental Nonlinear Dynamics: A Case Study in Mechanial Vibration*. Cambridge, United Kingdom: Cambridge University Press, 2000.
[106] J. D. Schoneman, Allen, M.S., and Kuether, R.J., "Relationships between Nonlinear Normal Modes and Responses to Random Inputs," presented at the SciTech 2014, National Harbor, MD, 2014.